N° d'ordre : 4037

THÈSE
en cotutelle

ENTRE

L'UNIVERSITÉ BORDEAUX 1

ÉCOLE DOCTORALE DES SCIENCES CHIMIQUES

et

UNIVERSITY OF CENTRAL FLORIDA

Par Ji Yeon CHOI

POUR OBTENIR LE GRADE DE

DOCTEUR

SPÉCIALITÉ : Laser, matière, nanosciences

Ecriture par Laser de fonctionnalités optiques : éléments diffractifs et ONL

Soutenue le : 14 juin 2010 (University of Central Florida)

Après avis de :

Mme K. RICHARDSON	Professeur – COMSET	Rapporteur
M. S. NOLTE	Professeur – IAP	Rapporteur

Devant la commission d'examen formée de :

M. D. HAGAN	Professeur – CREOL	Président du Jury
Mme K. RICHARDSON	Professeur – COMSET	Rapporteur
M. S. NOLTE	Professeur – IAP	Rapporteur
M. M. RICHARDSON	Professeur – CREOL	Examinateur
M. L. CANIONI	Professeur – CPMOH	Examinateur
M. T. CARDINAL	Chargé de Recherche – ICMCB	Examinateur

Université Bordeaux 1
Les Sciences et les Technologies au service de l'Homme et de l'environnement

ABSTRACT

Since the first demonstration of femtosecond laser written waveguides in 1996, femtosecond laser direct writing (FLDW) has been providing a versatile means to fabricate embedded 3-D microstructures in transparent materials. The key mechanisms are nonlinear absorption processes that occur when a laser beam is tightly focused into a material and the intensity of the focused beam reaches the range creating enough free electrons to induce structural modification. One of the most useful features that can be exploited in fabricating photonic structures is the refractive index change which results from the localized energy deposition. The laser processing system for FLDW can be realized as a compact, desktop station, implemented by a laser source, a 3-D stage and focusing optics. Thus, FLDW can be readily adopted for the fabrication of the photonic devices. For instance, it has been widely employed in various areas of photonic device fabrication such as active and passive waveguides, couplers, gratings, opto-fluidics and similar applications. This dissertation describes the use of FLDW towards the fabrication of custom designed diffractive optical elements (DOE's). These are important micro-optical elements that are building blocks in integrated optical devices including on-chip sensors and systems. The fabrication and characterization of laser direct written DOEs in different glass materials is investigated. The design and performance of a range of DOE's is described, especially, laser-written embedded Fresnel zone plates and linear gratings. Their diffractive efficiency as a function of the fabrication parameters is discussed and an optimized fabrication process is realized. The potential of the micro-DOEs and their integration shown in this dissertation will impact on the fabrication of future on-chip devices involving customized

DOEs that will serve great flexibility and multi-functional capability on sensing, imaging and beam shaping.

ACKNOWLEDGMENTS

I have to confess that the accomplishment I present in my dissertation is not my own, but an outcome made by great teamwork with people who I met in and out of CREOL and Orlando in the last five years. I have been one of the primary participants in making the research work. I have been very fortunate to have them in my life.

First and foremost, I would like to thank my advisor, Dr. Martin Richardson, for his support and endless encouragement. He has provided me amazing opportunities I could not even imagine before my doctoral study. I saw him at a conference in Seoul, Korea in 2003, and that was the prelude to my blessed five years. He has encouraged me to continue research and led me to move forward every moment I was stuck somewhere without any progress. He also broadened my sight to see not only obstacles I faced but also the things beyond them to keep me motivated.

I am deeply thankful to my French advisors, Dr. Thierry Cardinal at ICMCB and Dr. Lionel Canioni at CPMOH in University of Bordeaux, for giving me an opportunity to work in their laboratories. It was a great experience to work with people who are passionate and active in the lab. I have learned a lot from our many discussions. I will also never forget Dr. Cardinal's warm and friendly help in everything I needed when I was in Bordeaux.

I would also like to thank my dissertation committee professors, Dr. Aravinda Kar, Dr. M. G. "Jim" Moharam, Dr. David Hagan, Dr. Stefan Nolte and Dr. Kathleen C. Richardson for their useful advice which inspired me to be aware of other disciplines. I was able to improve my research with their guidance. In particular, Dr. Kathleen C. Richardson has taught me invaluable knowledge in material science and guided me to have a broad sight in that area. She has also been my mentor who showed me the life of the enthusiastic female scientist which I have always dreamed about.

I would like to thank Troy Anderson and Mark Ramme for being great colleagues and friends all the time. It was a pleasure to have both in the lab at the same time. I would also like to thank Michaël Hemmer for his enthusiastic support on lasers. I was deeply impressed and grateful for his spending many weekends and holidays to fix lasers.

I am truly thankful to the current laser plasma laboratory (LPL) members, Nicholas Barbieri, René Berlich, Andrew Housman, Nathan Bodnar, Christopher G. Brown, Matthew Fisher, Clémence Jollivet, Pankaj Kadwani, Reuvani Devi Kamtaprasad, Yuan Liu, Timothy S. McComb, Richard Ty Olmstead, Omar Rodriguez, Robert Andrew Sims, John Szilagyi, Andreas Vaupel, Benjamin Webb, Matthew Weidman, Christina Willis, Somsak (Tony) Teerawattanasook, Dr. Robert Bernath, Dr. Matthieu Baudelet, Dr. Lawrence Shah and Dr. Ilja Mingareev. I also have to thank all old LPL members, including Dr. Kazutoshi Takenoshita, Dr. Simi George, Dr, Vikas Sudesh and Dr. Santiago Palanco. In particular, I am thankful to Dr. Arnaud Zoubir for his pioneer work on femtosecond laser direct writing which impacted my research. I am also thankful to many CREOL colleagues including Georgios Siviloglou and Max Obando for their cheerful messages every time I was depressed. CREOL staff has provided me their wonderful support and I would like to thank them including Ms. Amy Perry and Ms. Rachel Franzetta.

I owe many things in my research from the Clemson team. Dr. Laeticia Petit deserves my deepest gratitude for her endless help and valuable discussions and comments. Nathan Carlie and Jonathan Massera have been the most excellent collaborators I could ever meet. I also want to thank my collaborators in Bordeaux, Dr. Arnaud Royon, who was also a member of LPL as a co-tutelle graduate student, Matthieu Bellec in CPMOH and Kevin Bourhis, Clement Maurel in ICMCB. Specifically, I am grateful to Dr. Evelyne Fargin for helping me to work with her group and teaching me many things. I also thank Dr. Michel Couzi for his expertise on micro Raman measurement, which is a very important part in my research. Rémi Bourdieu who was a REU from Bordeaux in summer 2009 helped me to gain interesting results. I appreciate the collaboration of Dr. Kye-Sung Lee, Dr. Supraja Murali and Dr. Rolland, in Rochester.

I am very thankful to Matthew Weidman, Christopher G. Brown, Reuvani Devi Kamtaprasad and John Broky for their great and timely help on editing my dissertation.

I deeply appreciate the warmth and friendship from the Korean community in Orlando including Bansok Church and Koreans in CREOL/UCF. I never felt alone with their prayer and support. I would like to thank many people in the US and Korea, including Pastor Kuh’s family, Dr. Hong and his family, Prof. Cho and Mrs. Cho, The Chons, The Lims, Dr. Song Hee Han, Dr. Hyejeong Chang and many others.

Finally, I would like to thank my parents, my sister Sukin, my brother Bongwon and my sister-in-law Sujin for their love, patience and encouragement. They believed in me and showed me their endless love throughout my graduate years. I could not be done with this race without their loving support.

LIST OF CONTENTS

LIST OF FIGURES

LIST OF TABLES

LIST OF ABBREVIATIONS

2-D	Two Dimension
3-D	Three Dimension
AFM	Atomic Force Microscopy
AO	Acousto-Optic
CCD	Charge Coupled Device
ChG	Chalcogenide
DE	Diffraction Efficiency
DIC	Differential Interference Contrast
DOE	Diffractive Optical Element
EO	Electro-Optic
FLDW	Femtosecond Laser Direct Writing
FZP	Fresnel Zone Plate
ICCD	Intensified Charge-Coupled Device
IR	Infrared
MIR	Mid-infrared
NIR	Near-infrared
OCT	Optical Coherence Tomography
OCM	Optical Coherence Microscopy
SHG	Second Harmonic Generation
THG	Third Harmonic Generation
UV	Ultraviolet
VIS	Visible

CHAPTER 1 : INTRODUCTION

Recent years have seen increasing demands for a variety of "integrated" on-chip photonic devices, as manufacturers of micro-sensors, micro-fluidics, micro-imaging systems, and photonic circuits continue to seek more compact, more portable, and even disposable platforms. Furthermore, as consumers of biological, medical, and informational technologies ask for more versatility and greater functionality, it has also seen demands increase for "customized" photonic devices that can readily accommodate the frequent revisions and customizations of the integrated platforms.

Until recently, custom-designed diffractive optical elements (DOEs) have played a key role in meeting the demands for these customized photonic devices, as they have many attractive features that their competitions do not have; for example, DOEs such as Fresnel zone plates (FZPs) are functionally very similar to refractive optics but have a much smaller component size and have the ability to reform the input beam distribution as well. That is why DOEs have been used in many compact optical devices such as micro imaging systems[1], EUV/X-ray imaging [2, 3], optical MEMS [4], micro sensors [5] and laser micromachining [6].

Despite these distinct advantages, however, conventional DOEs may not be the way to go, when we consider the current trend in micro-fabrication to move from planar to volumetric structures for higher-order integration. When it comes to customized 3-D micro-fabrication, conventional DOE fabrication techniques such as E-beam lithography, focused ion beam direct writing, UV laser direct writing, and a holographic recording technique are not practical. For example, E-beam lithography is a well-developed technique with high precision and throughput, especially suitable for mass production, but is complicated a multi-step process requiring long process time and high cost. To take another example, UV laser direct writing on photo-resist has the advantage of ease of fabrication, as it is based on the mask-free fabrication scheme, but it is also a complicated multi-step process, requiring longer fabrication time and higher cost, because both techniques have been developed and optimized for 2-D structures.

Given these limitations of DOEs, perhaps femtosecond laser direct writing (FLDW) is the most prominent technique for custom-designed 3-D fabrication, the concept of which is illustrated in Figure 1.1.

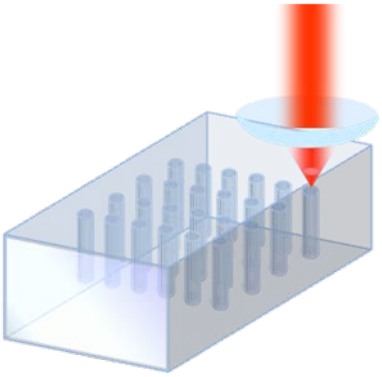

Figure 1.1 Schematic of femtosecond laser direct writing in a transparent medium

FLDW has many advantages over conventional DOEs. First, FLDW overcomes all the limitations of DOEs mentioned above. Second, with its nonlinear absorption process, it can produce a truly 3-D volumetric photonic structure in transparent optical materials. Third, it is so flexible that it does not require expensive photo-masks or any additional pre- or post-development process. Indeed, FLDW is a versatile tool that can be used in fabricating a variety of 3-D photonic structures such as active and passive waveguides[7-11], couplers[12, 13], gratings[14-19], and diffractive optical elements (DOEs) [20-23].

However, it also has difficulties to overcome to be a truly viable alternative to the conventional manufacturing techniques. First, its laser-written structures suffer from a low photo-induced refractive index change, resulting in low confinement in waveguide structures and low diffraction efficiency in DOEs. Second, its fabrication time is not competitive yet, because it is a “serial” process and thus limited by laser power, repetition rate, and focusing geometry. Third, its application so far has been limited; although many laser-written single elements have been developed, advanced platforms (such as integrated 3-D devices consisting of multiple laser-written structures integrated on a single chip) have not been fully explored, with the honorable exception of simple waveguide arrays and a stack of FZPs [23-25].

This dissertation is an attempt to overcome these difficulties, thereby furthering the potential of laser written volumetric DOEs that enable custom-designed micro optics for integrated on-chip devices. Specifically Fresnel zone plates and gratings are intensively investigated as the main topic of this dissertation. Moreover, this work explores a variety of novel optical materials to broaden the types of integrated optical device platforms possible, and investigates fabrication protocol required by evaluating material specific photo-response.

The scope of this dissertation is to discuss the fabrication of volumetric DOEs using FLDW in various bulk glass materials and their characterization. The diffraction efficiency dependence on the fabrication parameters is investigated in order to optimize the laser and optics parameters, respectively. The optimized parameters are then used to fabricate on-chip integrated devices involving DOEs in the bulk glass substrate.

Chapter Two discusses the distinctive features of femtosecond laser-matter interaction, especially its nonlinear absorption processes and localized heat accumulation. Chapter Three reviews the current techniques used in femtosecond laser direct writing, with their advantages and disadvantages, and introduces the laser systems that have been used for this work. Chapter Four presents the candidate materials with their distinct properties, methods and techniques to observe their properties, and their photo-response when exposed by a femtosecond laser. In Chapters Five and Six present a demonstration of a fabrication of custom designed laser direct written DOEs and of their integration with other photonic devices, respectively. The diffraction efficiency as a function of fabrication parameters is investigated as well as the coupling efficiency of DOEs with direct written waveguides. Chapter Seven presents a model of “laser depletion” as a way to create second-order nonlinear structure in amorphous glass, with recent experimental data supporting the model. Chapter Eight discusses the degradation of functionality of photo-written devices caused by the relaxation of material due to time and heat treatment. Chapter Nine summarize the main points of the thesis as well as perspectives.

CHAPTER 2 : THEORETICAL BACKGROUND ON FEMTOSECOND LASER-MATTER INTERACTION

This chapter discusses the distinctive features of femtosecond laser-matter interaction, especially its nonlinear absorption (ionization) processes and heat accumulation effect.

2.1 Femtosecond laser-matter interaction

Femtosecond lasers deliver a highly intense photon flux in an ultrashort time duration that is comparable to the order of elementary interaction time scales such as electron-electron or electron-phonon interaction times. The characteristic time scales of the electron collision time, the electron cooling time and lattice heating time are a few fs, 1~10 ps, and 0.1~1 ns, respectively[26, 27]. Figure 2.1 depicts the different laser-matter interactions for metals, semiconductors and insulators and their characteristic interaction time – laser intensity regimes.

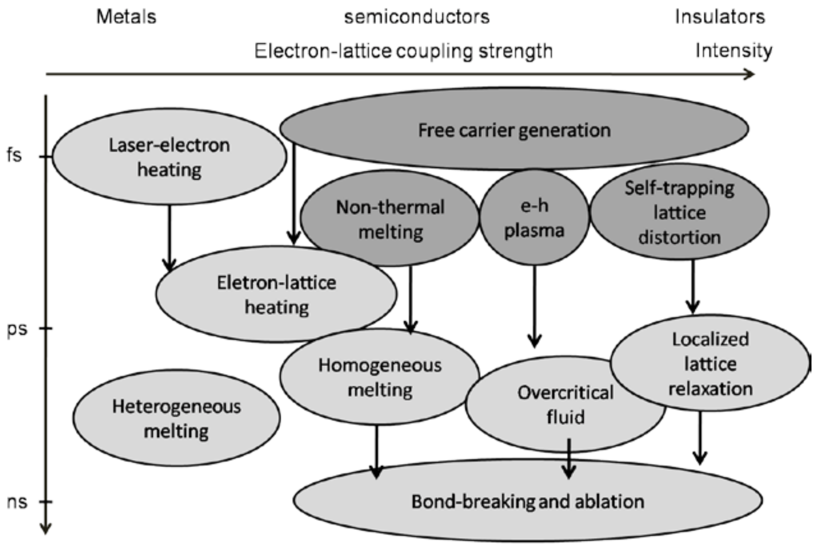

Figure 2.1 A chart showing schematically the relevant time and intensity scales for laser - matter interaction regime, modified from [28, 29]

It is to be noted that the mechanisms of light-matter interaction with ultrashort pulses differ from those of CW or longer pulse lasers; thus the resulting structures may exhibit many distinctive features. First, the interaction time is short enough to limit the interactions within a tiny focal volume, namely the “voxel” (volume pixel) because the energy transfer time is much shorter than the thermal diffusion time of the most materials in nature. The laser exposure is thus concluded even before the energy is transported to the surroundings within the material. A two-temperature model, described by a non-equilibrium state of extremely “hot” excited electrons combined with relatively “cold” surroundings, explains this situation [30, 31]. This plasma interaction, driven by a very short energy deposition time, leads to desirable features for micromachining such as the near absence of scarf material and the creation of a limited heat affected zone (HAZ). The energy loss due to thermal diffusion is negligible compared to the nanosecond laser pulse–matter interaction regime. The material damage thresholds expressed in J/cm^2 are reduced for ultrashort pulse irradiation [32, 33]. Figure 2.2 shows the reduction of damage thresholds of both fused silica and CaF_2 as the pulse width is decreased. It can also be seen that the plot fits well with the $\tau^{1/2}$ scaling, implying the effect is governed by thermal diffusion whose characteristic time is longer than ~10 ps where τ is the pulse width of the laser [28, 32, 34]. For material interaction with a laser pulse(s) whose pulse durations are shorter than 10 ps, the thermal diffusion is no longer the dominant factor that the damage threshold obeys. The threshold becomes less dependent on the $\tau^{1/2}$ scaling in this regime.

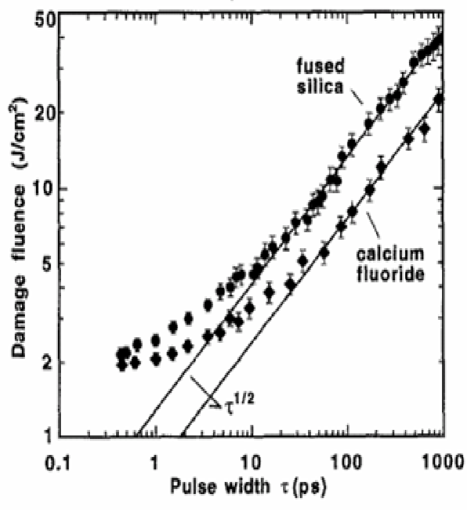

Figure 2.2 Fluence of the surface damage initiation in fused silica and CaF$_2$ as a function of pulse width. From [32].

In addition, extremely high laser intensity leads to nonlinear absorption processes in transparent dielectric materials that enable the highly localized energy deposition in the material with a lack of linear absorption. These processes are the most important features of ultrashort pulse – matter interaction in FLDW, another topic of this chapter.

2.2 Ionization mechanisms in transparent media

In transparent materials where the linear absorption is not present in the range of incident laser frequency ω ($\alpha_o \approx 0$), nonlinear ionization processes are the dominant excitation mechanisms. These promote a bound electron to the conduction band. In this case single photon excitation does not take place. Ionization processes in transparent materials consist of two complementary mechanisms. One is avalanche ionization and the other is photo-ionization [32-36].

2.2.1 Avalanche ionization

Avalanche ionization is itself a two-step process, where free carrier absorption by an electron in the conduction band is followed by impact ionization. A free electron in the conduction band absorbs photons until its energy exceeds the bandgap energy (E_g) of the material. An electron with an energy $E > E_g$ can then collide with, and excite another electron from the valence band to the conduction band. A schematic diagram of impact ionization is depicted in Figure 2.3,. This process will continue throughout the duration of a light pulse increasing the free electron density in the focal volume [32].

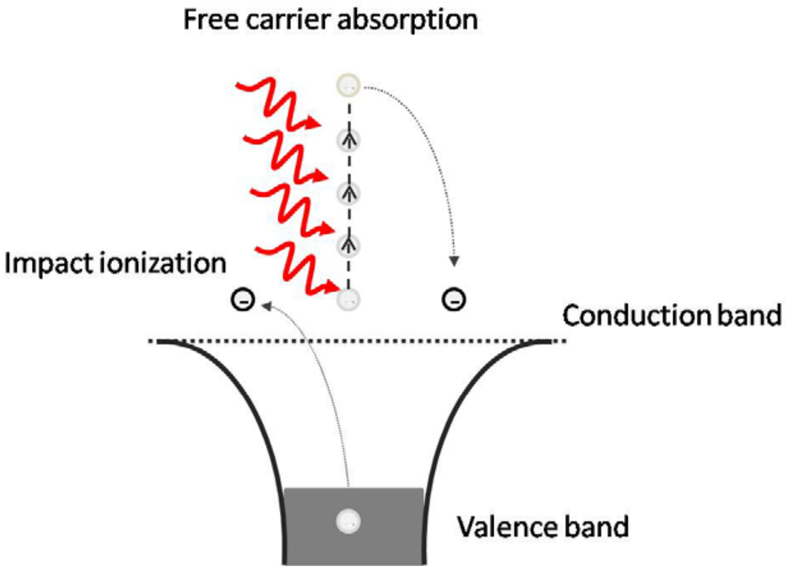

Figure 2.3 Schematic diagram of avalanche ionization consists of free carrier absorption and impact ionization

This process requires seed electrons in the conduction band to initiate photo-absorption. In the high intensity regime created by ultrashort pulses, the seed electrons can be generated directly by photo-ionization. This defines why femtosecond laser micromachining has a deterministic threshold because seed electrons can be always generated by photo-ionization whether or not seed electrons exist in the material. Long laser pulses, however, show a statistical behavior depending on the density of seed electrons and defects resulting in unevenly processed features in a high bandgap transparent material. This deterministic (statistical) behavior of ultrashort (long) pulse irradiation is clearly seen in Figure 2.4.

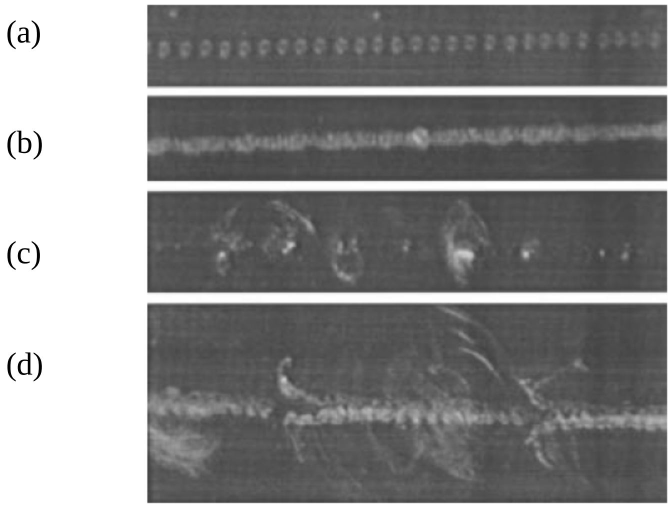

Figure 2.4 Comparison of micro drilling of PET plastic with different pulse widths at 800 nm. (a),(b) 80 fs, 5 μJ/pulse, with translation speed at 20 mm/s, 8 mm/s (c),(d) 200 ps. 20 μJ/pulse, 15 mm/s and 150 μJ/pulse, 20 mm/s. 80 fs pulses shows regularly ablated dots compared to 200 ps. From [37]

To formulate the avalanche ionization, the time dependent differential of the free electron density is described as Eq. (2.1) when a small number n_e of free electrons initially present within the voxel interact with the laser field

$$\frac{dn_e}{dt} = \alpha I(t) n_e , \tag{2.1}$$

where α, I(t), n_e are the avalanche ionization coefficient[cm^2/J], the incident laser intensity[W/cm^2] and the free electron density respectively.

2.2.2 Photo-ionization

If the material of interest is a transparent dielectric with a bandgap whose energy $E_g > \hbar\omega$, where $\hbar\omega$ is the photon energy of the incident laser wavelength, a single photon cannot excite an electron from the valence band to the conduction band. In this regime, only nonlinear absorption processes can excite the valence electron. Photo-ionization is the process of direct excitation of the electrons in the valence band by photons $\hbar\omega$. There are two regimes of photo-ionization, multiphoton ionization and tunneling ionization. Multiphoton ionization is the process in which an atom is ionized by absorbing n photons from the laser field, described as the Eq. (2.2) [38]:

$$n\hbar\omega + A^{q} = A^{q+1} + e^{-}, \tag{2.2}$$

where q is the charge of the target atomic system A, expressed in atomic units (a.u.), $\hbar\omega$ is the photon energy, and n > 1 is an integer indicating the number of participating photons. Multiphoton ionization of transparent material is the dominant mechanism for intensities in the range from 10^{12} to 10^{16} W/cm^2 [36].

The rate W of the multi-photon ionization can also be described as the differential of the free electron density,

$$W(I, \hbar\omega, E_g) = \sigma_n I(t)^n, \tag{2.3}$$

where $\sigma(n)$ is the n-photon absorption cross section described with intensities, which is measured in photons cm^{-2} s^{-1}. For n-photon absorption cross section, the unit is expressed as [cm^{2n}s^{n-1}] [39, 40].

In tunneling ionization, the electric field of the laser is comparable to the binding potential of the atom and can suppress the potential so that the electron can escape from the potential well by the suppression. This process is expected to become dominant if the peak laser field strength exceeds the atomic field strength. Figure 2.5 illustrates two regimes of photo-ionization, tunneling and multiphoton ionization.

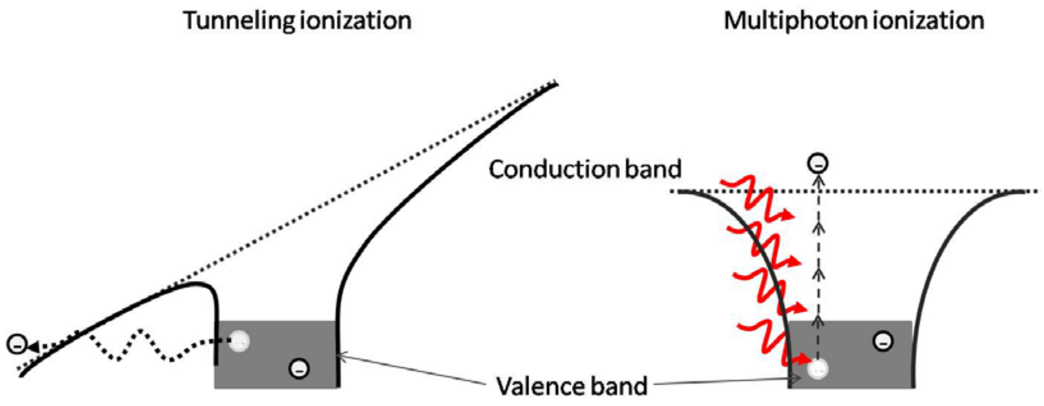

Figure 2.5 Schematic diagram of (left) Tunneling ionization and (right) multiphoton ionization

These two ionization processes are characterized by the Keldysh parameter γ [41] given as Eq. (2.4)

$$\gamma = \frac{\omega}{e}\left[\frac{mcn_o\varepsilon_o E_g}{I}\right]^{1/2}, \tag{2.4}$$

where m and e are the mass and charge of the electron respectively, c is the speed of light, n_o is the refraction index of the material, ε_o is the permittivity in vacuum, E_g is the bandgap energy of the material, and ω and I are the frequency and intensity of the laser, respectively. If the value of γ is greater than 1.5, the ionization follows multiphoton ionization, otherwise tunneling takes place. Because of its nonlinear nature, the absorption is confined only to the tightly focused volume in the medium.

2.2.3 Contribution of avalanche and photo-ionization to free electron generation

The electron excitation kinetics is determined by the interplay of the photo-ionization and avalanche ionization, which can be described by [34]

$$\frac{dn_e}{dt} = \sigma_n I(t)^n + \alpha I(t) n_e \,. \tag{2.5}$$

Figure 2.6 shows the electron density of a transparent material irradiated by a single pulse. As is seen, the free electron density populated only by multiphoton ionization reaches a maximum at the peak of the pulse. However, the plot shows that the free electron density resulting from the interplay between multiphoton and avalanche ionization grows to reach a maximum throughout the pulse duration (FWHM of the pulse). Consequently, the latter results in the higher electron density (approximately three orders of magnitude).

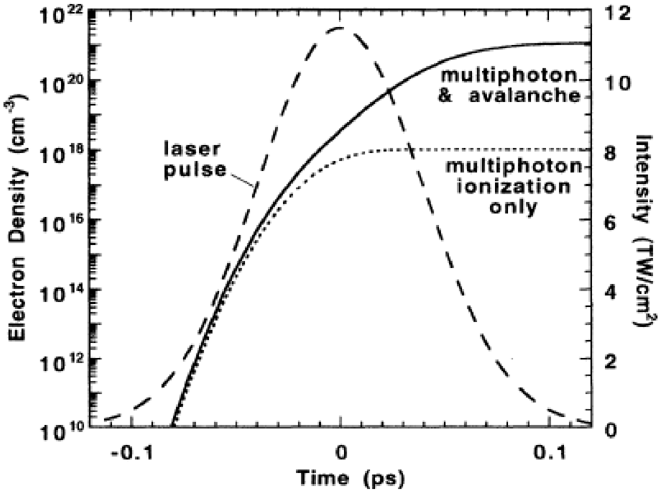

Figure 2.6 Electron density of the material irradiated by a ultrashort pulse with/without a participation of avalanche ionization. From [32].

2.3 Heat accumulation effect

The thermal diffusivity D [cm^2/s] of a given material is described as

$$D = \frac{\kappa}{\rho c_p}, \tag{2.6}$$

where κ is the thermal conductivity [W/cmK], ρ is the density of mass [g/cm^3], c_p is the specific heat capacity [J/gK] of the material [42]. Values of the thermo-physical properties of various materials including metals, semiconductors and optical glasses are listed in Appendix A. The thermal diffusivity of common transparent dielectrics is the order of ~10^{-3} cm^2/s which is ~100 times smaller than metals. Thus, localized heat accumulation in transparent dielectric materials becomes significant when the dielectrics are subjected to the high repetition rate irradiation, whose pulse-to-pulse interval is shorter than the diffusion time of the material, the order of a few μs in general case. Figure 2.7 illustrates the difference of material response with 1 kHz and 36 MHz laser exposure. As depicted, the pulse interval of 1 kHz laser is 1ms which is longer than the material response time, therefore every pulse behaves single pulse irradiation while the interval of 36 MHz laser is shorter than the thermal response time so that the next pulse comes even though the material is not cooled enough. Consequently the required energy to excite material is reduced by heat accumulation from prior pulses. Localized heat accumulation is therefore the unique feature of the high repetition rate pulses.

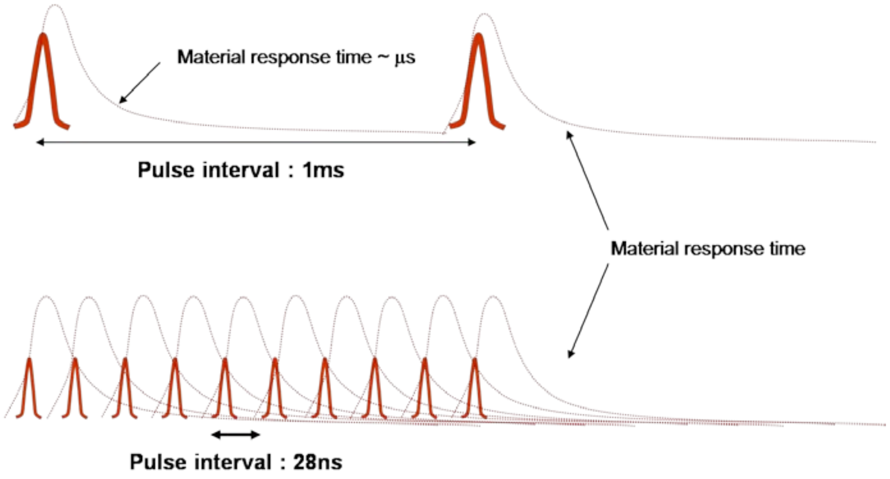

Figure 2.7 Comparison of the material response at 1 kHz vs. 36 MHz pulses

There are several aspects on the heat accumulation in femtosecond laser materials processing. In the case of laser micromachining seeking sub-micron precision quality with a minimized heat affected zone (HAZ), heat accumulation may undermine the advantage of femtosecond machining. However, in the other case, one can actively introduce heat accumulation to process fragile high bandgap materials by reducing the formation of a shock wave due to use of a low applied pulse energy; this offers the benefit of an enhanced photo-induced response (reduced damage threshold). Furthermore, incorporating heat accumulation may enhance (suppress) certain processes such as photo-thermo-chemical reactions locally. The details of these mentioned aspects are discussed in the following paragraphs.

Schaffer et al. investigated the localized heat accumulation in bulk zinc-doped borosilicate (Corning 0211) using a 25 MHz repetition rate pulses as a function of number of pulses [40, 41]. Optical images of the permanent structures produced by a single pulse and multiple pulses are seen in Figure 2.8. The structures in (a) have approximately sub-micron diameter, which is predicted by the spot size of the NA(=1.4) while the structures in (b) show drastically increased diameters. It is also noticed that the structures created by successive pulses show multiple rings implying regions of different refractive index change.

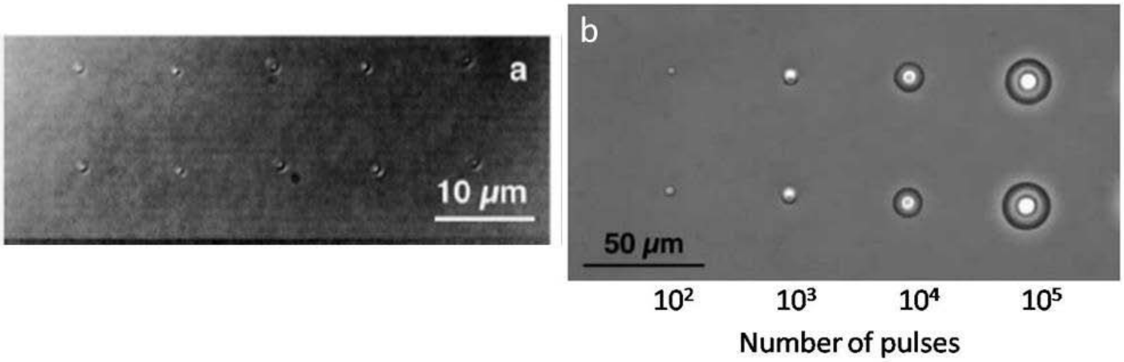

Figure 2.8 Optical microscopic image of structural modification by a 25 MHz oscillator (NA=1.4) (a) single pulse by 10 nJ, 100 fs and (b) by 5 nJ-30 fs pulses. Note that the scales are different. (modified from [43, 44])

Gattass et al. extended the investigation to soda lime glass by the use of an acousto-optic (AO) gate to obtain variable repetition rates from a 25 MHz oscillator [45] . Eaton et al. also reported a heat accumulation effect in borosilicate glass at a range of 0.1 – 1 MHz by burst irradiation using an AO modulator [46]. Figure 2.9 shows the effect of heat accumulation produced by a variable repetition rate femtosecond laser. As shown in the micrograph, researchers observed \initiation of melting due to the cumulative heating started at 200kHz which became significant over 500 kHz. It can also be seen that there is significant difference of the ablated spot size between 200kHz and 500kHz implying that heat accumulation effect become dominant at > 500KHz.

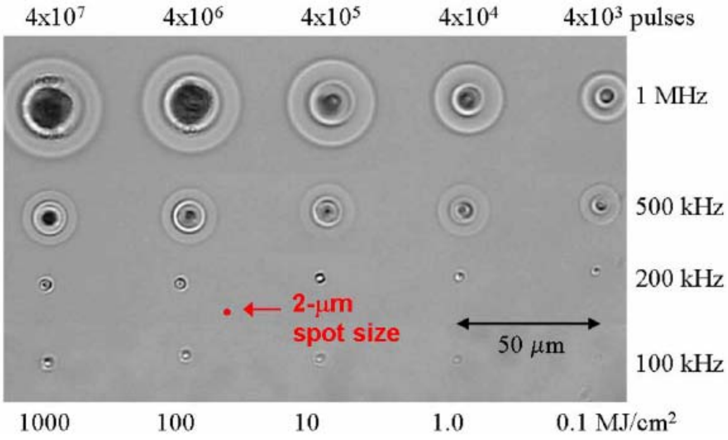

Figure 2.9 Ablation threshold map as functions of repetition rate and number of pulses. AF45 borosilicate irradiated with 450 nJ pulses from 1045 nm femtosecond laser. From [46]

Figure 2.10 depicts a calculation of the material temperature as a function of pulse number at different repetition rates calculated with thermal diffusion coefficient of borosilicate glass. As is seen, a heat accumulation effect increases the material temperature significantly higher than non-thermal process at 100 kHz.

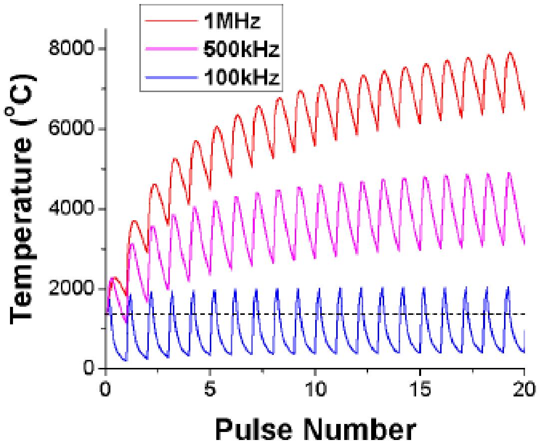

Figure 2.10 Heat accumulation effect. Finite-difference model of glass temperature at a radial position of 2 µm from the center of the laser pulse. From [46]

Both results reveal that cumulative local heating plays an important role in photo-induced structural change at high pulse repetition rate. In general, heat accumulation is not precisely controllable since the effect is closely related to the thermal properties of the materials matrix. Hence it may cause material degradation and distortion in post-processed region.

Differential interference contrast (DIC) optical microscopic images of directly written grating structures embedded in borosilicate glass are shown in Figure 2.11 as an example of excessive cumulative heating produced. The gratings were written using the same objective lens with pulse energies of ~1800 nJ at 100 kHz and ~375 nJ at 500 kHz respectively. Whereas well defined fine structures are created at 100 kHz, it can clearly be seen that the excessive cumulative heating results in a more complicated secondary pattern at 500 kHz with the smaller pulse energy and the similar laser dose. It is thought that an increase of the local temperature by cumulative heating resulted in melting, causing localized high pressure followed by the generation of a shock wave. Thus the beam propagation mode is not uniform at 500 kHz while the guiding mode is uniform and evenly localized at 100 kHz. These results directly show that the management of cumulative local heating is important to the fabrication of desired structures at high repetition rate.

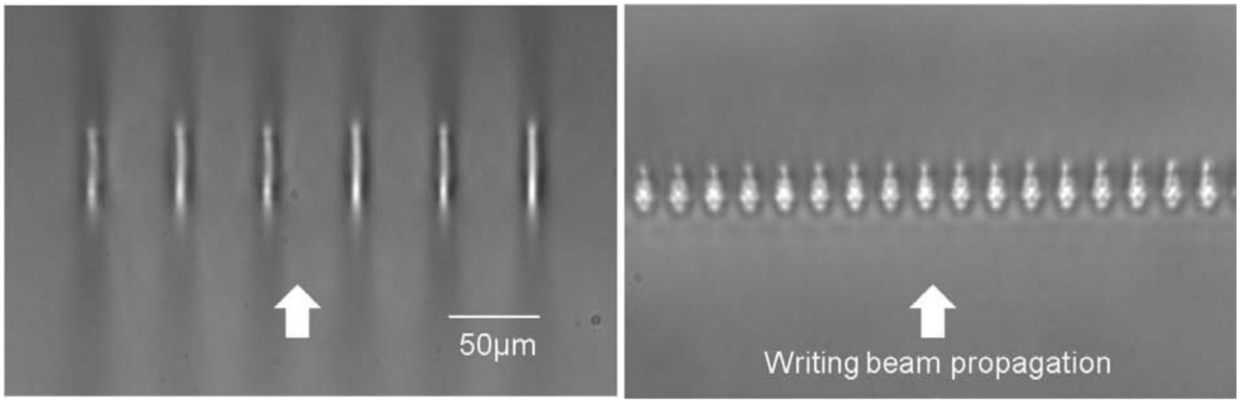

Figure 2.11 Optical images of the cross-section of the laser generated structures

using a focusing objective with NA=0.4 at (a) 100 kHz (b) 500 kHz

Lastly, as is mentioned above, localized cumulative heating can enhance photo-thermo-chemical reaction in the material, which may be advantageous for development of opto-chemical sensors and similar applications utilizing thermo-catalytic reaction. As an example of the former, Ag clusters can be formed in Ag^+ doped glass from the photo-reduction of Ag^+ to Ag^o followed by an aggregation process driven by heat accumulation effect at MHz regime femtosecond laser irradiation. In other words, the use under MHz regime removes the post heat treatment, which is not observable at 1 kHz repetition rate regime, where requires a post annealing process for the aggregation of reduced silver atoms is required. The detail of the experimental result on the formation of Ag clusters will be presented in the Chapters 4 and 7.

CHAPTER 3 : FEMTOSECOND LASER DIRECT WRITING

This chapter reviews the major femtosecond laser direct writing techniques currently available, paying a special attention to those novel laser and optical techniques, which rely on a precise control of the femtosecond laser-matter interaction for successful device fabrication. It also presents the femtosecond laser systems used for this research, with their specifications.

3.1 Femtosecond laser direct writing techniques

The laser direct writing technique has been widely used in various areas of laser materials processing for its convenience and flexibility. It produces arbitrary patterns using a tightly focused beam, which is used as “optical pen” while photolithographic technique only produces pre-determined patterns through photo-masks, which are expensive consumable parts. This feature makes the technique suitable for the fabricaton of customized devices and prototypes by simply changing the computer-generated writing pattern and optical configuration. In addition to this advantage, femtosecond laser direct writing (FLDW) offers a capability of 3-D patterning in transparent materials owing to the nonlinear absorption processes, discussed in the previous chapter. Figure 3.1 illustrates how embedded 3-D arbitrary patterning is available in FLDW by a comparison of the nonlinear absorption to the linear absorption process. The material (a) is supposed to have an absorption band at the incident wavelength while the material (b) to be transparent to the incident wavelength, which means the absence of linear absorption. When ultrashort pulse are incident, the nonlinear absorption in (b) is localized within a focal volume where the laser intensity exceeds the threshold of structural modification while the linear one is not confined, even though there is stronger absorption at the focal region in (a).

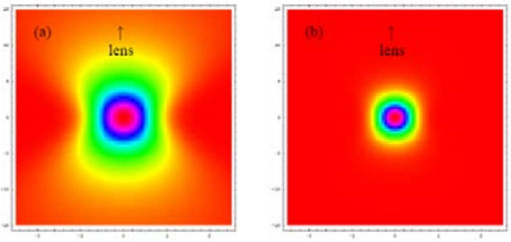

Figure 3.1 Schematic diagram of linear (a) vs. nonlinear absorption (b) in a transparent medium. From [47]

The least requirement for 3-D FLDW is therefore high transparency of the material and high intensity of the laser pulse. The combination of a transparent dielectric material and a femtosecond laser equipped with a focusing optics is then the minimum utility for the 3-D FLDW to fulfill those requirements. With these circumstances, nonlinear absorption is confined only in a voxel. A voxel can be used as an “optical pen” to write desired photo-written 3-D structures in a transparent medium. In addition, this fabrication protocol allows us to control over the laser-matter interactions in microscopic scale by well defined external parameters (laser and optical parameters). The properties of the structure are highly dependent on the optical parts and the irradiation scheme. In general, the dimensions (e.g. line width) and properties of the laser-written structure, such as photo-induced refractive index change of waveguides, are controlled by the following writing parameters.

- Laser parameters (laser wavelength, pulse width, laser power, repetition rate)
- Mechanical parameters (translation speed and precision of the stage)
- Optical parameters (NA of lenses, beam delivery optics)

In other words, those given writing parameters are the driving factors in FLDW, implying that a wise control of those parameters guarantees successful fabrication using FLDW. This section discusses the various techniques of controlling those writing parameters.

3.1.1 Longitudinal vs. transverse writing

There are two irradiation schemes in 3-D femtosecond laser direct writing. One is longitudinal writing and the other is transverse writing. As illustrated in Figure 3.2, the direction of the structural modification is the same with the laser propagation in longitudinal writing, while the modification is formed perpendicularly to the laser propagation in the transverse writing.

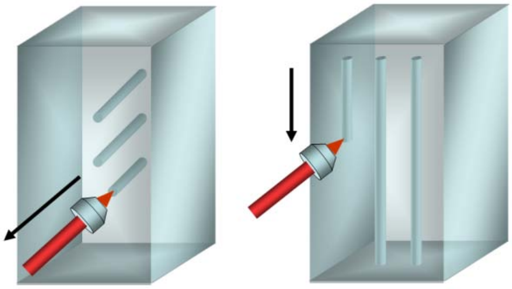

Figure 3.2 Schematic diagram of longitudinal writing (left) vs. transverse writing (right)

The different irradiation geometries cause different shapes of the structure. The longitudinal writing produces circular structure cross-sections, which would be useful for waveguide writing. However, as is noticed in Figure 3.2, the working distance of the objective limits the length of the waveguide. For instance, the 10X objective lens (N.A. = 0.25), which was used in this study, has the working distance of about 7mm which implies the maximum length of the structure.

In transverse writing, the limiting factor of the length of the written structure is not the working distance of the objective lenses, but the stroke of the translation stage and the sample length. The transverse writing scheme is thus suitable for large area structuring. In this scheme, the confocal length (twice of the Rayleigh length), which is determined by the NA of the objective lens, can be another limiting factor depending upon the application. Figure 3.3 describes the difference between low and high NA lenses, which affects the shape of the voxel and resulting structures.

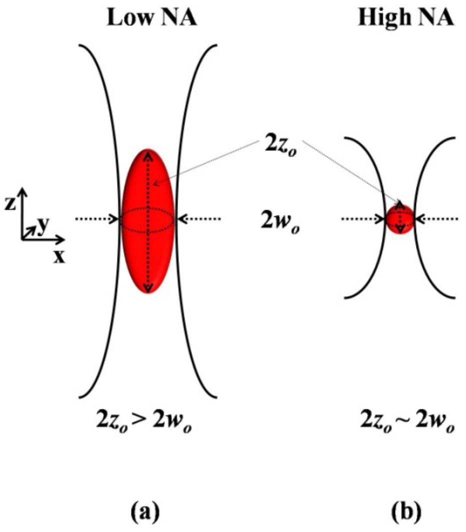

Figure 3.3 The schematic illustration of the comparison of the voxel length by low NA and high NA objectives

In the longitudinal writing, the irradiation profile follows the cross-section of the writing beam in the x-y plane, which is normal to the propagation direction along the z axis. This means that the irradiation profile is always circular regardless of the NA of objective as mentioned above. In transverse writing, the irradiation profile is the cross-section in the x-z plane, which is elliptical in general.

In addition to the difference of irradiation cross-section, the beam overlap rate is also described differently for each writing scheme. In Figure 3.3, the focal volume V of the voxel produced by a microscope objective can be estimated as $V \approx 2\pi w_0^2 z_0$ with a beam waist w_0, Rayleigh length z_0 and laser wavelength λ. Then the beam overlap rate r is described as Eq. (3.1),

$$\begin{aligned} r_t &= 1 - \frac{v}{2w_0 f} \\ r_l &= 1 - \frac{v}{2n_o z_0 f}, \end{aligned} \tag{3.1}$$

where f is the repetition rate of the laser system, v is a translation speed of the stage, n_o is the refractive index of the medium, r_t is the rate for transverse writing and r_l is for longitudinal writing.

The Beam overlap rate is an important fabrication factor determining the dimension and resolution of the structure. Figure 3.4 shows an example of the longitudinal writing performed in bulk PMMA, using LS I and a 10X objective (NA=0.25). As expected, perfect circular waveguides are produced. It is also noticed that the line widths of the waveguides are different although same objective lens was used. That is due to the different overlap rate varied by different writing speeds, 20, 30 and 40μm/s. It shows clearly that longitudinal writing (or alternatively a high NA (oil immersion) lens) is a suitable writing scheme in many applications, which require well defined waveguide structures. For those applications, transverse writing with low NA objectives may cause difficulty generating nicely shaped waveguides competitive against the longitudinal scheme due to the long Rayleigh length of the lenses compared to beam waist.

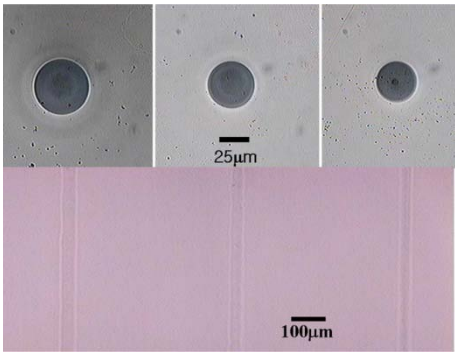

Figure 3.4 The side view and cross sections of waveguides in PMMA. The diameter of the waveguide varies with the writing speeds. (from left to right, 20 μm/s, 30 μm/s and 40 μm/s)

For other applications seeking an elongated modification region (it is the main focus of this dissertation), transverse writing using low NA objectives are a solution. Figure 3.5 shows the microscopic images of the modification lengths variation of gratings produced by the transverse writing scheme. The gratings were produced in a borosilicate glass as functions of NA of objectives and laser pulse energy. A femtosecond laser system(LS III) with a repetition rate of 100 kHz created those gratings using various objective lenses from NA=0.2 to NA= 0.4 (a-c). As is seen in Figure 3.5 (a-c), the difference of the lengths as a function of NA of the objectives is observed. The writing speed and pulse energy were kept constant at 0.5 mm/s and ~2.4 μJ. The modification length at NA=0.2 is approximately twice as long with respect to the length at NA=0.4. Figure 3.5(d-g) shows the induced refractive index (Δn) variation of the modification. In this case, Δn is induced as a function of the pulse energy (150 ~ 1500 nJ) under the same focusing geometry (NA=0.4). It is clearly seen that the guided region from (d) to (g) becomes brighter, which means higher guided light due to higher laser-induced Δn in (g). It implies that the higher pulse energy induces higher refractive index change. The demonstration shown in Figure 3.5 indicates that the dimension and the optical properties of the laser produced structures can be controlled quantitatively by a single or combination of fabrication parameters listed above. The following chapters will discuss the detail of the relationship between the NA and diffraction efficiency of the diffractive optical element written by this scheme.

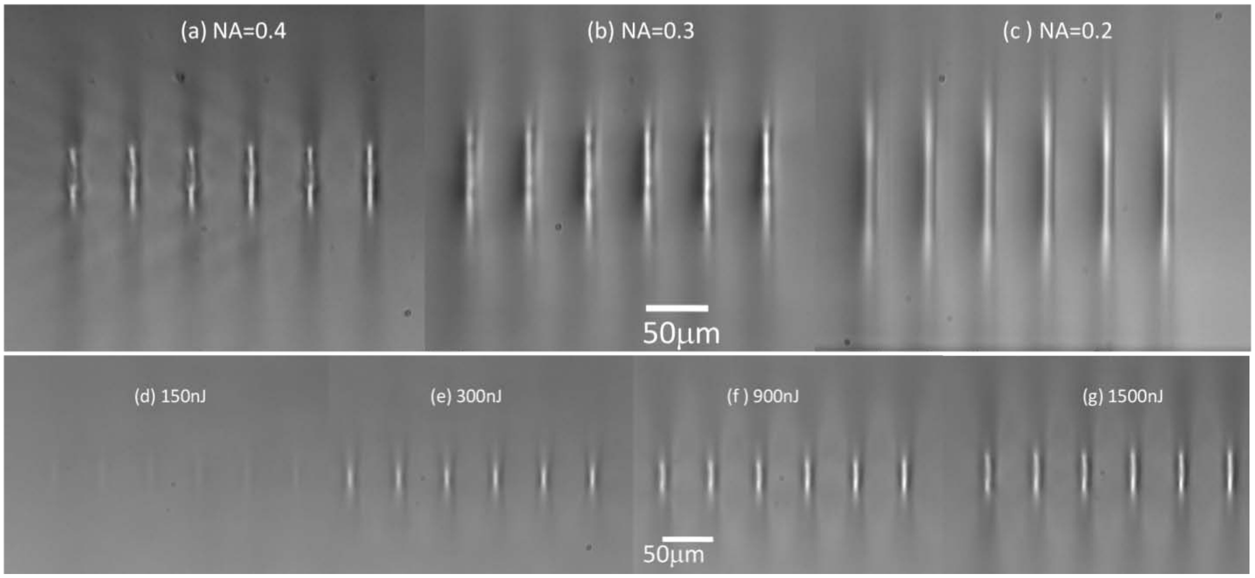

Figure 3.5 Optical images of the cross-section of the generated structures using various focusing objectives with (a-c) numerical aperture variation at 100 kHz (a) NA = 0.4 (b) NA = 0.3 (c) NA = 0.2, (d-g) pulse energy variation (NA=0.4) pulse (d)E_p=150 nJ (e) E_p=300 nJ (f) E_p=900 nJ (g) E_p=1500 nJ

As discussed in this section, the wise choice of the laser writing layout and irradiation parameters as well as appropriate fabrication parameters is the key for the successful fabrication. However, there is always a challenge in choosing appropriate parameters because of the limitation of resources such as a limited choice of NA and a lack of the laser power causing low throughput. One way to overcome those limitations is beam (pulse) shaping. The following section discusses various beam (pulse) shaping techniques employed in laser direct writing to achieve the desired results on each application.

3.1.2 Beam and pulse-shaping

Although femtosecond lasers have been proved as a versatile means to producing micron size 3-D volumetric structures within a substrate, there are several limitations and challenges which inhibit FLDW from being adopted in industrial applications.

- An elongated beam cross-section in transverse writing
- A short modification length with the material
- A low laser-induced refractive index change in most materials
- The intrinsic diffraction limit
- It is a slow, serial process
- Long fabrication time (low throughput)

It is not an easy task with a single writing setup to address all of these requirements at once. The solution can be the selection of appropriate beam (pulse) shaping in the spatial (and temporal) domain respectively, which allows us to overcome many of the limitations mentioned above. Here, various beam (pulse) shaping methods are reviewed and their advantages and limitations are discussed.

3.1.2.1 Spatial beam shaping

Spatial beam shaping is a way to reshape a laser beam profile from its initial form, which is mostly a Gaussian profile, to appropriate profiles which are required to the applications. For example, many laser micromachining applications utilize beam homogenizers to produce uniform irradiation such as a top hat mode in order to improve the machining uniformity [48, 49]. Another example is the use of DOEs to generate multiple outputs. For instance, gratings and custom designed diffractive optical elements could be used to split the input beam into multiple outputs with various intensities depending on the diffraction efficiency of DOEs [6]. These elements enable parallel processing, thereby increasing the throughput of the machining system.

There are also many challenges in FLDW caused by the limitations of geometrical optics. In waveguide fabrication, as discussed in previous section, either longitudinal writing or transverse writing with high NA objective (mostly oil immersion type) is preferable to achieve a round cross-section. However, it is not practically useful because of the short working distance of objective lenses and/or the use of index matching fluid. Although, transverse waveguide writing using low NA objective lenses is more favorable in practical applications, it suffers from the elliptical waveguide cross-section as seen in Figure 3.5. Osellame et al. demonstrated a solution to improve the poor waveguide profile by use of cylindrical lens to introduce an astigmatic aberration [50]. Figure 3.6 shows their system with a cylindrical lens. They showed much improved waveguide cross-sections even though the diameter of the waveguide was increased. However, the setup in Figure 3.6 is assumed to be sensitive to the misalignment of a cylindrical lens as it controls the astigmatic aberration related to the roundness of the waveguide. Ams et al. adopted the idea and simplified the setup by replacing a cylindrical lens with a slit having a width of 500 µm [51]. Although the use of a slit results in laser power loss, it showed similar improvement on the waveguide profile with a use of a low NA objective lens (NA=0.46). Figure 3.6 shows the guided beam profile with and without a slit. It is clearly seen that the guiding region is greatly improved and appears perfectly circular.

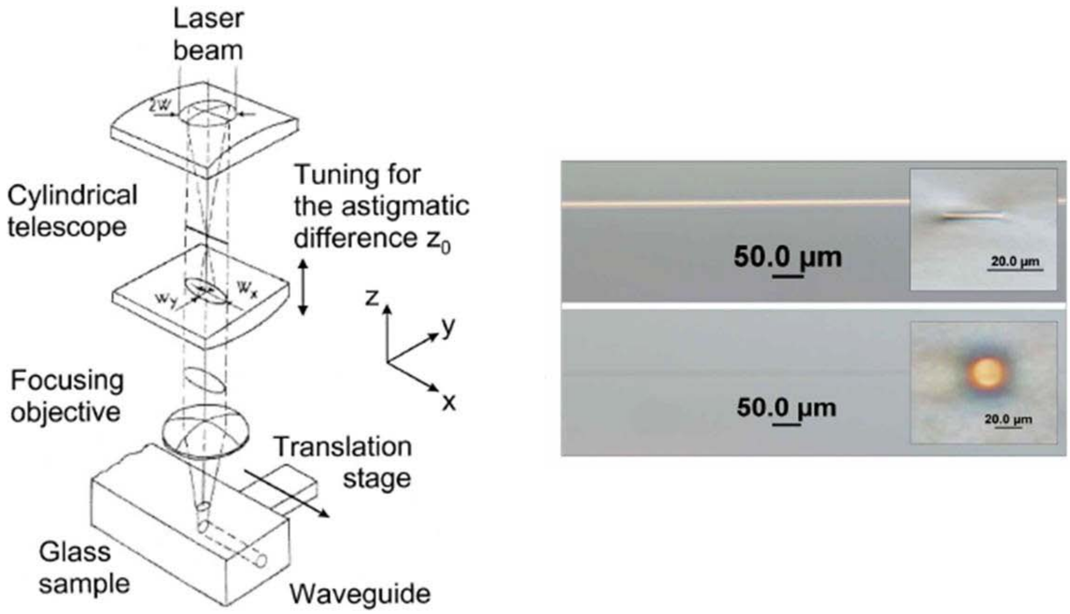

Figure 3.6 Astigmatical beam shaping using a cylindrical lens (left, From [50]) and a waveguide written in a phosphate glass with/without a slit with width of 500 µm(right, From [51])

Another method of beam shaping is through the use of axicons. Axicons have been widely used in trepanning drilling [52], optical tweezers [53] and many other applications requiring a ring shape beam profile. Figure 3.7(a,b) shows a configuration of an axicon and its ring-shaped intensity profile. Another advantage of using axicons is their very long beam waist. Figure 3.7(c,d) shows the intensity profile of the setup with an axicon used for the fabrication of very thin and long micro-channels [54].

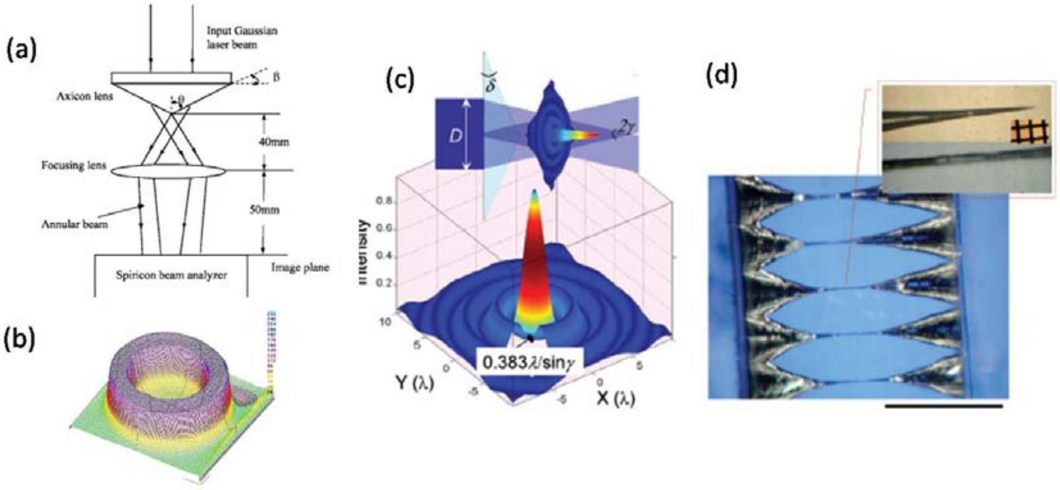

Figure 3.7 A setup using axicon(a) and its beam profile (b) (c-d) micro channel formation using an axicon (From [52, 54])

Splitting an input beam into multiple output beams is another pathway to improve not only the throughput, but also the positional accuracy of a desired sub-pattern. Here we discuss several examples of the use of DOEs and interferometric methods in femtosecond laser processing. Figure 3.8 shows the laser micro-patterning using a four-level phase DOE which has 22 focal points with a partial periodic structure, demonstrated by Kuroiwa et al. [6]. The researchers used a DOE designed by a computer generated hologram method for the wavelength at 800nm.

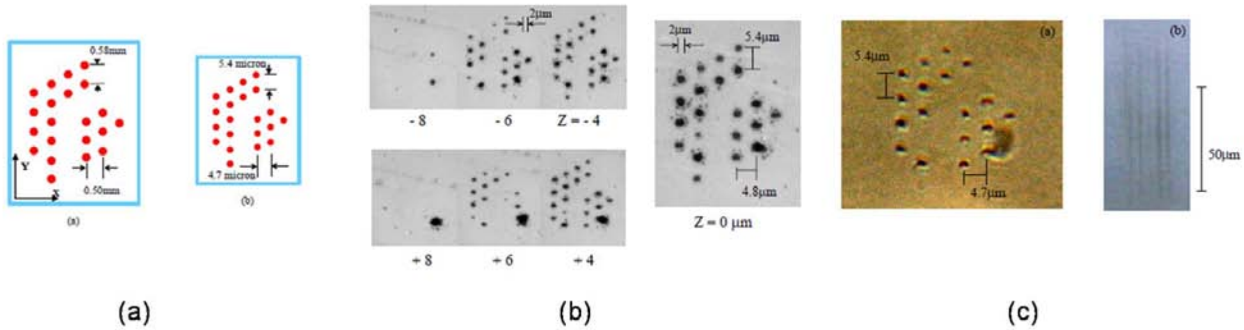

Figure 3.8 A four-level phase DOE used for the laser drilling of SiO_2 glass. (a) focal shape of the DOE pattern (left-without objective, right-with objective), (b,c) optical

microscope images of (b)ablation pattern on the surface of SiO_2 glass (c) embedded structures within SiO_2 glass (From [6])

Another case is the use of DOEs to produce multiple beam interferometer, demonstrated by Misawa et al., for either holographic recording[55, 56] or multi-beam recording [57]. Figure 3.9 shows the universal configuration using a DOE for both recording types. The sample position 1 in Figure 3.9 is to irradiate the sample by a holographic interferogram while position 2 is for the multi-beam scheme exposure. The laser-written grating shown in Figure 3.9 was recorded in bulk As_2S_3 by direct multi-beam writing (31 inline beams) inducing photo-darkening. The same exposure strategy was used to create 2-D micro rods using an interferogram via two-photon polymerization, which is also shown in Figure 3.9(right).

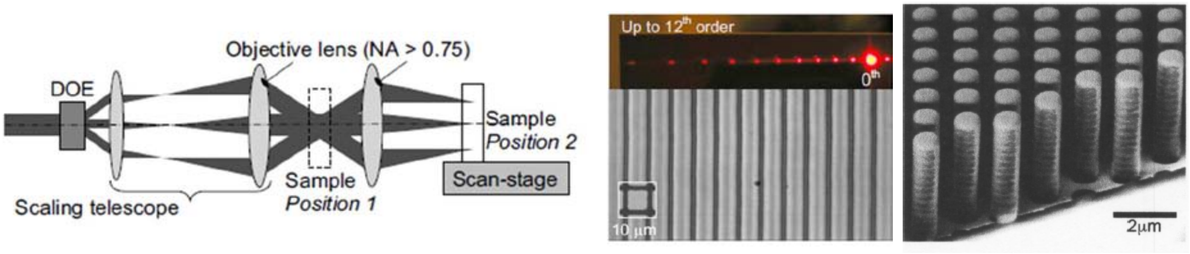

Figure 3.9 Holographic writing method using a diffractive beam splitter (left) and photo-written grating (mid) and 2-D photonic crystal (right) demonstrated by Misawa group. From [55-57]

Kawamura et al. also demonstrated a similar technique based on holographic recording to create a micro grating in fused silica, which is shown in Figure 3.10. The colliding angle between two beams was varied from 15~158°, corresponding to the fringe spacing of 3~0.43µm, shown in Figure 3.10 (b) [58]. The second grating, which is in Figure 3.10 (c), was recorded by a double exposure [59]. Once the hologram was recorded in one direction, the sample was rotated

90° to record the same grating in the perpendicular direction, so that the resulting pattern shows buried periodic 2-D micro structure as seen below.

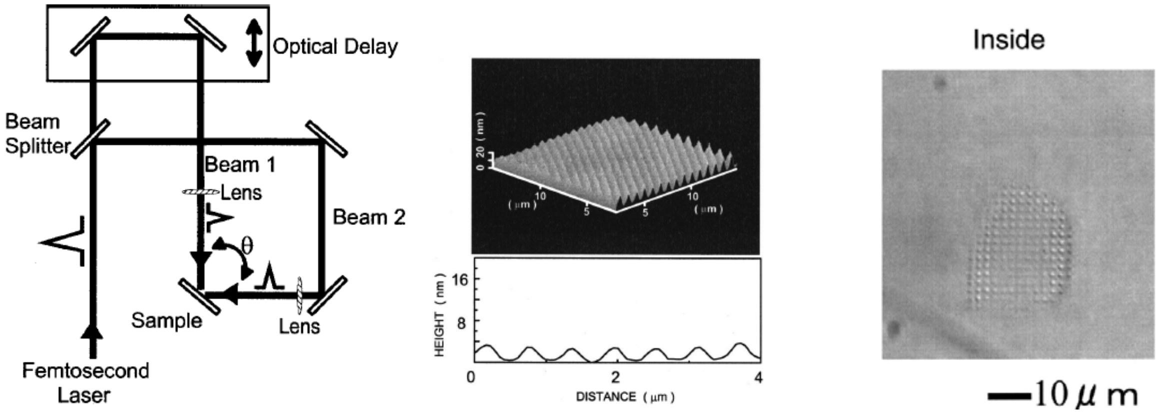

(a) (b) (c)

Figure 3.10 (a) Holographic recording setup using two beam interferometry and (b) surface and (c)volumetric gratings written in fused silica (From [58, 59])

3.1.2.2 Pulse shaping in the temporal domain

As discussed above, the primary strategy of the beam shaping is to modify the input beam's spatial intensity either by diffraction, interference or any other method. However, it is not closely related to the materials properties. Pulse shaping is also the reformation of the beam intensity, but in the temporal domain. It can be related to the materials properties such as thermal diffusivity and characteristic time constants of energy transfer between elementary particles and plasma formation. Thus the aim of the pulse shaping is to enhance the photo-response of materials to increase the efficiency of modification.

One of the commonly used techniques in FLDW is burst mode processing. The key idea of the technique is converting a single input pulse into a burst, which consists of multiple sub pulses with a sub-pulse interval τ. In general, τ is much shorter than the inverse of the repetition rate of the laser system. Burst mode pulses are generated either by implementation of a two (multiple) beam interferometer or by use of acousto-optic (AO) modulators, which enables fast gating. In addition, the former has an advantage to have arbitrary sub-pulse interval depending on a delay stage. However, the alignment required is very sophisticated. The advantage of the latter scheme is the simplicity and easy configuration as well as quasi-arbitrary burst repetition rate. In this case, the sub-pulse interval is not variable since the interval is the same as initial repetition rate of the laser system. The interferometric configuration has been demonstrated using the low repetition rate laser systems (a few kHz) and AO modulators are widely used for the MHz repetition rate regime. The realization of the former has been demonstrated with a few different schemes by Herman et al.[60], Marjoribanks group [61, 62], Siders et al. [63] and the Laser plasma laboratory in CREOL [64, 65]. The typical implementation based on interferometry is shown in Figure 3.11.

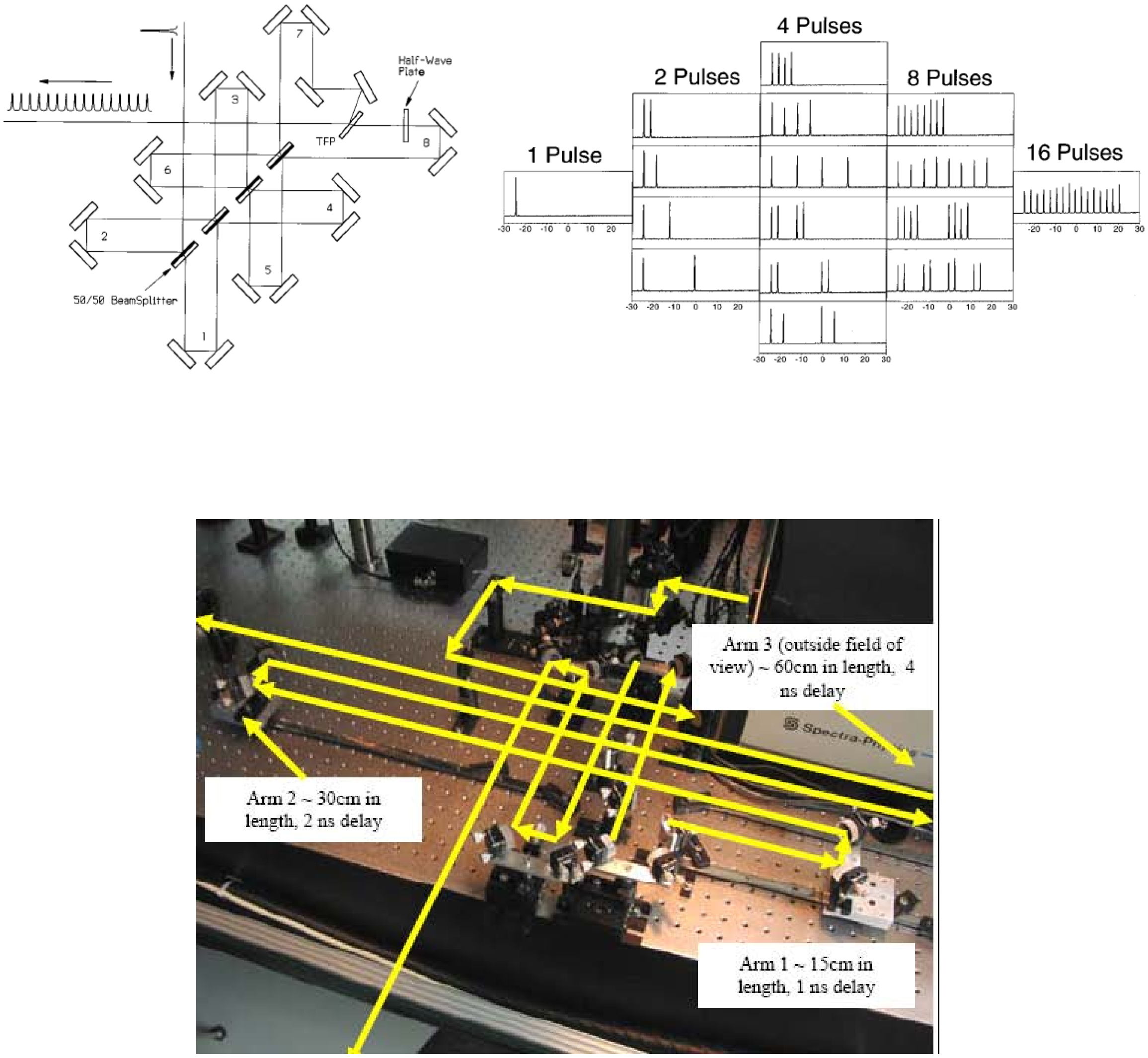

Arm 3 (outside field of view) ~ 60cm in length, 4 ns delay

Arm 2 ~ 30cm in length, 2 ns delay

Arm 1 ~ 15cm in length, 1 ns delay

Figure 3.11 Interferometric configuration for burst pulse generation (From [63]) and 8-pulse Hyper Michelson interferometer built in the laser plasma laboratory in CREOL

The schematic of the use of AO modulator is illustrated in Figure 3.12. The implementation has been demonstrated by Gattass et al.[45], Eaton et al. [46], Canioni et al.[66] and other research groups.

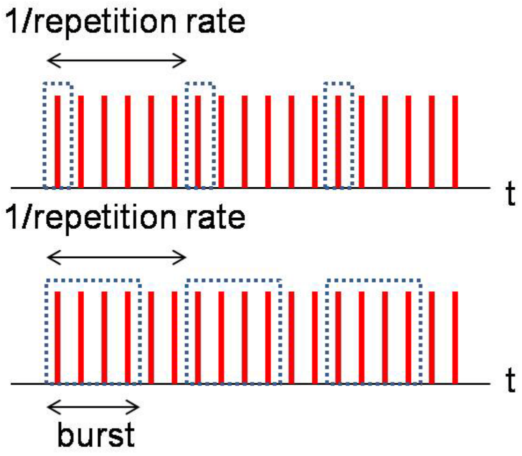

Figure 3.12 The scheme of the gating with an AO modulator for burst pulse generation.

Figure 3.13 shows the comparison of the etch rate for single pulse and burst mode drilling [60]. Two advantageous aspects of burst mode drilling are clearly seen in the figure. One is the decease of the laser fluence for the onset of drilling. The other is the steeper slope of the etch rate as a function of laser fluence. These attributes of burst mode drilling promises more efficient drilling since the burst pulses enhance the photo-induced response of material either by stimulating the formation of electron plasma or by increasing the local temperature due to the heat accumulation. Figure 3.14(a) shows that the drilled diameter is increased and the onset of the structural modificaiton is decreased as the number of the sub-pulse increases. It is probably due to the efficient local heat accumulation in focal volume shown in Figure 3.14 (b).

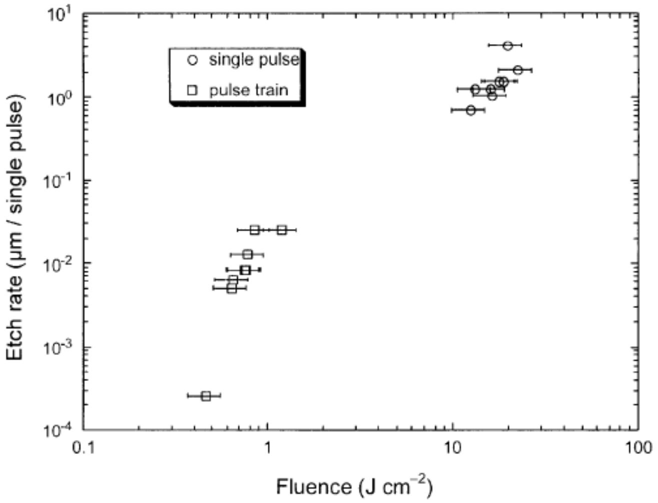

Figure 3.13 The etch rate of single pulse vs. burst mode drilling (From [60])

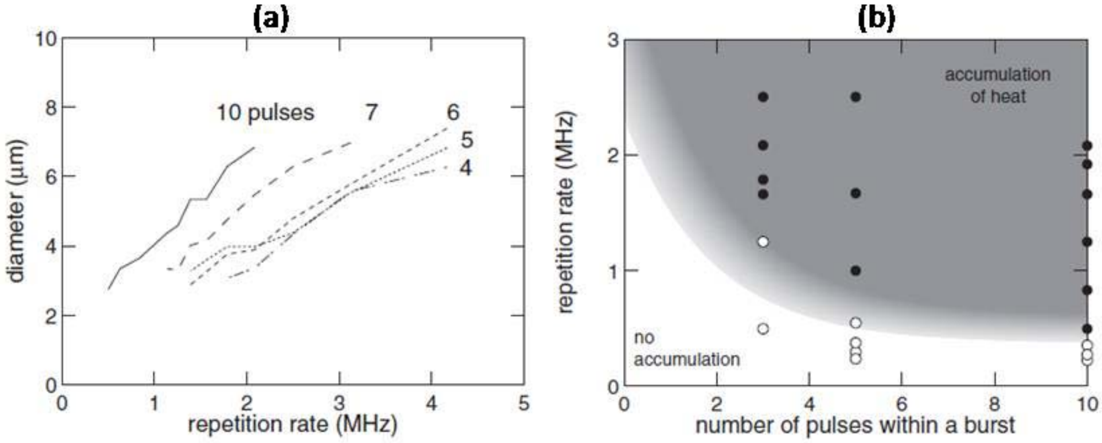

Figure 3.14 Drilled hole by a burst drilling with different sub-pulses. From [67]

Burst pulse processing has advantages not only in the increase of processing efficiency, but also for the improvement of processing quality. Figure 3.15 shows the difference of single and burst pulse drilling quality on the borosilicate glass. It is clearly noticed that the edge of burst pulse drilled hole is much smoother than single pulse drilled hole at the same fluence. It is due to lower sub pulse energy generating weaker shockwaves and less debris to the substrate even though the total fluence of a burst is kept the same with the single pulse.

As mentioned briefly above, the control of the sub-pulse interval and burst pulse repetition rate is important since it is closely related to the intrinsic material properties such as thermal diffusivity and plasma formation. This infers that a sub-pulse interval should be optimized for the material of interest. Figure 3.16 shows the difference of the burst pulse ablation as a function of repetition rate and pulse interval on a tooth and on an alumina ceramic substrate respectively.

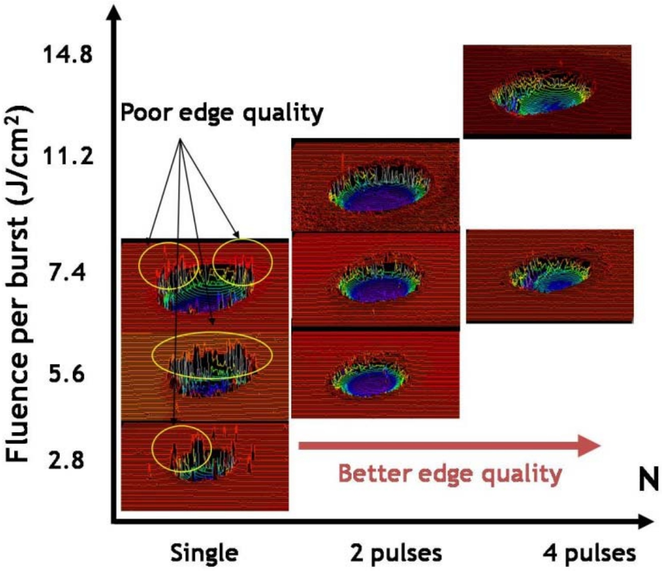

Figure 3.15 Surface profile of drilled holes via single pulse and burst pulse (Borosilicate glass)

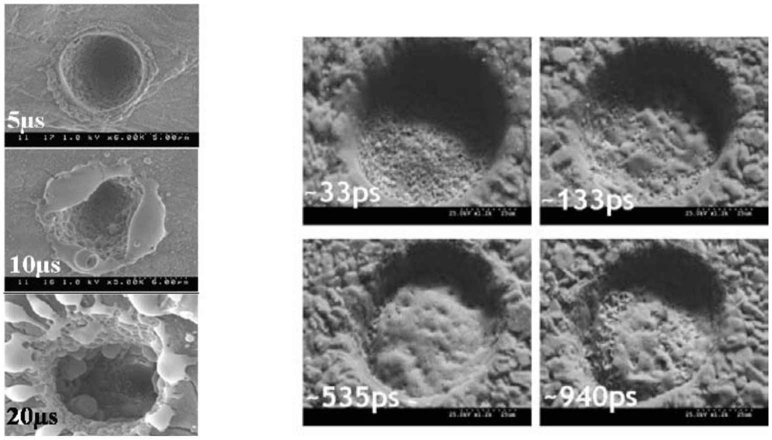

Figure 3.16 Burst mode ablation of tooth with ultrashort pulsetrain-bursts with 5,10 and 20 µs (From [61]) and alumina ceramic. (produced by Laser plasma lab, From [65])

3.2 Femtosecond laser direct writing facilities used in this study

In this dissertation, three femtosecond laser systems were used for the different requirements of investigations on a variety of materials and applications. The first system (LS I) is a custom built extended cavity Ti:Sapphire oscillator with 26MHz rep. rate at ~800 nm center wavelength. The second system (LS II) is a regenerative amplified Ti:Sapphire laser (Spitfire, Spectra Physics) with the repetition rate of 1 kHz at 800 nm center wavelength. The third system (LS III) is an Yb-doped femtosecond fiber laser (FCPA µJewel D-400-VR, IMRA America Inc.) operating at various repetition rates from 100 kHz up to 5 MHz. The center wavelength is at ~1043nm with the pulse width of around 450fs. Table 3.1 shows the details of these laser systems. With these three systems, customized laser irradiation in the low/ intermediate/ high intensity regimes at various repetition rates is available on the materials of interest depending upon the target materials for each application.

Table 3.1 Specifications of laser systems

	LS I	LS II	LS III
Type	Ti:Sapphire	Ti:Sapphire	Yb doped fiber
Center wavelength (nm)	800	800	1043
Pulse width (fs)	~60	~120	400 ~ 450
Rep. rate (MHz)	26	0.1	0.1 – 5
Pulse energy (Max) (µJ)	<0.02	~1000	< 5[1]

---

[1] At 100 kHz

These laser systems are integrated with laser direct writing systems consisting of computer controlled 3 dimensional writing stages (VP-25XA, Newport and ALS-130, Aerotech), and beam delivery optics including microscope objectives (NA=0.1~0.65) to deliver the femtosecond beam to the sample. A LabView based program was developed to control the 3-D stages in order to produce various diffractive patterns. Figure 3.17 depicts the laser writing setup.

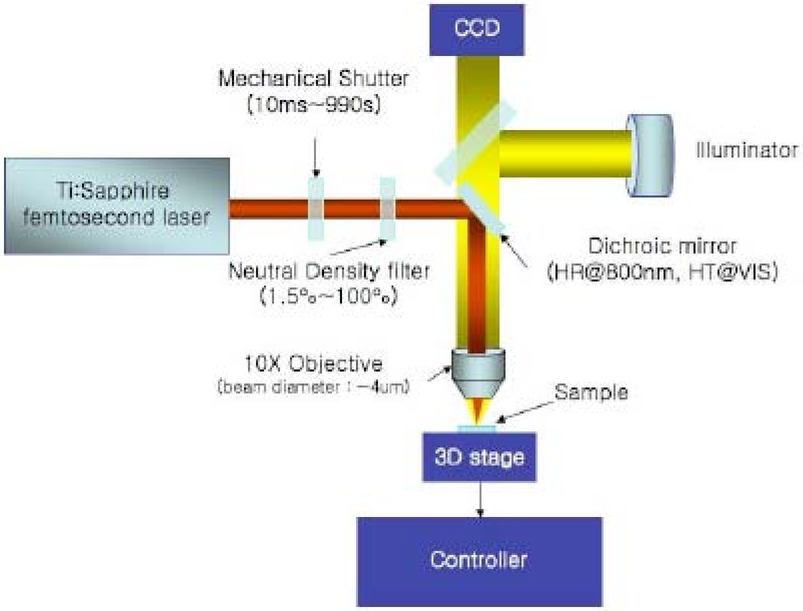

Figure 3.17 Schematic diagram of a laser direct writing system

Figure 3.18(a) and (b) shows fully equipped laser direct writing setups for LS I and LS II respectively. The beam (pulse) profiles of both laser systems were characterized using a Grenouille (Model 8-20, Swamp optics), which is shown in Figure 3.18(b). The pulse widths were measured to be ~60 fs and ~110 fs respectively. An optical parametric oscillator (OPO) was attached to LS II to generate tunable wavelengths $\lambda > 1$ μm via parametric conversion. The variable wavelength range of the OPO system is about from 1.2 to 2.6 μm.

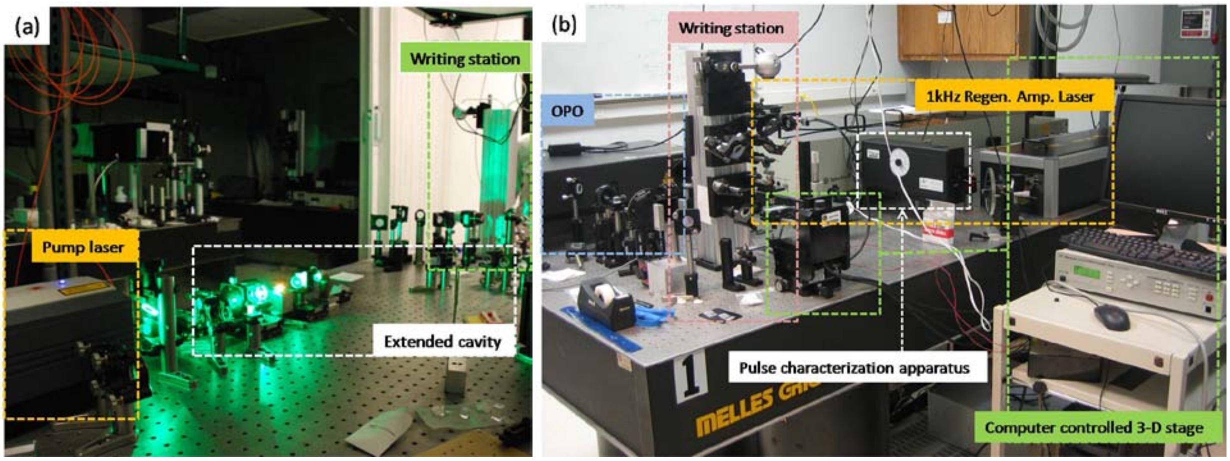

Figure 3.18 (a) 26 MHz extended cabity Ti:sapphire oscillator (LS I) (b) 1 kHz regenerative amplified Ti:Sapphire laser system (LS II) with an optical parametric oscillator (OPO)

Figure 3.19 shows a laser direct writing station using a Yb doped fiber laser system which is referred to LS III above. The pulse width of the system was characterized by a custom built auto-correlator, which is shown in Figure 3.19(b). The auto-correlation trace at 1 MHz repetition rate is shown in Figure 3.19(c).

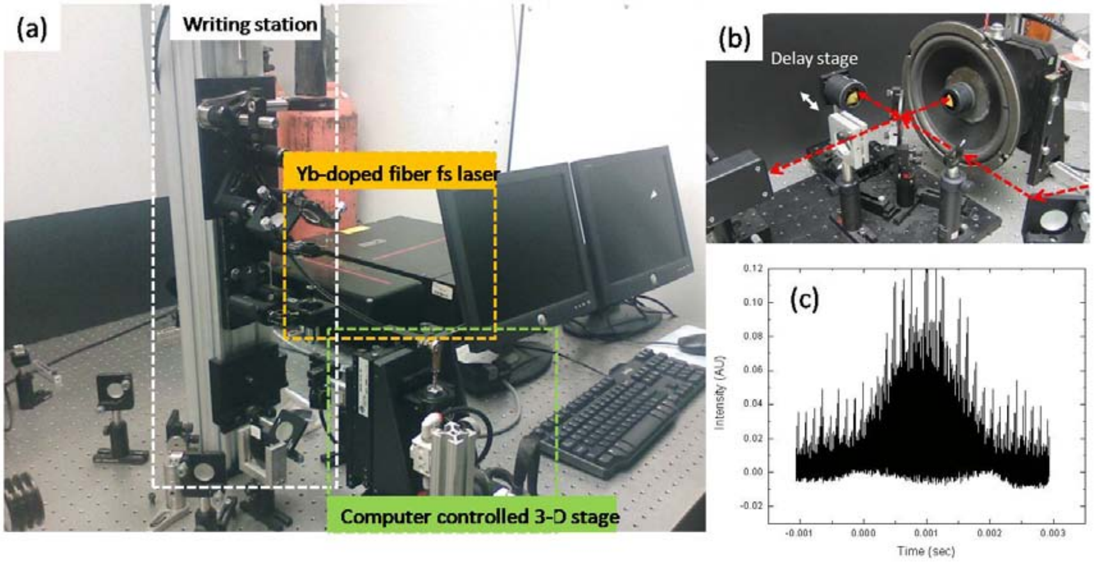

Figure 3.19 Laser direct writing system with (a) Yb-doped fiber femtosecond laser (LS III) (b) a custom-built auto-correlator (c) auto-correlation at 1 MHz (<510 fs)

Various types of objective lenses are used for this work as shown in Figure **3.20**. Low NA refractive lenses (NA=0.1 ~ 0.4) were used for applications requiring long working distance and deep modification depth while oil immersion lenses (NA=1.25) were used for high resolution sub micron structuring. A Schwarzschild reflective objective (NA=0.5) offered small focused beam size with long working distance (~ 10mm) which was useful for longitudinal writing in a thick sample.

Figure 3.20 **Refractive and reflective type objective lenses with various NA**

CHAPTER 4 : CHOICE OF MATERIALS AND THEIR CHARACTERIZATION OF PHOTO-RESPONSE

This chapter discusses the potentials of various optical materials used in photonic device fabrication, various methods and techniques used to observe the physical and chemical properties of laser-written structures, and the photo-responses of materials under femtosecond laser irradiation.

4.1 Optical materials and their potential in photonic device fabrication

The first step to successful femtosecond material processing is to choose the right material for the desired application guided by a deep understanding of material science. The second step is to determine proper optical means for delivering light to the material including the laser wavelength, pulse width, and pulse energy maximizing the photo-response of the material. A variety of optical materials including (non) oxide glasses and photosensitive glasses were chosen to explore the feasibility for a suitable platform of buried volumetric optical structures written by a femtosecond laser. The candidate materials for photonic devices should possess the following attributes:

- High transmittance in the NIR for 3-D direct writing
- Low loss in the desired wavelength range
- Stability (chemically stable and robust to the air / moisture environment)
- Low thermal mechanical degradation with irradiated structure

Fused silica, borosilicate, and tellurite glasses have been chosen as oxide glass families of interest and $As_{0.42-x-y}Ge_xSb_yS_{0.58}$ glass as non oxide glass family for the photosensitivity in NIR range as newly developed for high nonlinear optical coefficient and superb MIR transparency. Novel metal doped SiO_2 thin films, silver containing tellurite, and zinc phosphate glass were also investigated for the space selective photo-precipitation of metal nanoparticles. The samples, except for commercial fused silica and borosilicate glass (EAGLE2000, PGO), were provided from our collaboration groups at Clemson University and the University of Bordeaux I.

4.1.1 Oxide glasses

Oxide glasses have been widely used in the history of optics due to their superior optical properties such as high transparency in the range from NUV to NIR as well as their robust thermal, mechanical, and chemical stability. Furthermore, the explosive development of fiber optic communication resulting from these glasses has brought much attention to oxide glasses. In this research, fused silica and borosilicate glasses are discussed as conventional and commercially available glasses and tellurite glass as an advanced optical material for novel photonics application.

4.1.1.1 Fused silica / borosilicate

Fused silica is a preferred optical glass for the investigation of laser-matter interaction for its simplest molecular structure to analyze underlying physical and chemical mechanisms by femtosecond laser irradiation. Borosilicate glass is also a widely used commercially available oxide glass because of its low thermal expansion coefficient. Many investigations using these glasses have been demonstrated for FLDW such as passive and active waveguides [11, 68, 69], Bragg gratings, and Fresnel zone plates. Recently, the huge interest in the micro-fluidic channels fabrication has been rising towards the fabrication of lab-on-a-chip and disposable sensors [70, 71]. A great concern for many researchers has been fabricating reliable photonic structures, which consist of micro-fluidic channels and waveguides, using FLDW. The refractive index and thermal properties are given in Table 4.1.

Table 4.1 Refractive index and thermal properties of fused silica and borosilicate [72]

	Fused silica[2]	Borosilicate (EAGLE 2000)[3]
Refractive index	1.460 (1014.0nm)	n_D = 1,5068 (589,3nm)
Density (g/cm^3)	2.202 g/cm^3 (20°C)	2,37 g/cm^3 (20°C)
Thermal expansion coefficient		
(0-300°C)	5.5 x 10^{-7}/ °C	31.8 x 10^{-7}/ °C
(25-670°C)		36.1 x 10^{-7}/ °C

4.1.1.2 Tellurite

Tellurite glasses exhibit high transparency in MIR, good thermal-mechanical stability, and laser damage resistance. This glass family is also considered as good optical host materials for rare-earth doping due to low phonon energy. Furthermore, these glasses are promising for high Raman gain platform as they possess high linear and nonlinear optical refractive indices compared to other oxide glass such as fused silica or phosphate glass. As a consequence, this tellurite glass family has been investigated for Raman gain amplifier [73, 74], SHG [75-79] and

---

[2] From ref[72]

[3] From http://www.pgo-online.com/intl/katalog/eagle2000.html

nanofabrication[80]. In this dissertation, a tellurite glass with a composition of $70TeO_2$-$10Bi_2O_3$-20ZnO is investigated as a base glass matrix and silver doped glasses from 2.5% to 7.5% Ag are studied as well. This research explores the means by which one can locally precipitate silver nanoparticles using femtosecond laser irradiation so that the glass can be a platform towards nonlinear optical applications such as SHG. The details of the composition are shown in Table 4.2. This investigation aims to provide a summary of photo-induced responses of the newly processed tellurite glass series subjected to the femtosecond laser irradiation.

Table 4.2 Compositional difference of Zn-Bi-tellurite with/without silver doping

Doping	Composition
Undoped	$70TeO_2$-$10Bi_2O_3$-20ZnO
Silver doped	2.5%Ag - 97.5%($70TeO_2$-$10Bi_2O_3$-20ZnO) 5%Ag - 95%($70TeO_2$-$10Bi_2O_3$-20ZnO) 7.5%Ag - 92.5%($70TeO_2$-$10Bi_2O_3$-20ZnO)

The absorption spectra near the femtosecond laser are shown in Figure 4.1.

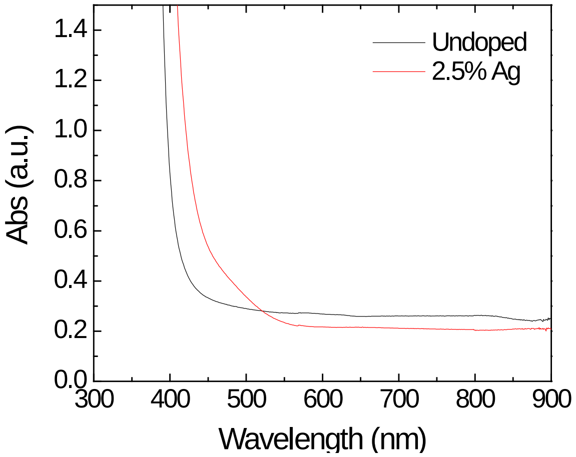

Figure 4.1 Absorption spectra of tellurite family (($70TeO_2$-$10Bi_2O_3$-20ZnO (undoped), 2.5%Ag - 97.5%($70TeO_2$-$10Bi_2O_3$-20ZnO)

The absorption spectrum of 2.5% shows decrease of transparency in the range from 450 nm to 550 nm which may infer the insufficient quality of the glass due to the scattering. An optical microscopic image of the sample confirmed that the glass has defects explaining the absorption band.

4.1.2 Photosensitive glasses

The term “photosensitive” is used here in the sense of a material with narrow bandgap with respect to the wide bandgap exhibited by materials such as fused silica, which leads to low ablation threshold that is two orders of magnitudes lower than oxide glass in NIR range.

Fused silica has a bandgap of 8.9 eV which requires a multiphoton (~6) process for 800 nm femtosecond laser irradiation. This means that either a single photon in the deep UV regime or multiple photons in ultrahigh intensity regimes (which enables multiphoton absorption) is required to excite electrons from the ground state. Photosensitive glasses have, as their name indicates, much lower band-gaps resulting in a lower damage threshold at NIR femtosecond irradiation.

Chalcogenide glasses are amorphous semiconductors containing Chalcogen (Group VI: S, Sb, and Te) species which are responsible for the high nonlinearity in this glass family as well as high IR transparency and photosensitivity. The giant photo-expansion and photo-darkening by near bandgap laser irradiation in ChG has been well known since a few decades ago, and studied by many investigations [81]. Series of research on femtosecond laser irradiation in these glasses have been intensively conducted by Laser Plasma Laboratory group as well [82-87]. In this dissertation, home-made ChGs have been investigated in bulk form to study their laser-induced photo-response when subjected to the femtosecond laser irradiation. $As_{0.42-x-y}Ge_xSb_yS_{0.58}$ glasses have been also investigated, with glasses provided by the Clemson University team. The preparation of the glass sample is described in [84, 88]. Table 4.3 and Figure 4.2 show their chemical and optical properties. It is noted that as heavy Sb content is increased, the material density is increased and the bandgap of the system is red-shifted. The refractive index is also increased whereas in the case of increasing Ge content, the refractive index decreased from that of $As_{42}S_{58}$.

Table 4.3 material properties of the system

Sample	EDS (±5%)	Density (g/cm^3 ±0.02)	Tg (°C ±5)	Cutoff wavelength (nm) @ 10cm^{-1}
$As_{42}S_{58}$	$As_{42}S_{58}$	3.20	210	580
$As_{36}Ge_6S_{58}$	$As_{34}Ge_8S_{59}$	3.15	220	580
$As_{36}Sb_6S_{58}$	$As_{37}Sb_6S_{57}$	3.40	208	625

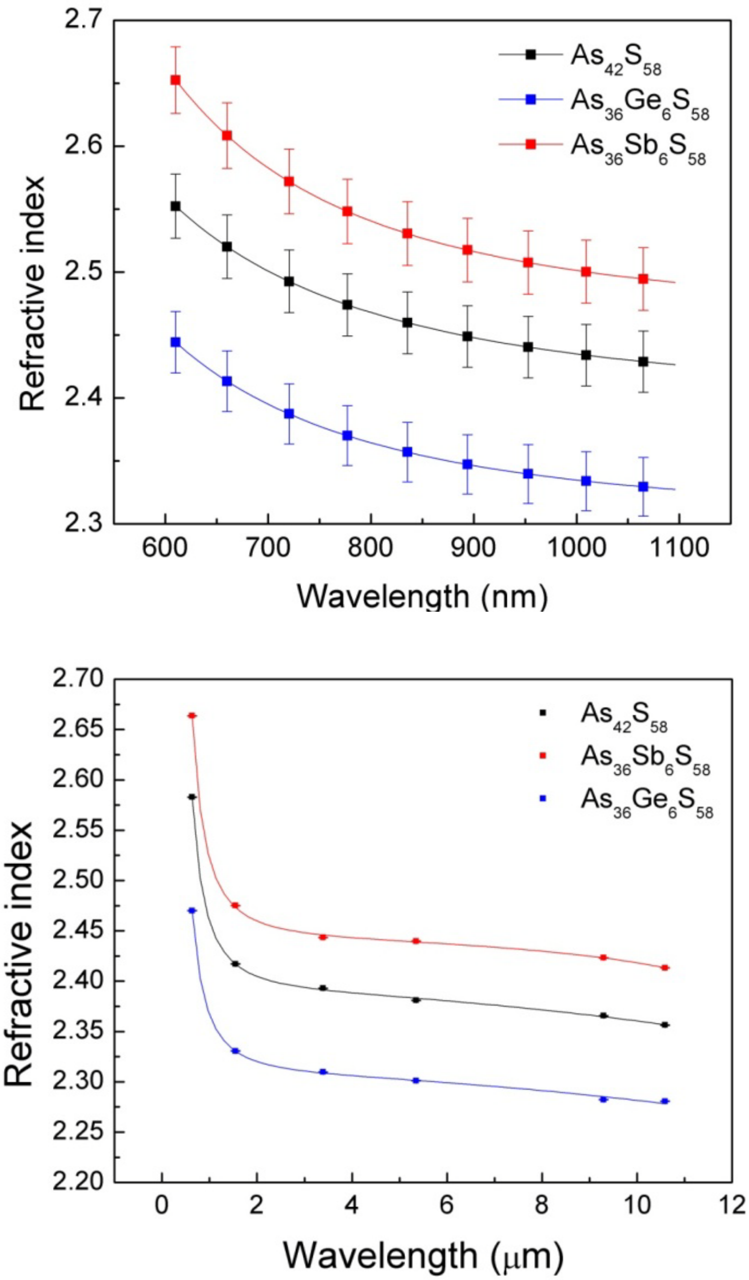

Figure 4.2 Refractive index of given materials (top) in NIR region (bottom) in MIR region. From [84][4]

---

[4] Provided by N. Carlie at Clemson University

4.1.3 Noble metal ion containing glasses

Nobel metal nanoparticles embedded within glass provide a great opportunity to tune optical properties of glass matrix by changing their metallic compositions, size, and concentration. They exhibit large third-order nonlinear susceptibility and ultrafast nonlinear response which promotes them to be promising materials for an ultrafast all-optical switch in the THz region [89-91]. Moreover, these glasses would be suitable for the platforms of nano-structured surface plasmonics prepared by laser irradiation. Commonly, ion exchange and ion implantation are used to provide a means of space-selective precipitation of nanoparticles in a substrate [92-94]. However, after further treatment, both the composition of the glass matrix and the nanoparticles-precipitated area are restricted in the ion-exchange method. Laser direct writing can offer versatility of space selective formation/dissolution of nanoparticles without any restriction and damage.

4.1.3.1 Ag/Cu/Au doped silica glass prepared by sol-gel method

Three metal species (Ag, Au, Cu) have been used as dopant ions in silica glass films prepared by sol-gel method to investigate photo-induced metallic nanoparticles formation/dissolution using UV and NIR light sources including a CW UV lamp, a 3rd harmonic Nd:YAG laser, and a 1 kHz Ti:Sapphire laser. The metallic precursors were dissolved in a solvent to be mixed with a tetraethylorthosilicate (TEOS, $C_8H_{20}O_3Si$, Sigma –Aldrich), using ethanol as the solvent. The final solution was sealed and stirred at room temperature for 24 h. The films were spin-coated on microscope slides with the thickness less than 1 µm and annealed for 15 h at 150 °C. The absorption spectra before and after the irradiation will be presented in the next section.

4.1.3.2 Silver containing zinc phosphate glass

The glass composition of the matrix is $40P_2O_5$-xAg_2O-(5-x) Ga_2O_3-55ZnO (molar percent) [95, 96]. The glass was produced using a melt-quench method. $(NH_4)_2HPO_4$, ZnO, $AgNO_3$, and Ga_2O_3 were the raw materials. Gallium oxide was introduced to increase the glass stability. The raw materials were placed in platinum crucible and heated up to 1000 ºC with the heating rate of 1 ºC/min. Then the glass was annealed at 320 ºC (55 ºC below T_g) for 3 hours. The concentrations of silver oxide (Ag_2O) for this research were 1% and 4% (mol %). Figure 4.3 shows the absorption and emission spectra of the glass [96]. The emission located at 380 nm, corresponding to the absorption at 265nm, is attributed to isolated Ag^+ silver ions.

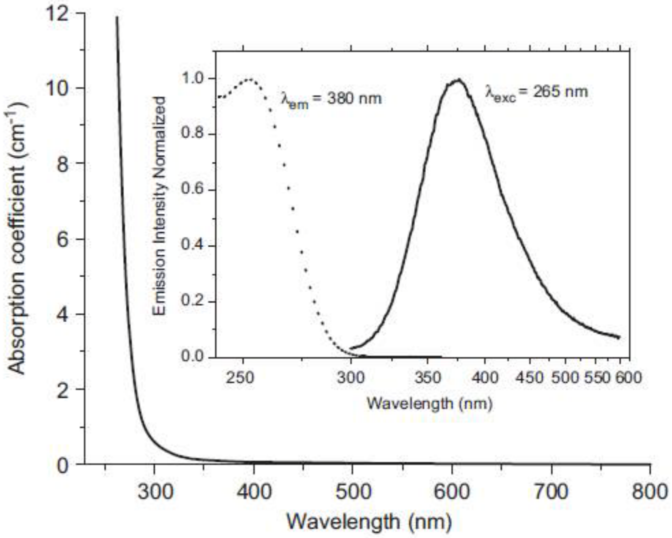

Figure 4.3 Absorption and emission spectra of 1 % silver containing zinc-phosphate glass. From [92]

4.2 Characterization of laser-written structures

4.2.1 Physical domain

4.2.1.1 Differential interference contrast (DIC) optical microscopy

Optical microscopy is the most commonly used technique to observe the physical appearance of surface features. Although the resolution of the technique is governed by the optical diffraction limit, various image quality enhancement techniques generally enable micron to submicron resolution. Specifically, a DIC optical microscope exploiting a polarizer and an analyzer provides the ability to increase the contrast of the region possessing slightly different refractive indices. This configuration has provided powerful imaging means for transparent specimen such as biological cells, tissues, and glasses. Therefore, it is suitable not only for surface modifications, but also for the observation of femtosecond laser-written embedded structures in a transparent substrate such as a photo-induced refractive index change exhibiting a similar refractive index with their transparent surroundings.

4.2.1.2 White light surface profiler

White light interferometeric surface profilometry is a non-contact method to characterize the surface of the specimen. The Zygo NewView 6300 (Zygo Coporation, http://www.zygo.com/) was used to measure and characterize the surface expansion or contraction induced by laser irradiation with nanometer resolution. The Zygo profiler is based on the Fizeau interferometry: the light from a white light LED is split into two arms. One is reflected from the surface of the sample and then interferes with the other arm reflected from the reference surface. The resulting interferogram is analyzed to be converted as the surface profile. This profiler offers high vertical resolution (< 0.1 nm) since it is based on white light interferometry and the coherence length of the light source is very short. The lateral resolution is from 0.36 to 9.5 µm, which is objective dependent. Figure 4.4 shows an example of the surface profile measurement. Femtosecond laser irradiated bulk $As_{36}Ge_6S_{58}$ exhibits photo-expansion on the order of up to a few hundred nanometers. The surface profile reveals that the expanion is laser dose dependent. The detail of the analysis is presented in section 4.3.2.

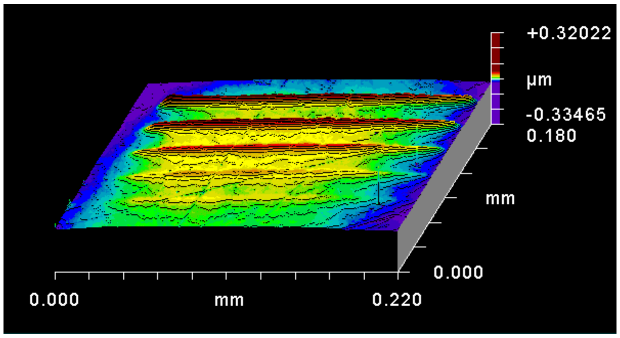

Figure 4.4 Photoexpansion of bulk $As_{36}Ge_6S_{58}$ glass measured by zygo white light surface profiler

4.2.1.3 Optical coherence microscopy

Optical coherence microscopy (OCM) provides noninvasive highly resolved 3-dimensional images of biological specimens [97, 98]. To date, very few studies on imaging femtosecond laser directly written samples have been carried out [13]. As OCM implementations have been constructed with Ti:Sapphire-based femtosecond lasers to take an advantage of its broadband spectrum, the materials of interest for femtosecond laser machining such as oxide glass and optical polymers possess the same transparent windows as the OCM probe source. This means that it is possible to perform low noise measurements relying on low intrinsic extinction ratios. Because this technique does not require any sample preparation prior to the measurement, it may be utilized as a fast diagnostic means of the laser direct writing to evaluate the real time quality of the processed structure in the specimen.

The OCM system used in this research provides ~2.5 µm axial resolution in air and ~1.72 µm in fused silica corresponding to a 120 nm bandwidth. The lateral resolution is dependent on the objective lens. In this work, 0.12 NA objective lens providing 4.4 µm lateral resolution and 35 µm depth of focus in fused silica was used. Figure 4.5 shows an embedded laser-induced refractive index change and void formation written in fused silica substrate. The sample was produced to examine the detectability of the OCM facility with the S/N ratio of ~ 97 dB. Figure 4.6 is the OCM images of the side view and top views of the void formation created by 8.3 µJ. The 3-D structures are clearly seen without any shadow effect. However, the refractive index change is not detected, probably due to the low index change of the fused silica, implying the induced index is less than 10^{-5} corresponding to the sensitivity of 97dB [99].

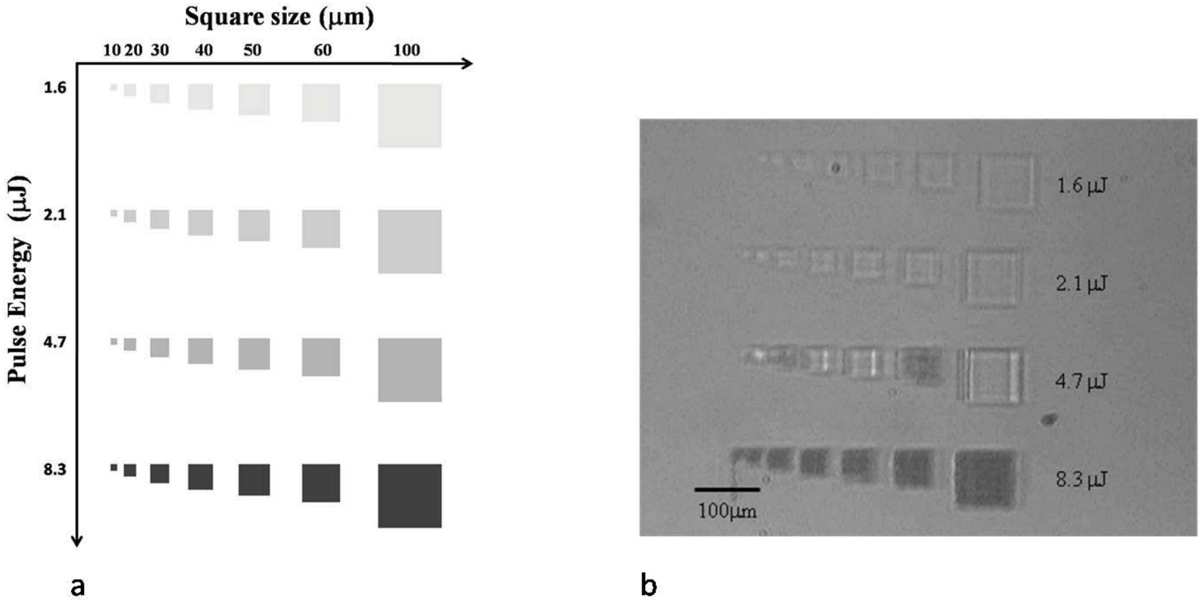

Figure 4.5 (a) Map of the buried structure (b) optical image of the laser-written structure in fused silica

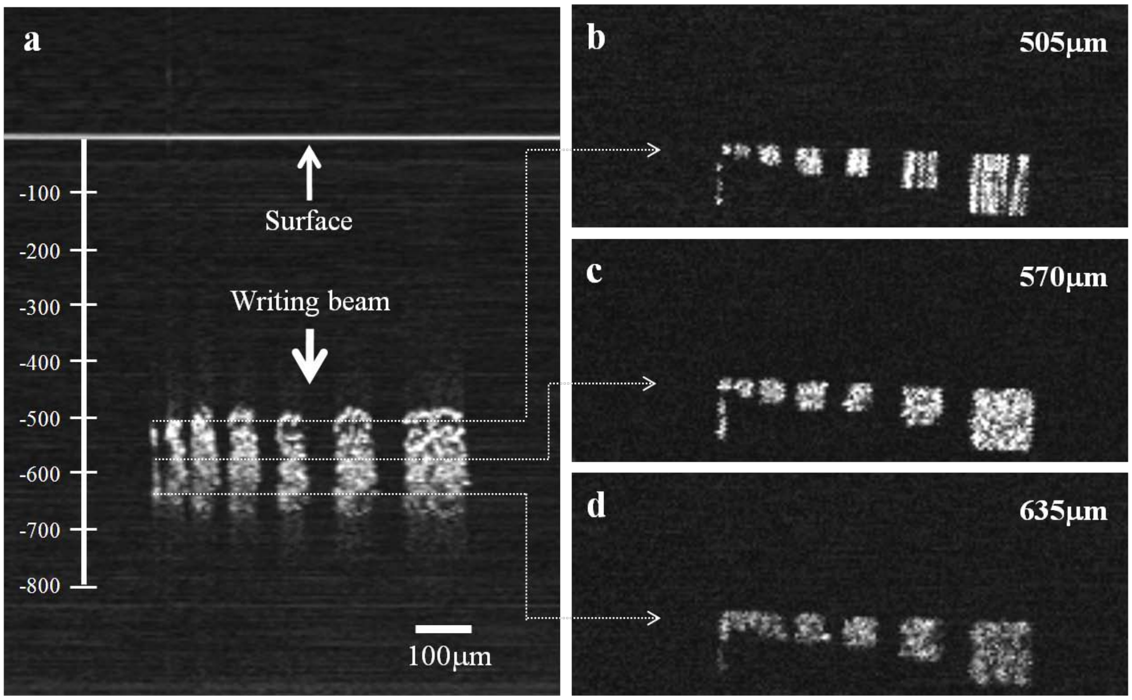

Figure 4.6 OCM images of buried 3-D structure (a) side view (b-d) top views at different depths (Images were provided by the ODA lab, led by Dr. Rolland.)

To increase the photo-induced refractive index change and improve detectivity of refractive index change, a bolosilicate glass was used as a substrate. Figure 4.7 and Figure 4.8 are the images of a buried FZP taken by a DIC optical microscope and OCM respectively. The 172 images of side view in x-z plane were acquired by scanning in x-direction. The top view image was then reconstructed from re-slicing 172 images. This image clearly proved that OCM can detect refractive index changed structrures. Furthermore, the modified length can be measured without any sample preparation such as grinding and polishing.

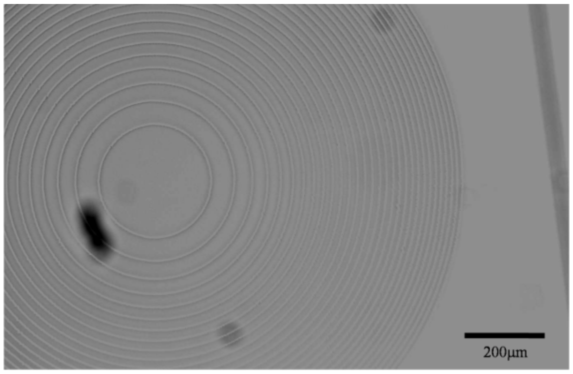

Figure 4.7 An embedded FZP written in borosilicate

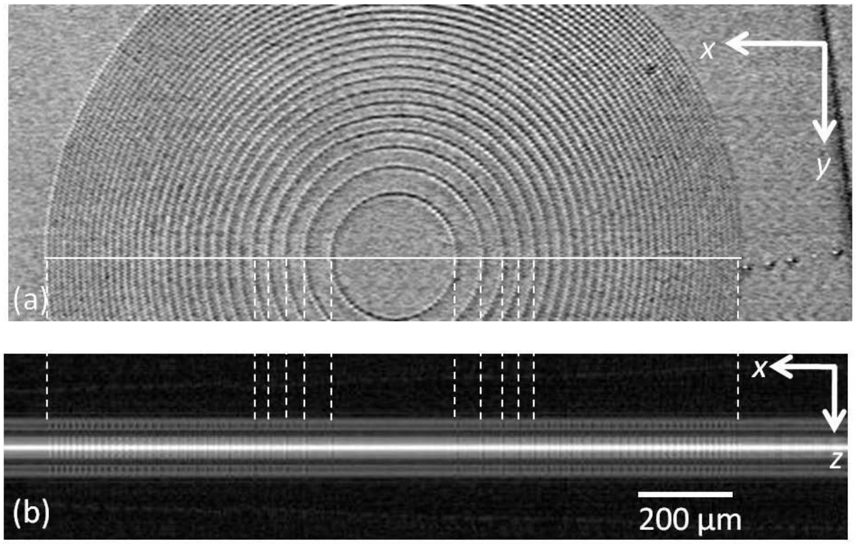

Figure 4.8 OCM images of an embedded FZP written in borosilicate (a) top view (b) side view (a mirror image is also shown in the side view which can be removed by a appropriate data analysis) (Images were provided by the ODA lab, led by Dr. Rolland.)

4.2.1.4 Laser-induced refractive index change

Refractive index change of laser-written structure can be measured with several methods such as refracted-near field profilometry [9, 47], microellipsometer [7], cylindrical waveguide mode solving routine (Rsoft BeamPROP) [46, 100] OCT [13], guided mode analysis of a written waveguide [13], white light interferometry [82, 86], Swanepoel analysis [86, 101] and grating method [14, 16]. These methods are complementary to each other in terms of accuracy and ease of measurement. Grating method is a measurement of diffractive power of input beam via a laser-induced grating. This method does not provide either a precise number or sign of the index change, but estimation of overall change due to the formation of a grating. However, it is often used for its easy scheme as well as simple implementation. Figure 4.9 depicts the concept of the measurement. The refractive index change is deduced from the measured diffraction efficiency which is the ratio of the 1st diffracted power to the input power.

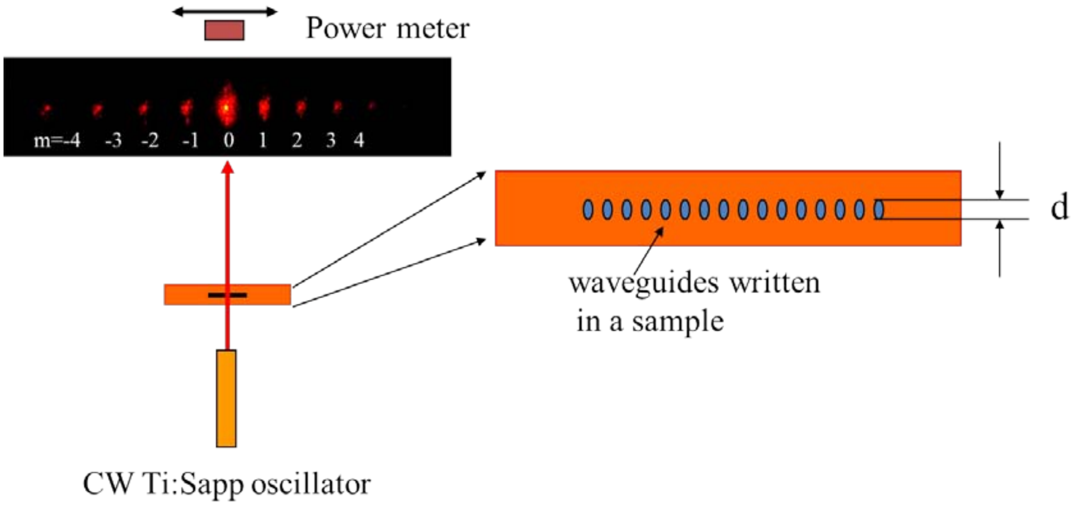

Figure 4.9 A schematic illustration of a measurement of the refractive index change using a grating method.

The diffraction efficiency of the amplitude / phase grating can be represented by the Eq. 4.1[102]

$$\eta_m = (\frac{\pi \Delta n d}{\lambda})^2 + (\frac{\Delta K d}{4})^2, \tag{4.1}$$

where η is a diffraction efficiency of the 1st order, Δn and ΔK are the refractive index and absorption coefficient of the glass, and d is the depth of the grating, and λ is the wavelength of input beam. In this work, most transparent phase gratings utilized for the estimation of laser-induced gratings. In phase grating, ΔK is negligible, thus Eq. (4.3) involving Bessel function is often used alternatively [14].

$$\eta_m = J_m^2(\delta) = J_m^2(\frac{2\pi L \Delta n}{\lambda \cos\theta}). \tag{4.2}$$

4.2.2 Chemical domain

4.2.2.1 Raman spectroscopy

Raman spectroscopy is a means to investigate a transition which is forbidden by one-photon excitation. It is useful to investigate the change of molecular structure by stimulation, specifically in this study, stimulation by intense laser irradiation. Figure 4.10 shows a depiction of the Raman scattering. The involved energy levels are indicated as g, n and n’ which are a ground level and upper states respectively. Stokes Raman scattering is a transition from g to n via intermediate state related to n’ ($\omega > \omega_s$) and Anti-Stokes scattering is vice versa ($\omega < \omega_s$) where ω and ω_s represents excitation photon and Raman scattering respectively.

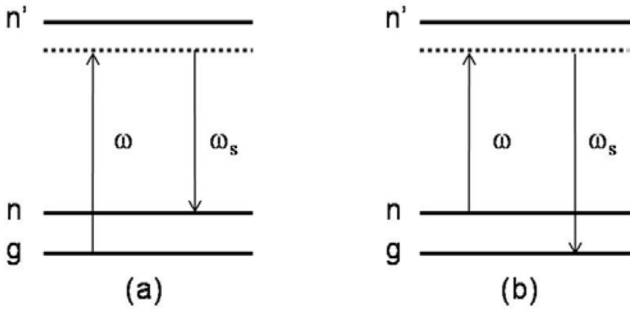

Figure 4.10 E level diagram of Raman scattering (a) Stokes (b) Anti-Stokes

In material research, Raman spectroscopy can be used to identify the presence of the target bonds in the material by examining the existence of their vibration modes as a spectroscopic “tag”. In this dissertation, photo-expansion of chalcogenide glasses was investigated using a micro Raman spectroscope to understand the underlying chemical mechanism of the bond change responsible for the photo-expansion induced by femtosecond laser irradiation.

Figure 4.11 shows a Raman spectrometer coupled from two laser sources; a 515 nm frequency doubled Yb-YAG laser and a tunable Ti:Sapphire oscillator tuned by VBG coupler in NIR range (750 ~ 850 nm). Therefore, micro Raman with broad wavelength range enables the investigations of the photo-structural modification produced in various glasses such as oxide glasses and photosensitive glasses.

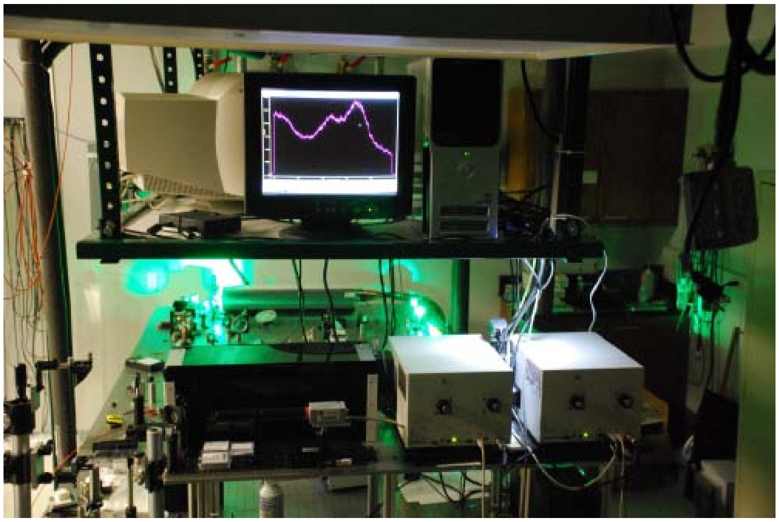

Figure 4.11 VBG coupled multi-pump Raman spectroscope

4.2.2.2 UV-VIS-IR spectrophotometry

The UV-VIS-IR spectrophotometer is an apparatus consisting of a broadband light source, a monochrometer, a photo detector, beam delivery optics, and sample holder. It is used to measure the fraction of light that passes through a sample. The light is then detected through a monochrometer to select only one wavelength from the continuum to measure the portion of the wavelength. The monochrometer is swept throughout the desired wavelength range. Thus, the linear optical properties such as transmission and absorption of the sample are measured. A CARY 500 (Varian Inc), which offers a detection range from 170 nm to 3300 nm, was used for this investigation. It was intensively used for extinction spectroscopy experiment (attenuation by absorption and scattering) to confirm the formation/dissolution of metallic nanoparticles in Ag/Au/Cu doped SiO_2 thin film by UV laser or NIR femtosecond laser irradiation. It is well known that noble metal nanoparticles such as Ag and Au induce additional absorption bands in the host material at the visible range due to surface plasmon resonance, which can be explained by Mie theory [103]. The location of the absorption band depends on their size, shape, and density. Therefore, not only the existence of metallic nanoparticles, but also their physical properties can be deduced from the extinction measurement. The example of the measurement is shown in 4.3.3.

4.2.2.3 Fluorescence (confocal) microscopy

Photoluminescence is an emission from a semi-stable level to the ground level. This process occurs when an electron is excited from the ground state to higher energy level by absorption of photon via external excitation. The electron spontaneously decays to the next lower level by energy loss until it reaches the semi-stable level. The electron emits a photon corresponding to the difference of energy from upper level to ground level. If the radiation is spin-allowed transition, the process is called “fluorescence” whose lifetime is typically 0.1 ~10 ns[104]. Figure 4.12 shows a schematic diagram of fluorescence process. As is seen, the energy of the emitted photon cannot exceed the energy of excitation photon due to energy conservation. In general, fluorescence provides the information on the intrinsic electronic configuration in the material which can be used as a “fingerprint” of the presence of the material. Fluorescence (confocal) microscopy is widely used for biological imaging and material science for the investigation of the fluorophore tagged specimen or intrinsic fluorescent materials.

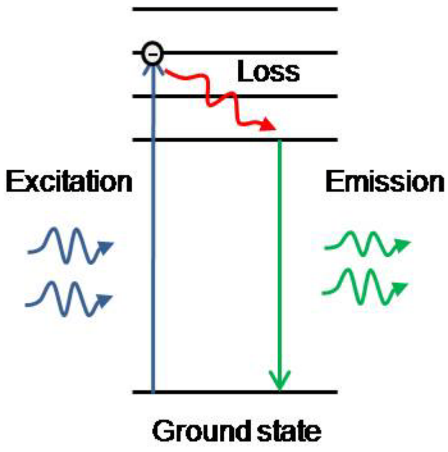

Figure 4.12 Diagram of the energy levels involved in fluorescence

In this dissertation, fluorescence microscopy was also used to investigate the properties of photo-reduced silver clusters since their photoluminescence properties are well known [105-107]. One-photon or two-photon fluorescence spectroscopy using femtosecond laser irradiated silver containing zinc phosphate glass was investigated to confirm the existence of photo-reduced silver clusters in the glass after irradiation. The details of the experiment to confirm the precipitation of silver nanoparticles in zinc phosphate glass by their photoluminescence properties will be present in section 4.3.3.

4.3 Photo-response of materials under femtosecond laser irradiation

4.3.1 Ablation threshold measurements

Ablation is the process describing destructive, violent removal of the material from the surface by intense laser irradiation. "Optical breakdown" is often misused as an alternative term in similar phenomena by laser pulses, but it is a more general process regarding the breaking bonds between molecules, and not necessarily either material removal or confined on the surface.

However, ablation and optical breakdown thresholds of a material of interest are similar in the order of magnitude. Thus, bond strength of the material of interest is often estimated by measuring ablation threshold because phenomena on the surface are easier to observe and analyze than the events in the bulk. Figure 4.13 shows a typical ablation threshold map whose one axis represents an intensity of the irradiation and the other axis is a function of time (or number of pulses). Black dots are a physical removal of material from the surface of the sample.

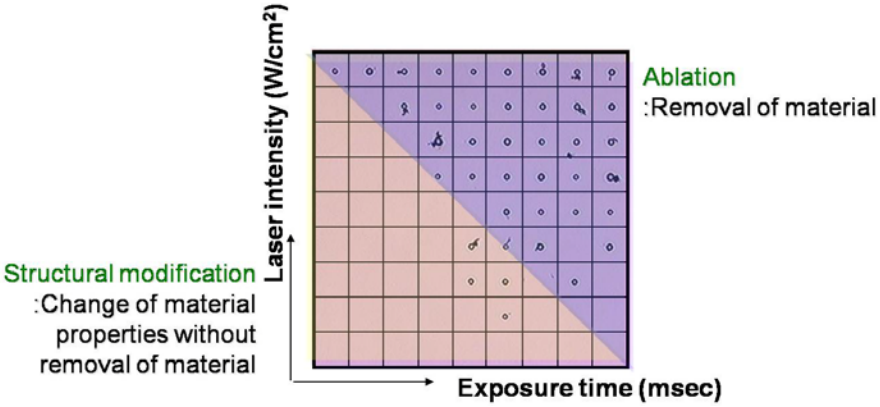

Figure 4.13 Optical microscopic image of an ablation threshold map (PMMA)

Table 4.4 shows ablation thresholds of a variety of optical materials including glasses and PFCB polymer. As discussed, the ablation threshold of materials can be estimated through their absorption properties. As is shown in the table, borosilicate glass exhibits the highest ablation threshold while chalcogenide glass family has the lowest value.

Table 4.4 Ablation threshold of various glasses and polymers at different repetition rates[5]

Sample		Irradiance (GW/cm^2)		
		1 kHz (800 nm)	9.44 MHz (1030 nm)	26 MHz (800 nm)
Microscope slide glass (borosilicate)		55.2E+3		
Tellurite	TeO_2-Bi_2O_3-ZnO (TeBiZn)	12.9E+3	3.0E+3	
	TeO_2-$Na_2B_4O_7$ (Te9)	930.0		
Borophosphate $(1-\mathbf{x})(0.514Ca(PO_3)_2-0.436NaPO_3-0.05Na2B_4O_7) - \mathbf{x}\ Nb_2O_5$	X=0.025	8.4E+3		
	X=0.30	3.4E+3		
	X=0.40	3.4E+3		
	X=0.45	2.5E+3		
Chalcogenide	$As_{42}S_{58}$			446.3
	$As_{36}Sb_6S_{58}$			297.6
	$As_{36}Ge_6S_{58}$			485.1
PFCB (polymer)		813.0		419.0[6]

In Figure 4.14, schematic depiction of the ablation threshold of the optical materials tested for this dissertation is illustrated as functions of intensity and repetition rate. It should be noted that, even for the same material composition, higher repetition rates tend to reduce ablation threshold. This issue will be discussed later.

---

[5] Measurement errors are less than ±5%

[6] Measured at different repetition rate of 36 MHz

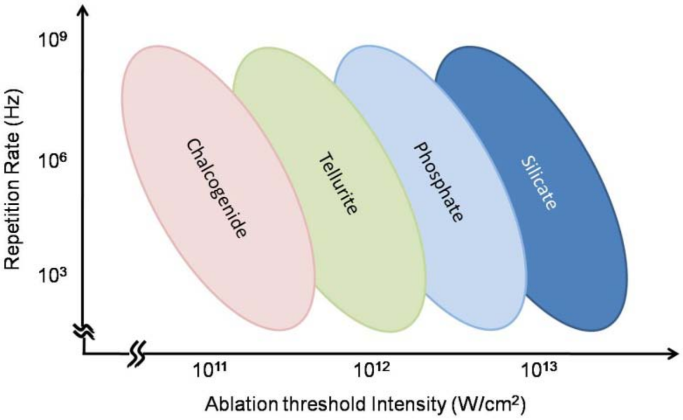

Figure 4.14 Schematic diagram of the ablation threshold ranges of optical material families

It may also be noticed that ablation threshold variance is dependent on the absorption properties in the similar composition with the same base material. For instance, in the borophosphate family, the absorption bandgap shifts to longer wavelength as the amount of Nb_2O_5 increases. The shift leads to a decrease of the ablation threshold, as shown in Figure 4.15. The same trend is also seen in Chalcogenide glass family. In Table 4.3, The bandgap of $As_{42}S_{58}$ and $As_{36}Sb_6S_{58}$ has similar at 580nm while $As_{36}Sb_6S_{58}$ has a red-shifted bandgap at 625nm. As seen in Table 4.4, $As_{36}Sb_6S_{58}$ has the lowest ablation threshold that results from the red shift of the absorption bandgap closed to the laser wavelength of λ = 800 nm.

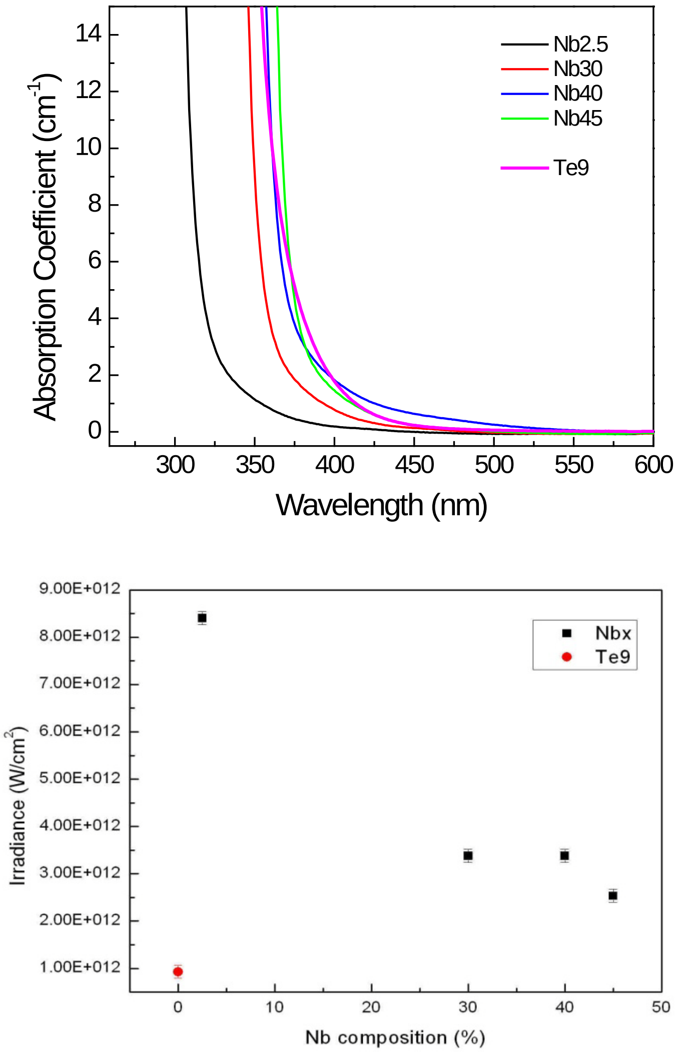

Figure 4.15 Absorption spectra(top) and ablation threshold (bottom) of borophosphate and tellurite (Te9) glass

It should also be noted that, even same material shows different ablation threshold at different repetition rate, as discussed in Chapters 2 and 3. In the case of tellurite glass (TeBiZn), the ablation threshold at 1 kHz is one order of magnitude higher than 9.44 MHz, even though the laser wavelength is slightly different in NIR regime. PFCB polymer shows the same result, but not as drastic as tellurite. This confirms that it is the heat accumulation effect which reduces the onset of material damage. Figure 4.16 shows threshold maps of 10 μm thick PFCB thin film irradiated at different repetition rate, 1 kHz and 36 MHz.

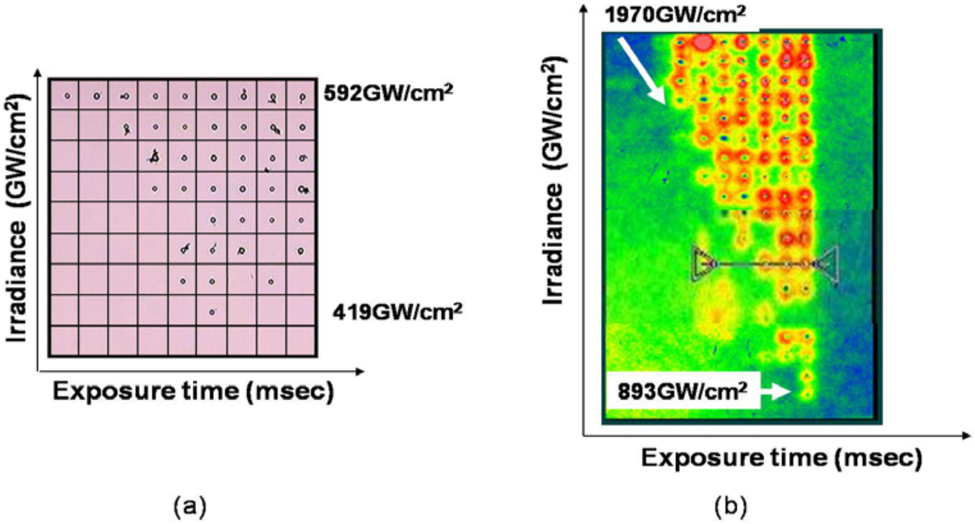

Figure 4.16 Ablation threshold map of PFCB at different repetition regime

(a) 36 MHz (b) 1 kHz

4.3.2 Photoexpansion and related structural modification

Photo-expansion of chalcogenide glass induced by laser irradiation is quite well known feature. Tanaka et al. [81, 108] observed giant photo-expansion of As_2S_3 by HeNe laser irradiation. In this investigation, photo-expansion via femtosecond laser irradiation was systematically investigated as a function of laser dose. Six lines with 200 μm were written on the each bulk ChG glasses ($As_{42}S_{58}$ /$As_{36}Sb_6S_{58}$/ $As_{36}Ge_6S_{58}$) via 26 MHz femtosecond laser pulses centered at ~800nm. A 10X microscope objective with NA=0.25 was used to focus the laser beam into the sample. The laser pulse energy was kept constant, ~90% of the ablation threshold of materials to produce the maximum photo-expansion. In this way, laser dose was controlled only by writing speed and is inversly proportional to the writing speed. Laser dose was changed as a function of writing speed. The writing speed was varied from 5~160 μm/s. Figure 4.17(a) shows the photo-expansion of bulk $As_{36}Ge_6S_{58}$. In the picture, the photo-expansion decreases as writing speed increases due to the reduced laser dose. The trend is clearly seen in other glasses shown in Figure 4.17(b).

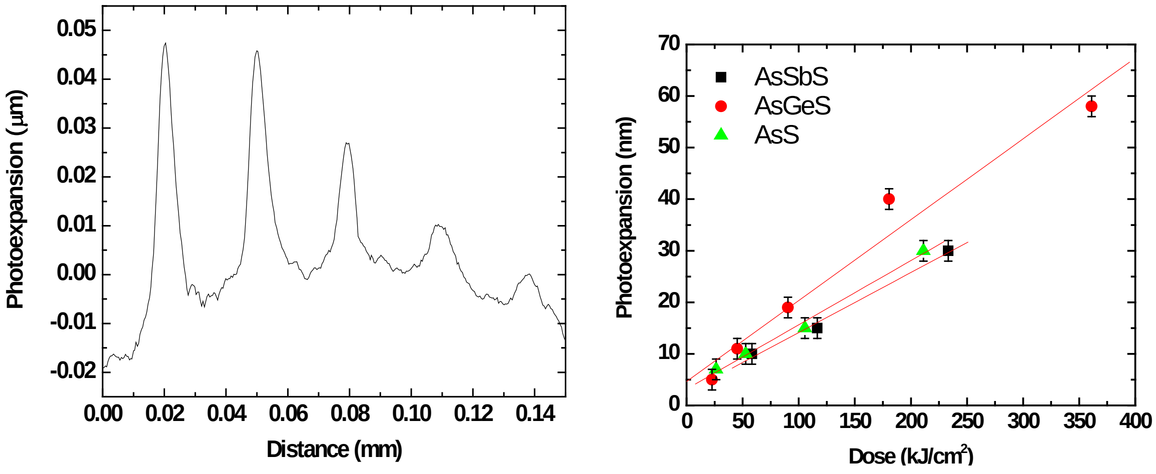

(a) (b)

Figure 4.17 (a) Photoexpansion of bulk $As_{36}Ge_6S_{58}$ glass measured by zygo white light surface profiler (the translation speed was varied from the highest line, 5, 10, 20, 40, 80 and 160 μm/s) (b) Photoexpansion of $As_{42}S_{58}$/ $As_{36}Ge_6S_{52}$/ $As_{36}Sb_6S_{58}$ as a function of laser dose. . From [109]

The photo-expansion by femtosecond laser irradiation was investigated with micro Raman in order to understand the molecular bond changes responsible for the photo-expansion. In Figure 4.18, the Raman spectra of three compositions after laser irradiation are shown. There is no real change in the main band of $As_{42}S_{58}$ after irradiation while $As_{36}Sb_6S_{58}$ and $As_{36}Ge_6S_{58}$ has significant decrease of peak in the main band. However, all three compositions exhibit changes in the regions from 200 to 250 cm^{-1} and 450 to 500cm^{-1}. This is attributed to the creation of As-As and S-S bonds. $As_{36}Ge_6S_{58}$ also shows a broadening of the main band with increasing dose.

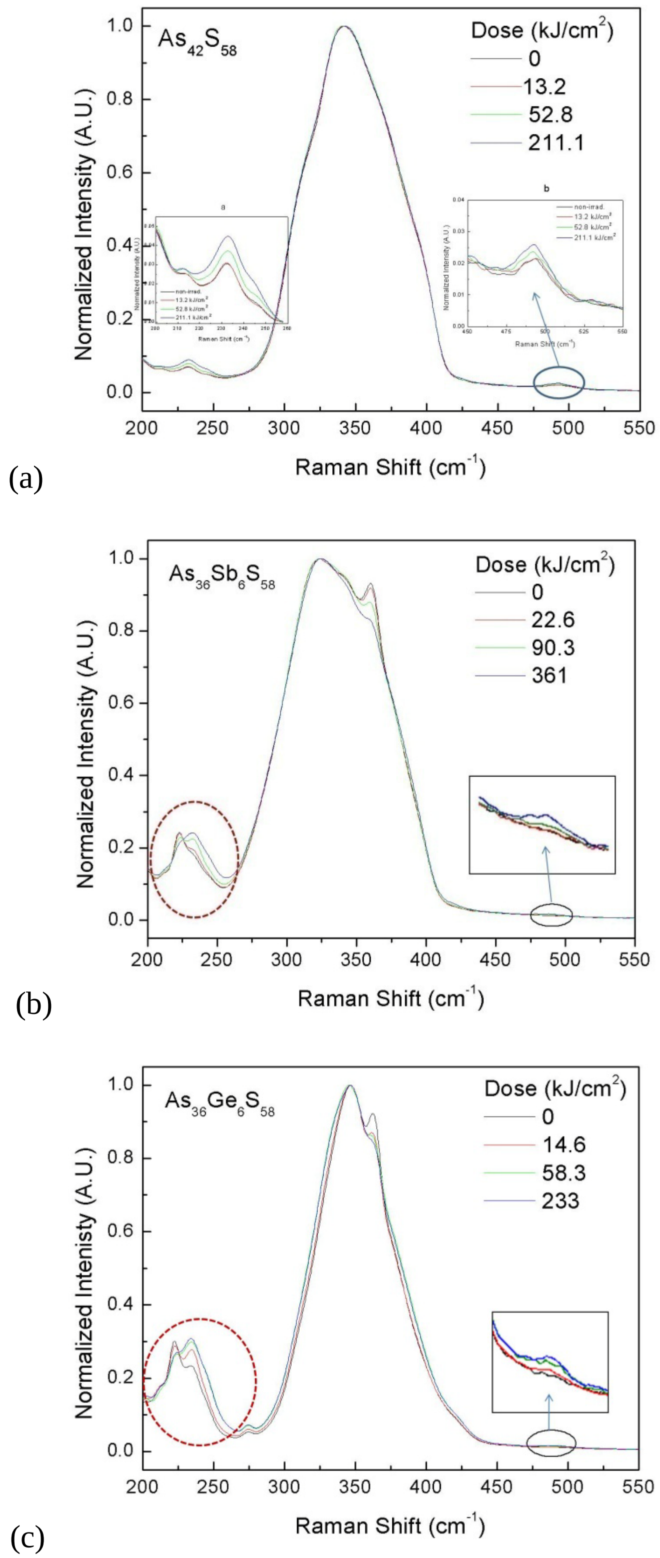

(a)

(b)

(c)

Figure 4.18 Raman spectra of given materials after fs irradiation (a) As$_{42}$S$_{58}$ (b) As$_{36}$Sb$_6$S$_{58}$ (c) As$_{36}$Ge$_6$S$_{58}$

4.3.3 Metallic nanoparticle formation

The conventional method used to form metallic nanoparticles is thermal treatment or via γ-ray or e-beam irradiation for localized formation. The underlying mechanism of the formation of nanoparticles in the metal ion containing glass is well understood [92, 94, 105, 107, 110]. The intense irradiation from these sources forms color centers, which exist as e- and hole trap pairs. Consequently, metallic ions can be then reduced by the free electrons generated during irradiation. Post irradiation annealing helps the reduced atoms to aggregate (by diffusion) and become larger clusters. After annealing, the glass turns colored due to newly generated absorption by the surface plasmon resonance of metallic nanoparticles formed in the glass. Different metal species, particle size, and concentration of metal nanoparticles lead to different absorption properties. This means that one can tune the absorption properties by changing those parameters. Several research groups including Qiu et al. demonstrated that femtosecond laser irradiation can also form metal nanoparticles in the glass [111, 112]. The advantage of this method over the conventional means discussed above is the ability to create 3-D structures consisting of metal nanoparticles which might be useful for fabricating surface plasmonic structures.

UV-VIS-IR spectrophotometers are commonly used for extinction spectroscopy to verify the existence of absorption band resulting from surface Plasmon resonance. By measuring absorption bandwidth and its peak location, the size and concentration of metal nanoparticles can be estimated. Figure 4.19 shows the transmission spectra of laser irradiated metal doped film.

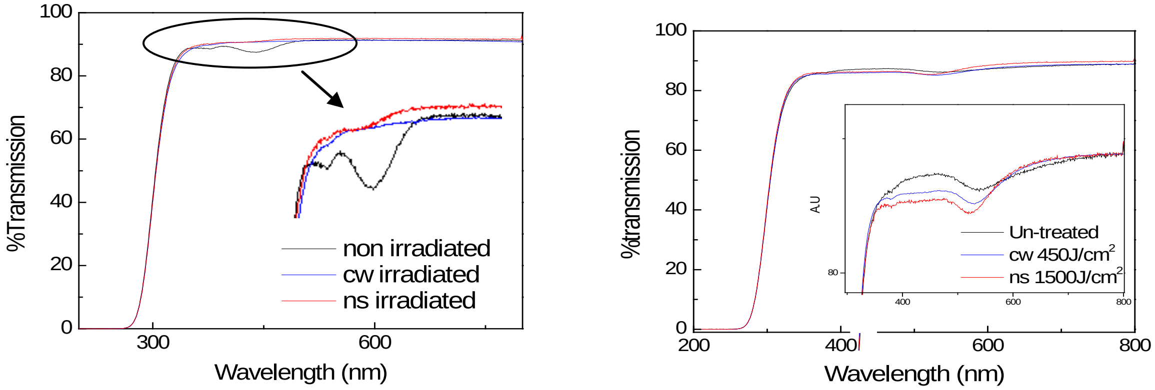

(a) (b)

Figure 4.19 Formation / dissolution of nanoparticles in SiO_2 thin film (a) dissolution of Cu nanoparticles by irradiation of CW/ns light at 355 nm. (b) Formation of Au particles by UV light followed by 30 min heat treatment at 520 °C

In the picture, it is seen that the amplitude of the absorption peak decreased by 355 nm CW/ns irradiation which confirms that UV light source dissolves metal nanoparticles in the glass film. Figure 4.19(a) shows opposite result. Irradiation of UV nanosecond laser or IR femtosecond laser followed by heat treatment for 30 minutes at 520°C changes the location of the absorption peak. It should be noted that the absorption peak resulting from surface plasmon resonance was shifted to the blue region also the bandwidth of the peak was decreased which means the laser irradiation changed the size distribution of the nanoparticles.

Partial reduction of silver and formation of clusters formed of Ag^0 and Ag^+ can be detected by investigation of the luminescence property of the materials. Figure 4.20 shows the photoluminescence of silver ion containing zinc phosphate (P_2O_5-Ag_2O-Ga_2O_3-ZnO) after 1043nm fs laser irradiation. The glass was excited at 405 nm and emitted typical red color near 600nm which proves the existence of silver clusters Ag_m^{x+} (m<10) formed by laser irradiation.

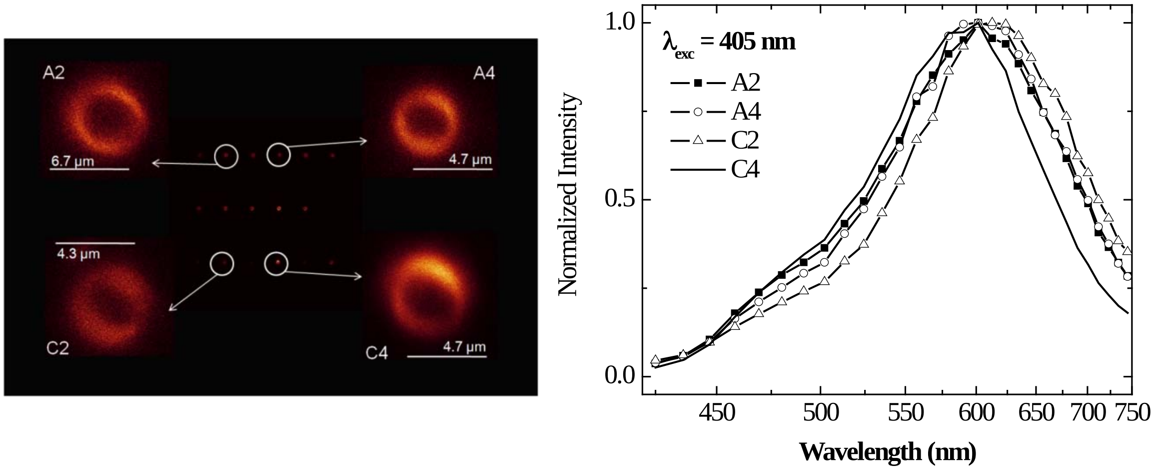

(a) (b)

Figure 4.20 (a) Fluorescence microscopic image of laser-induced silver clusters (b) fluorescence spectra of the emission of silver clusters with the excitation at 405 nm

4.3.4 Refractive index change

The complete mechanism for laser-induced refractive index change of all optical materials is not well understood yet. However, for a few cases, rigorous investigations have clarified the underlying mechanism responsible for laser-induced refractive index change Δn. For instance, laser-induced densification of fused silica, which is a glass with a simple (binary) molecular form, is well understood as to its origin of the laser-induced refractive index change [113]. In this study, femtosecond pulse-induced Δn in bulk ChGs has been systematically studied in the relation of photo-expansion involved with a photo-induced structural change.

The embedded gratings were written in bulk ChGs ($As_{42}S_{58}$ /$As_{36}Sb_6S_{58}$/ $As_{36}Ge_6S_{58}$) via 26 MHz femtosecond laser pulses at ~800 nm wavelength. A 10X microscope objective (NA=0.25) was used to focus the laser beam into the sample. The laser pulse energy was kept constant below the ablation threshold of each material and only the writing speed was varied to change the laser dose. The size of written gratings was 1.5 mm × 1.5 mm and the grating period was 20 µm. The grating depth was estimated via DIC optical microscope measurements. The diffraction efficiency was measured and laser-induced Δn was calculated from the measured diffraction efficiency and grating depth with the equation in the section 4.2.1.4. Figure 4.21 shows the estimated laser-induced Δn as a function of laser dose. It can be seen that Δn exhibits a similar trend to the laser dose induced photo-expansion. It should be noticed that although the laser-induced Δn is proportional to the laser dose, the compositional difference leads to different magnitudes of Δn at similar laser dose. It is evidenced that near a laser dose ~10kJ/cm^2, up to 3~4 times greater Δn is seen in $As_{36}Ge_6S_{58}$ as compared to $As_{42}S_{58}$. It is also interesting to note that the peak Δn of almost 10^{-2} is seen in the binary glass.

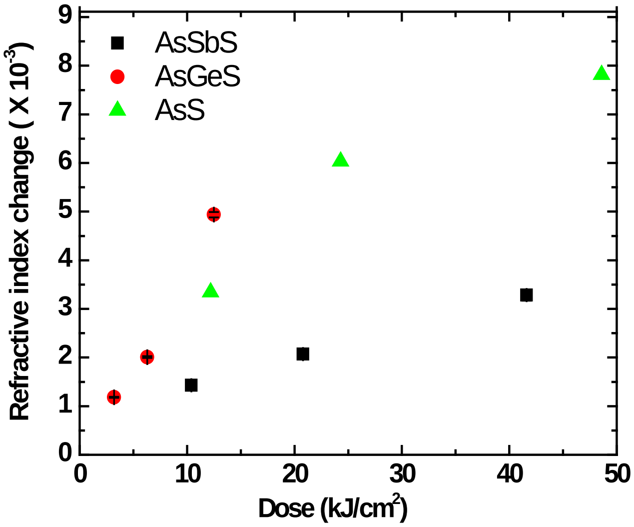

Figure 4.21 Laser-induced Δn of bulk $As_{42}S_{58}$ /$As_{36}Sb_6S_{58}$ / $As_{36}Ge_6S_{58}$

CHAPTER 5 : FEMTOSECOND LAER WRITTEN DIFFRACTIVE OPTICAL ELEMENTS

As discussed in the previous chapters, the strength of the FLDW technique is its flexible patterning scheme and 3-D structuring capability, making it a natural choice for fabricating custom-designed 3-D photonic devices, especially volumetric 3-D phase DOEs that require precisely controlled refractive index modification in micrometer scale.

This chapter reviews the current state-of-the-art in 3-D DOE fabrication, mainly concentrating on embedded phase type FZPs using FLDW, and makes suggestions on how to overcome the limitations of the prior works.

5.1 Prior results of fabrication of FZPs using FLDW

5.1.1 Embedded Fresnel zone plates

FZPs, perhaps the most classical and simplest form of DOEs, are thin and planar diffractive structures operating as focusing optics that are preferred in many applications seeking compactness and simple fabrication process. Thus, FZPs have been investigated as a substitution of refractive optics for their compactness towards integrated micro-optical devices and imaging systems utilizing micro-optics.

Watanabe et al. demonstrated the first femtosecond laser written embedded FZP in fused silica which was an amplitude type binary FZP; this structure however possessed micrometer size voids leading to high scattering and additional absorption [20]. As a consequence, this type of FZP exhibited extremely poor diffraction efficiency, less than 3 % at 632.8 nm, limited primarily by void-induced loss.

The phase type binary FZP demonstrated by Bricchi et al. overcame this diffraction efficiency drawback by replacing voids with laser-induced refractive index change to increase diffraction efficiency [22]. These FZPs showed highly improved diffraction efficiency, up to 39% at 404 nm, and relatively lower efficiencies at 550 nm and 642 nm. They explained that the laser-written structure provided greater phase shift for shorter wavelength because the effective length of the modified region is longer for shorter wavelength even though the physical modification length is fixed. Interestingly, their FZPs exhibited birefringence, hence, the diffraction efficiency was varied not only as a function of wavelength but also the polarization of the probe beam. The diffraction efficiency in one polarization was only ~17% of the diffraction efficiency of the orthogonal direction. Figure 5.1 shows the optical microscopic images of both amplitude [20] and phase [22] type laser written FZPs.

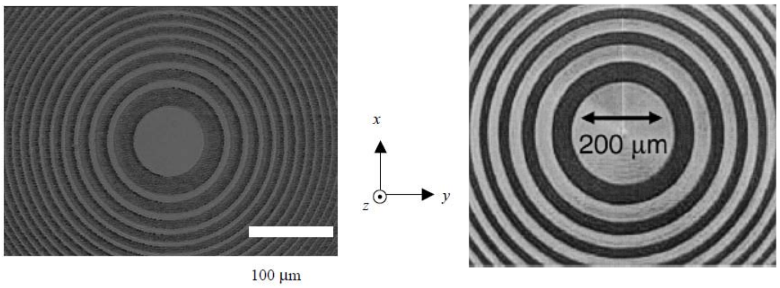

Figure 5.1 Amplitude type by void formation from [20] (left) and phase type FZP by laser-induced refractive index change from [22] (right)

Binary FZPs (Figure 5.1) have a theoretical diffraction efficiency of 40.5%, insufficient for most applications. In 2004, Yamada et al. demonstrated a multilevel FZP which was realized as a four-level structure and provided ~58% diffraction efficiency at 632.8 nm (Figure 5.2, left) [21]. In the case of four-level FZP, the theoretical diffraction efficiency is 81%.

In spite of this high efficiency, the fabrication time to create the FZP structure was extremely long (21 hours). Such a long manufacturing time is not attractive for practical use. Srisungsitthisunti et al. proposed a central ring method which is the replacement of a full-width Fresnel zone by the single track of index change to reduce the fabrication time (Figure 5.2, right) [23]. Consequently, their central ring FZP showed very low diffraction efficiency with a single layer. In order to increase the device efficiency, they proposed a volumetric scheme which accumulates the phase shift by the stacking of appropriately located layers of the central ring FZP. They optimized the distance between layers to cause an in-phase cumulative phase shift from each layer.

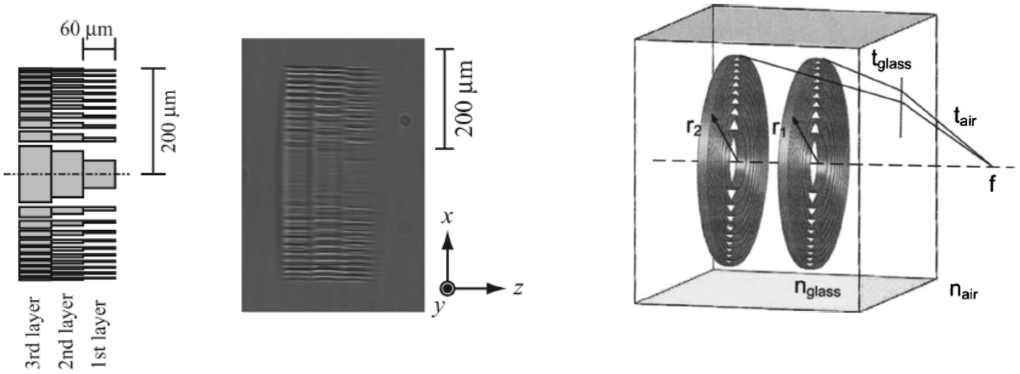

Figure 5.2 Four-level FZP from [21] (left), and volume Fresnel Zone Plate composed of central ring. From [23] (right)

In Table 5.1, the specifications of the femtosecond laser written embedded FZPs are shown. The majority of the prior works have been done using 1 kHz repetition rate pulses. Laser written FZPs suffer from low diffraction efficiency due to the low photo-induced refractive index change. To increase the refractive index change, either a slow writing speed to increase cumulative laser dose or thick FZPs consists of many layers to increase cumulative phase shift are required. However, both cases cause extremely long fabrication time at 1 kHz which is not desired for practical applications. The demonstration in ref [22] provided high diffraction efficiency, close to its theoretical limit (40.5%), however previous research results showed only at limited range in polarization and short wavelength.

This section clearly shows the challenges in fabrication of embedded FZPs using FLDW as following. First, it should offer high diffraction efficiency regardless of the input polarization. Second, the fabrication should be compatible with a practical requirement which implies short fabrication time. Then the aim of this dissertation, to provide a solution of those challenges, can be justified. The investigation to develop a protocol towards the goal is present in section 5.3.

Table 5.1 Specifications of FZP demonstrations

Type	Material	Diffraction efficiency (%)	Probe beam wavelength (nm)	Writing Rep. rate (kHz)	Pulse energy (μJ)	NA	Writing speed (mm/s)	Fabrication time (h)
Amplitude [20]	Fused silica	2	632.8	1	0.4	0.55	-	-
Phase (binary) [22]	Fused silica	39	404	250	1.3	0.55	0.4	-
Phase (multilevel) [21]	Synthesized silica	56.9	632.8	1	0.8	0.3	0.005	21
Phase (central ring) [110]	Fused silica	71.5[7] 7.1	632.8	1	10 ~ 15 0.1	0.15 0.8	0.01	< 6[8]

---

[7] For eight layers

[8] Estimated from ref[6],40 minutes per layer

5.1.2 Surface relief Fresnel zone plates

Two-photon polymerization is a pathway to realizing 3-D free standing structures that exploits FLDW. Chen et al. demonstrated eight-level reflective diffractive FZP shown in Figure 5.3 by two-photon polymerization followed by electroless plating [114]. It is probably the highest multilevel FZP structure fabricated via FLDW up to date. They obtained high diffraction efficiency up to ~68 %.

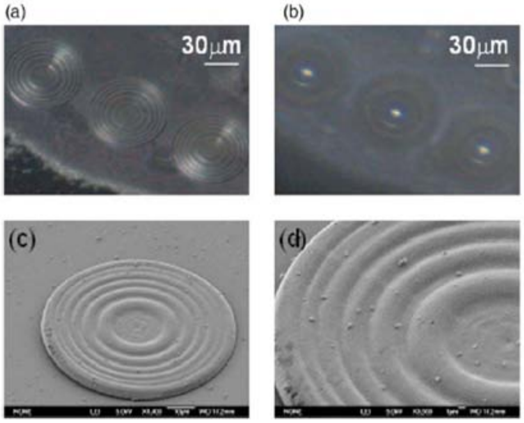

Figure 5.3 Reflective diffractive FZP fabricated by two-photon polymerization. From [114]

Kim et al. produced a binary FZPs on the surface of a mode-expanded hybrid optical fiber shown in Figure 5.4, which can also be an example of the post processing of FZP onto a commercial device [115]. To enlarge the surface area of the single mode fiber whose diameter is 10 μm, a coreless silica fiber with 200 μm diameter was attached as a beam extension element on the single mode fiber. The FZPs were produced on the other end of the coreless fiber by direct ablation using a 1 kHz femtosecond laser and 23 and 11 Fresnel zones were produced for the focal lengths of 300 μm and 600 μm respectively (Figure 5.4(b)). The focused beam sizes were estimated to be 10.9 μm for f = 600 μm and 10.4 μm for f = 300 μm. The diffraction efficiency was not specified; however, binary type FZPs made by direct ablation are supposed to have low diffraction efficiency due to the scattering loss.

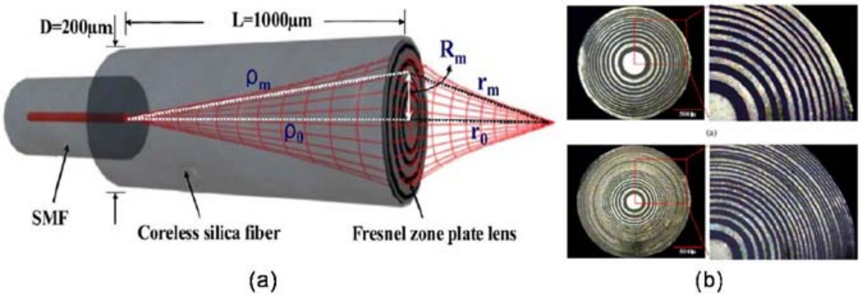

Figure 5.4 Binary FZP created on a coreless silica fiber attached on to a single mode fiber. From [115].

5.2 Femtosecond laser written FZPs

In this section, the basic knowledge on the FZPs, including the formulation, is offered. The custom design parameters and fabrication conditions of laser written FZPs produced by this work are also provided.

5.2.1 Fresnel zone plates

A side view of a binary FZP is shown in Figure 5.5. To formulate the radius of a Fresnel zone plate, the illustration depicts two light paths traveling from s to p: one is d + d' and the other is z + f. The path difference between two paths can be expressed as Δ(r) shown in Eq. (5.1)[116].

$$\Delta(r) = (d + d') - (z + f) = \sqrt{r^2 + z^2} + \sqrt{r^2 + f^2} - (z + f). \tag{5.1}$$

In order to have an integer multiple of half the wavelength for the condition of the Fresnel zone plate (the phase of adjacent zones cancel each other out), the path difference Δ(r) has to satisfy Eq. (5.2)

$$n\frac{\lambda}{2} = \Delta(r)\,, \tag{5.2}$$

where λ is the wavelength of interest and f is the focal length of the FZP.

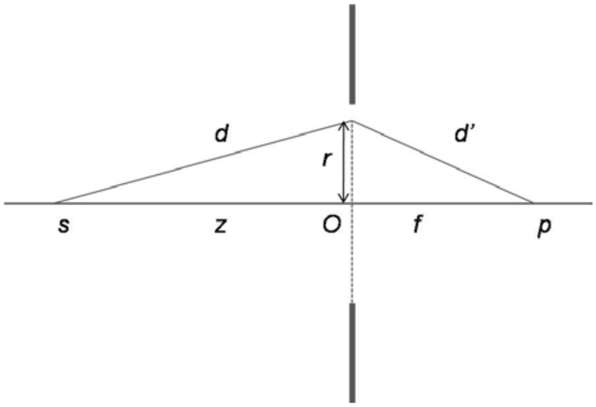

Figure 5.5 Side view of a binary FZP (reproduced from the illustration in [113])

The R_n, which is the n^{th} zone boundary radius of a FZP is then

$$R_n^2 = \left(f_o + \frac{n\lambda}{2} \right)^2 - f_o^{\,2}\,. \tag{5.3}$$

When n becomes large, the square of λ can be ignored and the R_n can be approximated as

$$R_n \cong \sqrt{n\lambda f}\ . \tag{5.4}$$

For multilevel FZP with N-level, the equation can be modified as Eq. (5.5) [117]

$$R_n = \sqrt{\left(\frac{n\lambda}{N} \right)^2 + \left(\frac{2n\lambda f}{N} \right)}\,. \tag{5.5}$$

It should be noted that the formulation is made under the assumption that the focal point is in air. In the case of embedded FZP produced by FLDW, Eq. (5.4) and Eq. (5.5) should be modified as Eq. (5.6) when the focus is located in the same media. Therefore, the λ has to be substituted by λ/n_o , where n_o is the refractive index of the substrate.

$$R_n \cong \sqrt{\frac{n\lambda f}{n_o}}\,,$$
$$R_n = \sqrt{\left(\frac{n\lambda}{n_o N}\right)^2 + \left(\frac{2n\lambda f}{n_o N}\right)}\,. \tag{5.6}$$

Diffraction efficiency of the multilevel FZP with N levels can be described as Eq.(5.7) [117]

$$\eta_N = \left[\frac{\sin(\pi / N)}{(\pi / N)}\right]^2. \tag{5.7}$$

Figure 5.6(a-e) shows the illustration of the common refractive lens and several FZP schemes. Figure 5.6(b) and (d) shows binary phase lenses while Figure 5.6(c) and (e) shows quaternary lenses which are four level phase lenses.

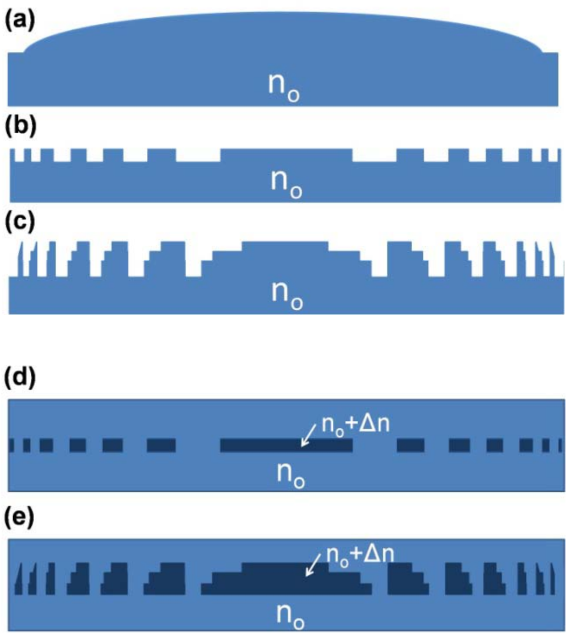

Figure 5.6 Illustration of (a) refractive lens (η=100%) and (b,c) surface relief diffractive lenses (b) Binary lens (N=2, η=40.5%) (c) Quaternary lens (N=4, η=81%), (d-e) embedded phase lenses (d) Binary and (e) Quaternary lens

For the binary FZP with single layer, N=2 and the theoretical diffraction efficiency is 40.5% while the quaternary FZP has 81% diffraction efficiency. In terms of the FZP shape, Figure 5.6(b) and (c) depict surface relief zone plates and (d) and (e) illustrate embedded zone plates. In laser direct writing, Figure 5.6(b-c) can be produced by either direct ablation or laser-assisted etching in order to produce surface relief by material removal. The phase difference results from the index difference between air (n=1) and the refractive index of the substrate (n_o). For embedded zone plate in Figure 5.6 (d) and (e), the index difference between the laser modified region and the refractive index of the material causes a phase difference.

The maximum diffraction efficiency is obtained when the optical phase shift is π, corresponding to the half of the wavelength, and causes constructive interference at the primary focal point. The phase shift $\Delta\phi$ induced by femtosecond laser writing is defined as

$$\Delta\phi = \Delta nl = \frac{\lambda}{2} = \pi \tag{5.8}$$

where Δn is a photo-induced refractive index change, l is a modification length, and λ is the wavelength of interest. Hence, the phase shift (ultimately diffraction efficiency) can be controlled by changing Δn or l. It implies that the manipulation of diffraction efficiency as functions of Δn or l is achievable by changing fabrication parameters, such as laser dose, laser repetition rate, the NA of focusing optics, substrate materials, or the number of stacked layers.

5.2.2 Fabrication and diffraction efficiency measurement

The FZP was designed for a wavelength of 543.5 nm which is selected for the test wavelength in the diffraction efficiency measurement setup. The focal length and the diameter of the FZP was 20 mm and 1.3 mm respectively. The NA of the FZP was calculated as ~ 0.033. Designed FZPs were created in bulk borosilicate (EAGLE2000, PTG). The thickness of the substrate was 1.1 mm and the surface area was 2 × 2 square inches. FZPs were written using different laser repetition rates, NA of objectives and pulse energies.

Two femtosecond laser systems (LS II and LS III) described in Chapter 3 were used to fabricate FZPs. The laser irradiance was below the damage threshold of borosilicate, and therefore did not create voids in the glass. A phase type FZP, relying on the photo-induced refractive index change, was produced. The laser parameters for the different repetition rates used in the fabrication process are shown in Table 5.2.

Table 5.2 Laser parameters at 1 k, 100k, 200 kHz and 1 MHz

	1 kHz (NA=0.15)	100 kHz (NA=0.15)	200 kHz (NA=0.15)	1MHz (NA=0.45)
Laser power on sample (mW)	2	250	300	225
Pulse energy (µJ)	2.0	2.5	1.5	0.2
Fluence (J/cm2)	6.0	4.8	2.9	3.9
Irradiance (TW/cm2)	50.1	10.7	6.5	8.7

The maximum photo-induced change at the 1 kHz laser system (LS II) considering fabrication time-efficiency was obtained when pulse energy ~ 2 µJ and writing speed, 10 µm/s were used. The diffraction efficiency of FZP at 1 kHz was compared to the result at higher repetition rates. A low NA objective lens (NA=0.15) was used for 1 kHz. Various objective lenses from NA=0.15 to NA=0.45 were tested for 100 kHz, 200 kHz and 1 MHz and finally NA=0.15, and NA=0.45 were used for 200 kHz and 1MHz respectively. In Table 5.2, the irradiance at 1 kHz was much higher than other repetition rates while the fluence on the sample was in the same order of magnitude regardless of the repetition rate. The pulse width of a Ti:Sapphire laser was ~4 times shorter than the other system. Except 1 kHz pulses, the pulse energies were the maximum energy of the system at each repetition rate. Central ring and fully filled normal zone plates were produced to compare the diffraction efficiency and corresponding fabrication time. The optical microscopic images of central ring and normal zone FZPs are shown in Figure 5.7.

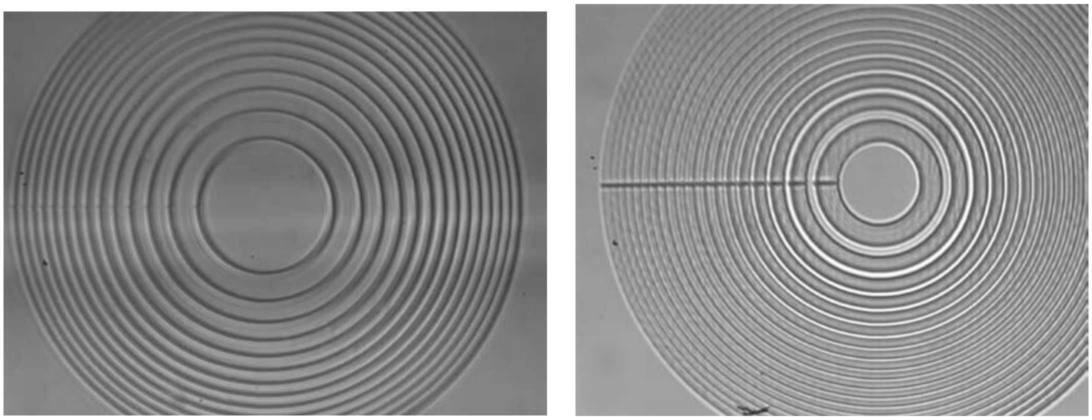

Figure 5.7 Laser written embedded FZPs at 100 kHz (a) 7 layers of single track with 0.5 mm/s writing speed (b) 4 layers of full zone with 1 mm/s

After direct writing, the diffraction efficiency was measured using a power meter (Ophir, PD200) and near field focus profiles of the fabricated FZPs were acquired using a CCD beam profiler (Spiricon Inc., SP-980M). Diffraction efficiency was systematically investigated as functions of laser writing parameters. It was estimated by calculating a power ratio between an input beam and its primary focus through the FZP.

5.3 Results

The diffraction efficiency of phase type FZP are present as functions of laser repetition rate, laser dose, optical power of the objective lens and number of layers of FZP. First, this work describes the influence of NA, repetition rate and laser dose and the number of layers to obtain the maximum DE. Both single track FZPs and full zone FZPs are investigated. This section also discusses fabrication time of FZPs under various repetition rates.

5.3.1 Single layer

A central ring method was first investigated to simplify fabrication process for minimization of fabrication error which might be introduced by cumulative uncertainty. With this approach, photo-induced refractive index change and modification length per single layer could be optimized. A normal FZP was produced to study the figure of merit of the fabrication time as functions of writing speed and beam overlap rate of each track in a filled zone.

5.3.1.1 Central Ring: optimization of NA

A variation of the diffraction efficiency (DE) depending on the NA of the objectives was investigated. Three objectives (NA=0.15, 0.25 and 0.45) were examined at 200 kHz. The corresponding pulse energy was 1.31~1.52 μJ depending on the transmission of the objectives. The confocal lengths are calculated to be 156 μm, 56 μm and 17 μm for NA =0.15, 0.25 and 0.45 respectively at 1043 nm in the borosilicate (n_o=1.5). Figure 5.8 shows the DE of central ring FZPs as a function of NA and their confocal length (shown in the inlet). At 200 kHz, the highest DE was obtained with the lowest NA (0.15) and it is decreased as NA is increased. As shown in inlet of Figure 5.8, the DE for 200 kHz was proportional to the confocal length.

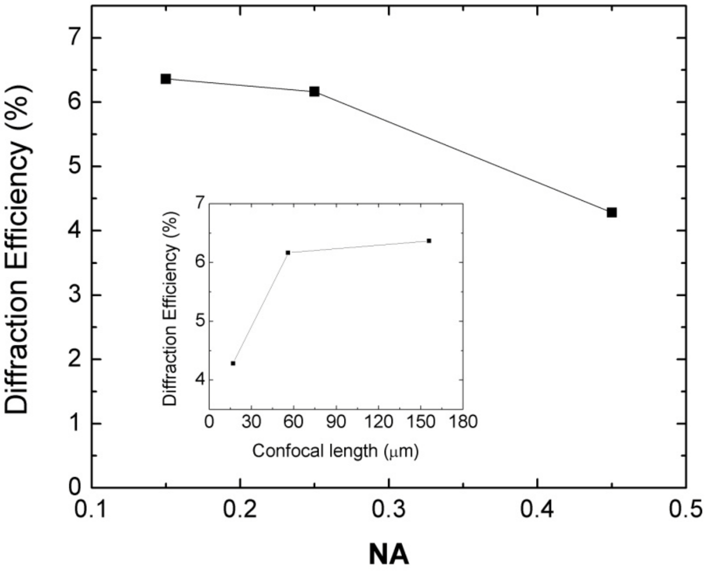

Figure 5.8 Diffraction efficiency varied by a function of NA (inlet, diffraction efficiency varied by a confocal length)

5.3.1.2 Central Ring: optimization of repetition rate

The DE was investigated in terms of the repetition rate as a function of laser dose. Laser dose can also be varied as functions of laser pulse energy and number of pulses, which can be easily controlled by varying translation speed of the sample. Since the FZPs were made in the bulk material, this work assumed a 3-D unit of the laser dose involving pulse energy and translation speed to describe the influence of the laser dose to 3-D structure. Laser dose D, having unit of J/cm^2 is redefined as volumetric unit J/cm^3 by Eq.(5.9) [118].

$$D = \frac{E_p Q}{Av} \tag{5.9}$$

Where E_p is the pulse energy, Q is the laser repetition rate, and v is the writing speed. A is the cross sectional area of the voxel normal to the direction of the sample translation. In our case, A is equal to $2\pi n_o w_o z_o$ which is the cross section of the ellipsoid where n_o is a refractive index of the medium, w_o is the beam waist and z_o is the Rayleigh length. All DE measurements were present using this unit.

Single layers of FZP were made at 1 kHz, 100 kHz, and 200 kHz by a central ring method. An objective with NA=0.15 was used to obtain high a DE. Laser power was kept constant (Table 5.2) during all fabrications at each repetition rate. The laser dose was thus only varied as a function of writing speed which varies the number of pulses per unit area. The laser parameters at different repetition rates are given in Table 5.2. The scanning speed was 0.1, 0.5, 1 and 2 mm/s at 100 kHz and as 0.25, 0.5 and 1 mm/s at 200 kHz. The corresponding laser doses are given in the x axis in Figure 5.9. Clearly, faster writing speed corresponds to the lower laser dose and vice versa.

As shown in Figure 5.9, the overall trend of the DE of single layer FZP was proportional to the laser dose, which corresponds with the prior research that indicates higher laser dose induces more refractive index change [82, 86, 119]. The DE at 100 kHz and 200 kHz is much higher than 1 kHz at the laser dose of under 1 MJ/cm^3, although the pulse energy and irradiance at 1 kHz was higher than 100~200 kHz (Table 5.2). It is three times higher at similar laser dose for 200 kHz than 1 kHz. First, it is thought that the longer modification length due to the longer wavelength of 1043 nm would be one reason to lead to the higher DE. The confocal length of the objective lens (NA=0.15) is ~156 µm at 1043 nm and ~125 µm at 800 nm. The modification length was close to the confocal length for both cases. But, it is not the dominant factor to explain the difference. It is assumed that high repetition rate, over one hundred kHz, produces higher Δn resulting from the thermal effect due to accumulation [46, 120].

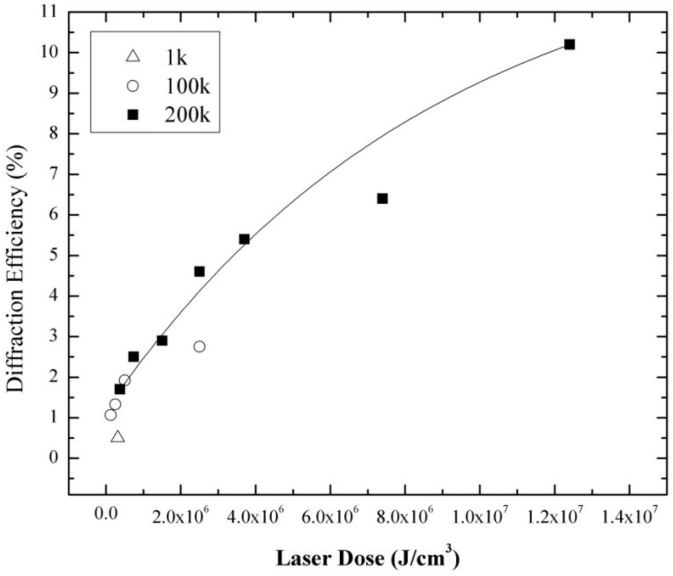

Figure 5.9 Diffraction efficiency for a single layer of the single track FZPs as a function of laser dose at different repetition rate. The scanning speed was converted as laser dose

5.3.1.3 Normal FZP: optimization of repetition rate

The increase in DE is dependent on the repetition rate is clearer in Figure 5.10 for normal zone FZPs. The DE at 200 kHz is higher than at 100 kHz even at similar dose and at the same wavelength. The pulse energy was smaller at 200 kHz under similar dose. It implies that the higher photo-induced Δn, due to the localized heat accumulation is primarily responsible for the difference. It confirms the prior research by Eaton et al. [120] that indicates the initiation of heat accumulation was found at 200 kHz with the same type of glass.

The fabrication times are also drastically reduced at 100 kHz and 200 kHz, ranging from ~2 minutes for the lowest DE (1.7%) to 40 minutes for the highest DE (10.2%) whereas prior result demonstrated 90 minutes for 1 kHz (DE = 0.5%). It supports that high repetition rate lasers are very useful, not only for high efficiency but also fast fabrication process. The evidence of the increase of the diffraction efficiency due to high repetition rate is discussed in detail in the next section.

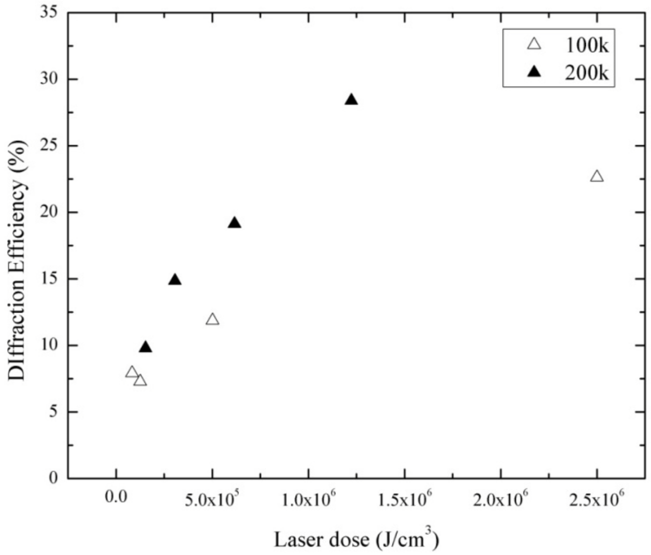

Figure 5.10 Diffraction efficiency as a function of laser dose at 100 kHz and 200 kHz.

5.3.1.4 Normal FZP: Figure of merit

There is a tradeoff between fabrication time and diffraction efficiency for FZPs produced by FLDW. Table 5.3shows the fabrication time depending on the writing speed and FZP type (normal zone vs. central ring). Figure of merit (F) was defined as diffraction efficiency per fabrication time in minutes compared to the efficiency generated from the different fabrication conditions. As shown in Table 5.3, normal zone plate shows much higher F than the central ring zone plate. In the prior research [23], the central ring volume FZP method was considered to reduce the fabrication time. However, the method is not suitable where compact device size is required since they obtained maximum DE with 8 layers of Central ring volume FZPs which is ~1 mm thickness. As the fabrication time is dramatically reduced by the use of high repetition rate pulses, several layers of normal zone plates produced by using higher repetition rates over 100 kHz would be more efficient for compact device fabrication than central ring volume FZPs.

The FZPs produced by faster writing speed exhibit higher F (Figure 5.11). As the fabrication time is decreased, the DE is also decreased, but the decrease rate is slower than the fabrication time. Hence the figure of merit increases as writing speed increases, but is slightly saturated over 1mm/s. Optimization of spacing between tracks is also investigated. The maximum figure of merit was obtained for 2 µm spacing, corresponding to the ~ 67% overlap between adjacent tracks in a filled zone (Figure 5.12). The most efficient single layer of normal zone FZP can be produced with the writing speed around or greater than 1 mm/s with 67% overlap. One can produce efficient FZPs by stacking several layers of the optimized single layer with reasonable fabrication time. It is interesting to compare the figure of merit, F of the DOEs demonstrated in the prior work, reviewed in the previous section with the best result of this work, which is F=2.55 for 2mm/s writing speed. As present in Table 5.1, the FZP produced by Srisungsitthisunti et al. exhibited 71.5% efficiency with ~ 6 hours of fabrication time. The F of their FZP is 0.23, which is only 10% of the result shown here. The F of Yamada et al. shows poorer value: with the 56.9% diffraction efficiency and 21 hours of fabrication time, the F is only 0.047, which is 2% of this work. This comparison proves clearly that the fabrication protocol suggested by this investigation achieved not only the improvement of diffraction efficiency, but also short fabrication time.

Table 5.3 Fabrication time, diffraction efficiency and figure of merit of 3-D FZPs

Writing speed at 200 kHz	Single track plate			Full zone plate (67% overlap between tracks)		
	Fabrication time, T (minute)	DE, η (%)	Figure of merit, η/ T (%/minute)	Fabrication time, T (minute)	DE, η (%)	Figure of merit□, η/ T (%/minute)
2mm/s	1:40	-	-	3:50	9.8	2.55
1mm/s	3:00	1.7	0.57	6:54	14.9	2.16
0.5mm/s	6:00	2.5	0.42	13:45	19.1	1.39
0.01mm/s (at 1kHz)	300:00	0.5	0.0017	-	-	-

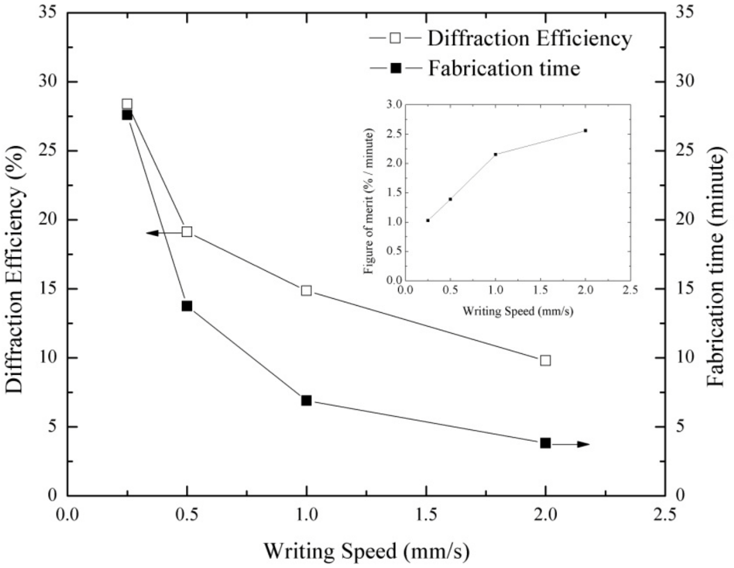

Figure 5.11 8 Full zone with different writing speed at 200 kHz (inlet is figure of merit)

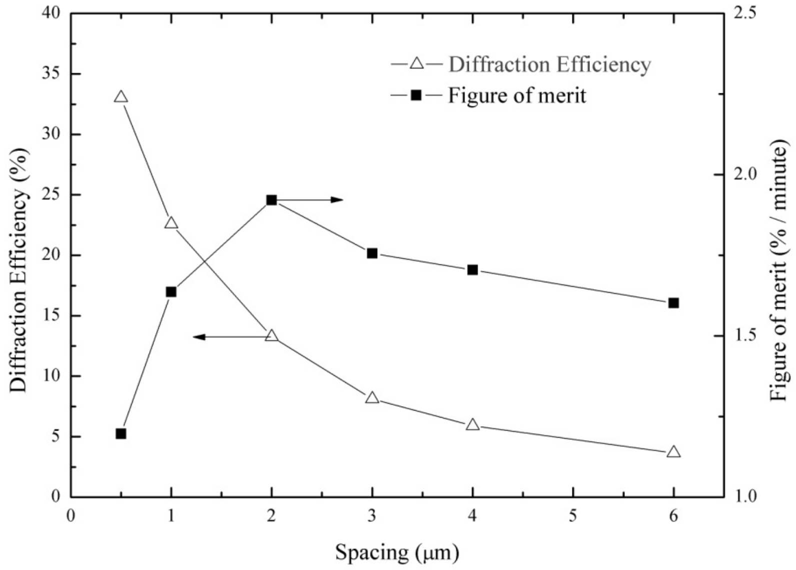

Figure 5.12 Full zone with different spacing with the writing speed of 1 mm/s at 200 kHz

5.3.2 Multi layer

It is a challenge to obtain very high DE with single layer phase FZP due to small photo-induced Δn. Consequently stacking of multiple layers is of interest to increase DE of the laser written FZPs [21, 23]. Here the trend of DE as a function of the number of layers was investigated to look at the evolution regarding phase accumulation. This work describes the effect of stacking for central ring and normal zone FZPs under various fabrication conditions. Layers of central ring and normal zone FZP were stacked coaxially with the separation distance of ~150 μm. The first layer was written at the location which was the bottom layer. Then the sample was moved downward as the layers separated (~150 μm) so that the writing beam propagation was not interrupted by the written structures. The stacked FZPs were produced at 100 kHz and 200 kHz with up to 6 layers.

Figure 5.13(a) shows the DEs of stacked central ring FZPs written at 100 kHz. As shown in the graph, the DE increases as either number of layer or laser dose increases. As described in the previous section, the laser dose was changed by varying the writing speed. The speed was 2, 1, 0.5 and 0.1 mm/s corresponding to the laser dose of 0.13, 0.25, 0.5 and 2.5 MJ/cm^3. The maximum DE for given parameters were ~23% for six layers at dose of 2.5 MJ/cm^3. The fabrication time of a single layer was about 30 minutes. The plateau of DE was observed between the 5th and 6th layer at the highest dose. This is probably caused by the fabrication error. Incoherence between diffracted beams multi-layer configuration would allow higher order phase depth because the theoretical DE of binary FZP is given as ~40%.

Figure 5.13(b) shows the DEs of the central ring FZPs with selected conditions with different writing speed at 100 kHz and 200 kHz. The corresponding laser dose at 1 mm/s and 0.25 mm/s for 200 kHz is 0.3 MJ/cm^3 and 1.2MJ/cm^3 respectively. It is interesting to note that similar DE results were obtained for 100 kHz and 200 kHz even though much less of a dose (fast speed) was applied at 200 kHz.

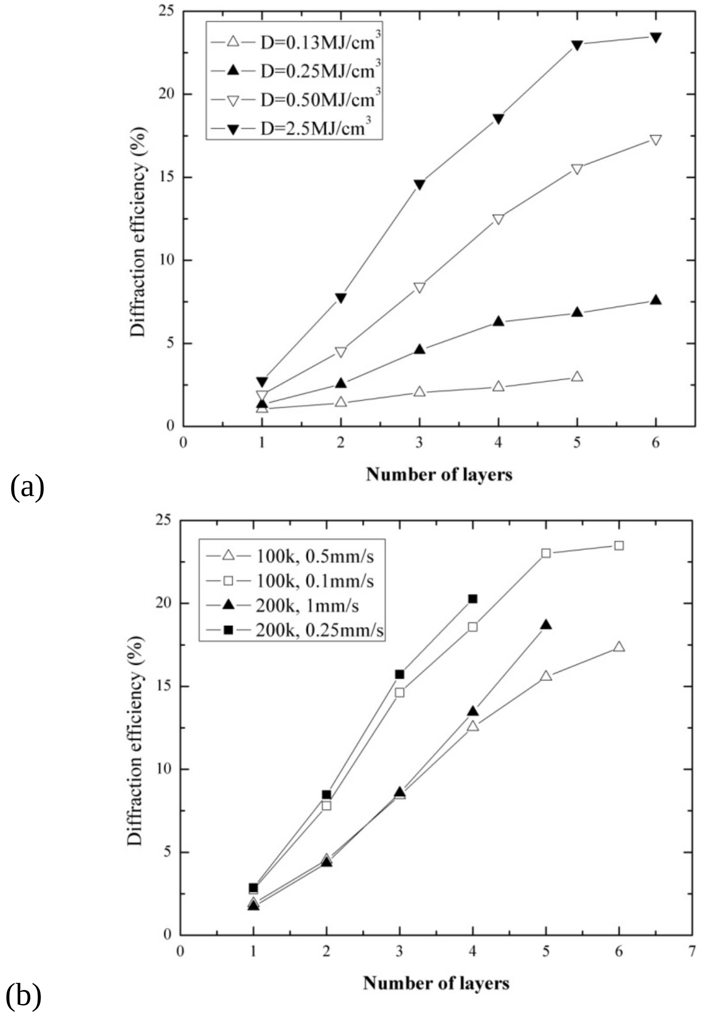

Figure 5.13 DE of the stacked single track FZPs (a) FZPs written at 100 kHz . The corresponding writing speeds are 2, 1, 0.5 and 0.1 mm/s (b) FZPs written at 100 kHz and 200 kHz

This also implies the evidence of heat accumulation effects proposed in the previous section that higher repetition rate would give increased photo-induced refractive index change than lower repetition rate. Using higher repetition rate pulses can reduce fabrication time and laser dose to produce FZPs possessing similar DE written by lower repetition rate pulses. The fabrication time for 0.25 mm/s is ~12 minutes which is only 40% of the fabrication time for

0.1mm/s. In this case, about 50% of the reduction of the fabrication time is obtained for increasing repetition rate from 100 kHz to 200 kHz.

Figure 5.14(a-c) shows the DE of stacked normal zone FZPs at 100 kHz and 200 kHz with varied writing speeds with identical pulse energy across the variance of speed. The DE is increased as the number of FZPs is increased. However, after it reached the theoretical maximum of ~40%, the DE is decreased although the number of layers is increased. It shows intuitively the optical phase shift of a layer under certain fabrication parameters. It is shown in Figure 5.14(a) that the maximum DE is located between 2nd and 3rd layer of FZP at 0.5 mm/s while 3rd and 4th layer for 2 mm/s. It shows the same trend for 200 kHz in Figure 5.14(b). It is also shown to be true for different repetition rates in Figure 5.14(c). The result written with 2 mm/s at 100 kHz and 200 kHz, calculated laser doses are 0.13 and 0.15 MJ/cm^3 respectively.

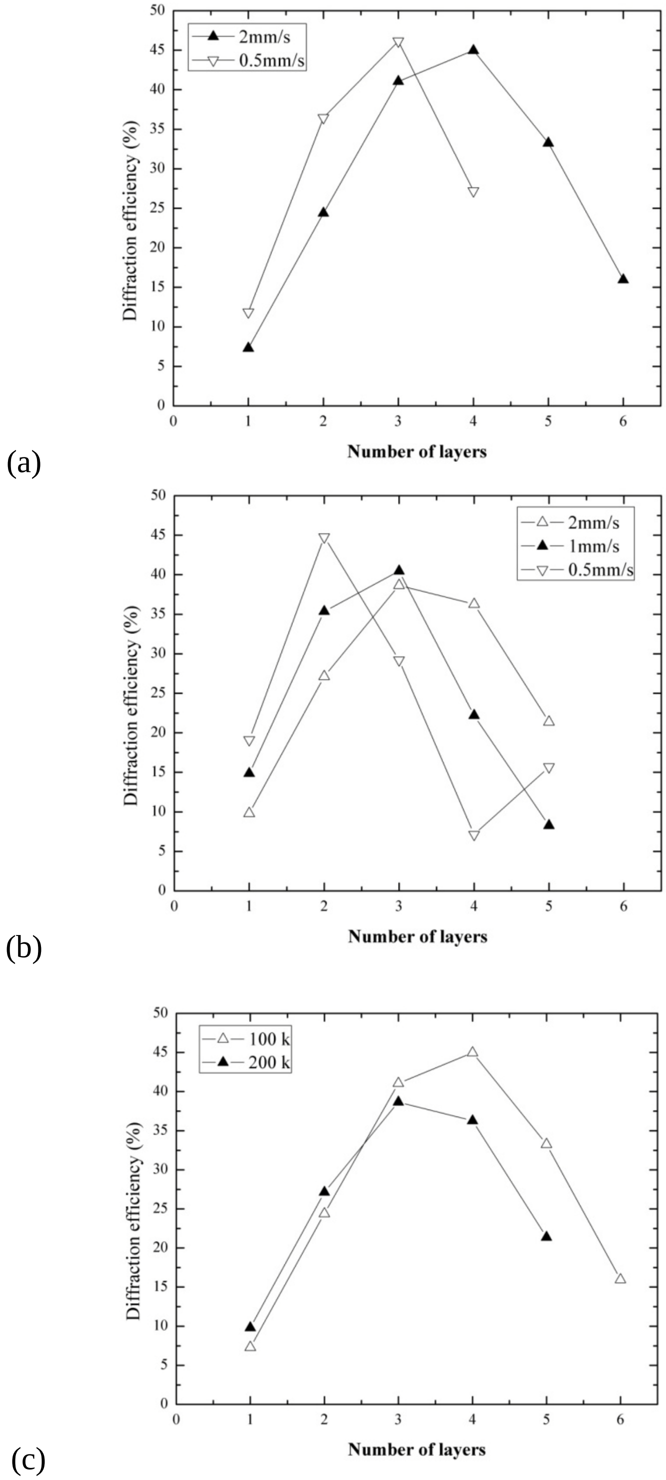

Figure 5.14 (a) DE of the full zone FZPs written at 100 kHz, (b) DE of the full zone FZPs written at 200 kHz (c) DE of the full zone FZPs written at 2 mm/s, 100 / 200 kHz

5.4 Conclusion and possible applications

In conclusion, it was clearly seen that a use of multi-hundred kHz repetition rate laser increased significantly the DE of laser written FZPs. Localized heat accumulation is considered to be responsible for the increase. Fabrication time was also drastically reduced compared to that of 1 kHz. In this way, not only central ring scheme, but also full zone FZPs can be fabricated in a hour with high DE, which is a great improvement from a prior works.

Both central ring FZP and normal FZP was discussed in single layer or multilayer form. The advantage of a single layer of high DE FZP may be the disadvantage of a stacked FZP in terms of number of layers. For instance, single layer FZP with reasonable DE would be appropriated in compact micro-optical device fabrication or imaging application which requires least aberration from FZP. For the application seeking highest DE, multi-layer structures will be suitable, but the image resolution may be decreased while light signal passes multi-layer structure. In this case, multi-layer FZP would fit to applications such as light collection optics.

CHAPTER 6 : INTEGRATION OF MULTIPLE PHOTONIC STRUCTURES

Numerous demonstrations have been made of laser directly-written single photonic devices exploiting FLDW. However, advanced device schemes consisting of multiple laser-written structures integrated on a single chip have not been fully explored. Simple waveguide arrays and a stack of FZPs are the only exceptions [23-25].

This chapter explores the feasibility of integrating multiple photonic structures, as a way to develop a fabrication protocol based on FLDW for integrated optical device platforms. This chapter also presents a few examples of the integrated optical structures that are truly all-optical directly written devices, along with a discussion of their characterization.

6.1 Type of integration

In this section, this work proposes types of integration involving laser written structures and their properties. One is multiplexing and the other is heterogeneous integration. Multiplexing is realized by constructing arrays of the same type of devices to enhance functionality. Heterogeneous integration can be realized by integrating multiple structures with different functionality in a single device. The latter may be a more general meaning of integration. More details of each regime are discussed below.

6.1.1 Multiplexing (homogeneous integration)

The first regime of integration is multiplexing which is the addition of plural structures or duplication that perform identical functions. The purpose of multiplexing is to increase the number of events of interest via parallel processes so that the overall system speed or output can be enhanced. For instance, a 1 × N channel increases the number of event N times. In optical systems, multiplexing can be implemented by such optical elements like beam splitters and micro lens arrays which divide the input beam into plural output beams.

Conceptually, there are two types of beam dividing methods. One is fragmentation (or spatial division) and the other is partial transmission (or power attenuation). Figure 6.1 shows two schematic diagrams of beam division. Figure 6.1(a) is a depiction of spatial beam division using a means to split the input beam spatially. Micro lens arrays or mirrors can be the means in this case. It is easily assumed that the output beams through a micro lens array with N micro lenses can have an equal split 1/N of input power only when the input beam has uniform power distribution and the micro lenses have the same size. Otherwise, the beam profile of the whole input beam cannot be duplicated but fragmented and the power cannot be equally divided in free space optics. The conventional micro lens array as a free space optic belongs to the fragmentation type. Sometimes, this feature is useful for analysis of wave-front distortion and is also known as Shack-Hartmann wave-front sensor.

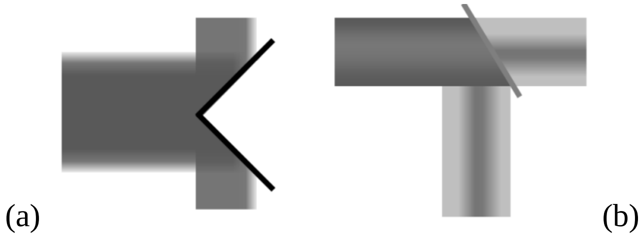

Figure 6.1 Schematic diagram of beam splitting devices (a) type I, fragmentation (spatial division) (b) type II, partial transmission (power attenuation)

Figure 6.2 shows an example of multiplexing implemented by a fiber array and an array of micro lens.

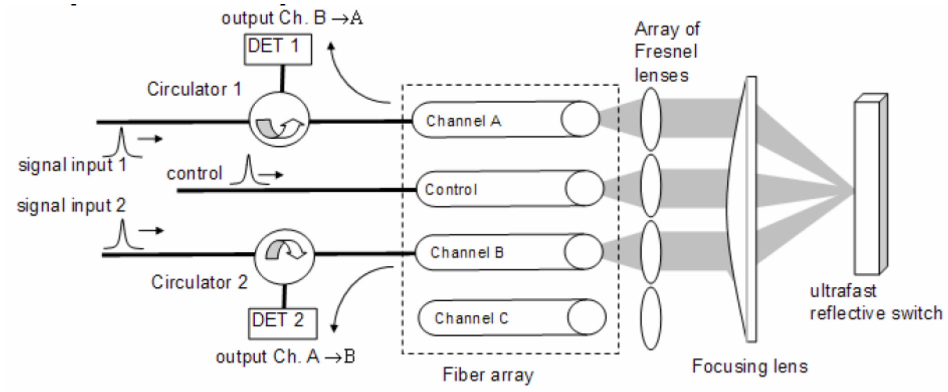

Figure 6.2 An optical multiplex system utilizing an array of the combination of fiber channels and micro lenses. From [121]

The second case is duplication of the input via partial mirror (or beam splitter) as is seen in Figure 6.1(b). In this case, the input beam profile remains the same while the power is attenuated as a given transmission. However, the type II can also be implemented by micro lens arrays. It is feasible by laser-written stacked FZPs because the diffraction efficiency can be adjusted intentionally. With this scheme, each layer acts as a lens and a power attenuator. Furthermore, the attenuation of each layer can be adjusted precisely by varying fabrication parameters as discussed in the previous chapter. Figure 6.3 depicts the concept of such a micro lens array, implemented by a multiplex FZP with a shift s. To maintain the input beam profile, the shift s should be s<<D where D is the diameter of the FZP. The distance d between the layers should be longer than l, which is the depth of a layer, to avoid the loss of overall diffraction efficiency. The focal length of each lens has to be adjusted as shown in Figure 6.3 in order to have the same flat focal plane. Otherwise, the focal length of each layer can be designed to have an intended curved focal plane.

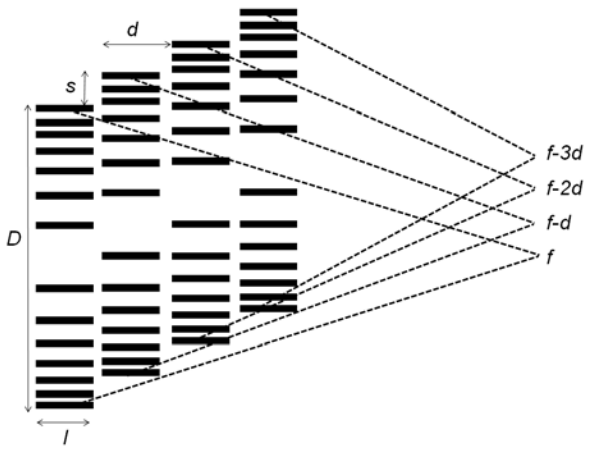

Figure 6.3 Schematic diagram of a stack of spread FZPs

The attenuation power of a layer is determined by the diffraction efficiency of the layer. Then, the input to each layer is affected by the attenuation of the previous layer as in the Eq. (6.1)

$$I_n = (1-\eta_{n-1}) I_{n-1}, \tag{6.1}$$

where I_n and η_n are the input and the diffraction efficiency for the nth FZP respectively.

6.1.2 Integration of heterogeneous structures

The second category is the integration of heterogeneous structures that is the combination of different type of photonic structures performing different functions in a single chip or substrate. In this way, the device exhibits multi-functional performance. Conventional integrated devices require multi-step fabrication processes to construct a combined structure. In FLDW, multiple structures can be written in 3-D within a bulk transparent substrate by a single step process. In Figure 6.4, a schematic depiction of a "built-in coupler" consists of a FZP and waveguide array is shown as an example of this type of integration. The structure has an advantage in terms of robustness and reliability over the conventional coupling devices which are separately made and integrated. The structure is expected to be free from any misalignment issues resulting from thermal or mechanical stress due to the difference of material properties of the devices.

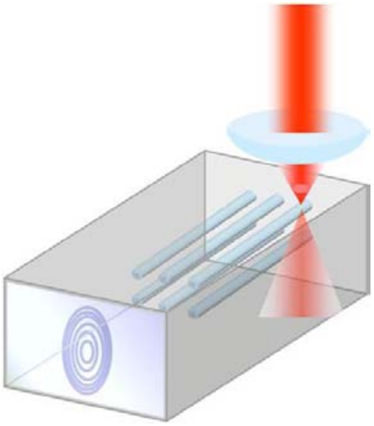

Figure 6.4 Schematic depiction of the integration of a FZP and a waveguide array

6.2 Realization of the integration via FLDW

This work demonstrates a few examples of the realization of the integration of laser-written photonic structures. The characteristic features of each device platform are discussed as well. All the structures demonstrated in this section were produced by the Yb-doped fiber femtosecond laser (LS III) which was described in Chapter 3. In the fabrication process, two microscope objective lenses were used. A lens with NA=0.15 was used for FZP fabrication to obtain long modification depth for high diffraction efficiency. The other is NA=0.4 for waveguide writing to minimize the elongation of the cross-section of the waveguides.

6.2.1 Multiplexing

Figure 6.5 shows a micro lens array consisting of laser-written binary FZPs created in a borosilicate substrate. Each lenslet has a diameter of 600 µm.

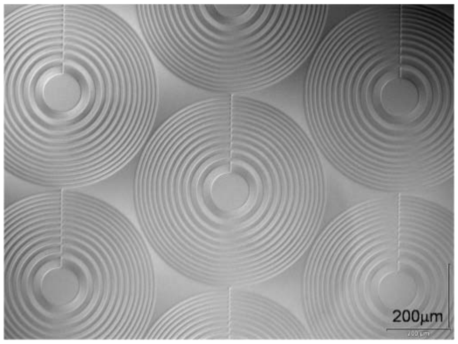

Figure 6.5 Micro FZP array

Another scheme, referred to as a spread FZP stack, was suggested as a 1 × n focused beam separator in the previous section. The realization of 1 × 4 beam separator with a stack of four layers of FZP is shown in Figure 6.6. The structure was inscribed in a borosilicate substrate. For simplicity, the fabrication parameters were kept the same and the single track fabrication was used in order to obtain similar diffraction efficiency. The diffraction efficiency of a layer is not high but the diffracted power was similar among each layer. In this way, simplicity was saved by ignoring the higher order diffraction and possible cross-talk between layers so that the power from the primary focus remained dominant. An assumption was also made that the input beam was diffracted only once at a layer then propagated without further diffraction. As shown in Figure 6.6(c), the intensity of four outputs looks equally distributed and the Gaussian beam profile of the input beam was maintained. The individual diffraction efficiency for primary focus of each layer was measured as DE1:DE2:DE3:DE4=3.2:3.1:2.9:2.9 and the total diffraction efficiency was 11.5%.

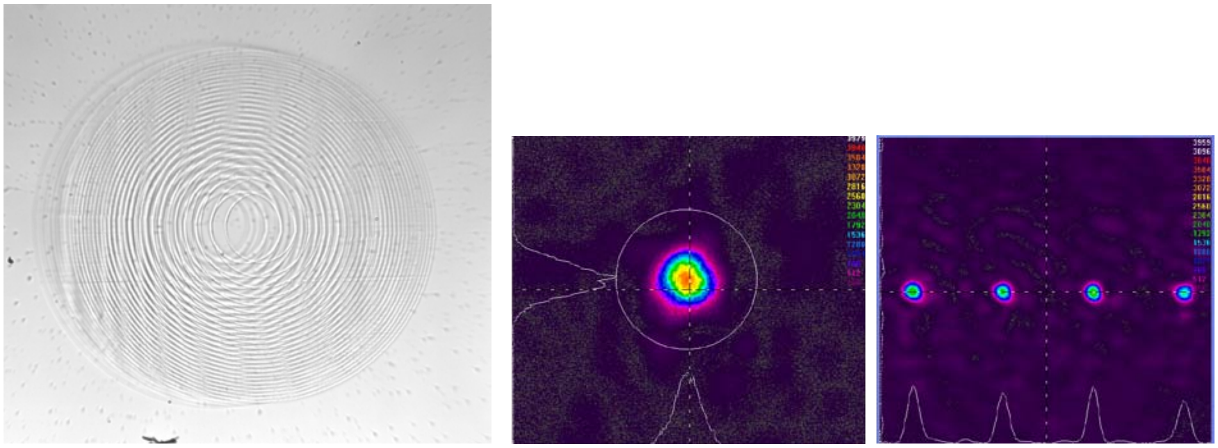

(a) (b) (c)

Figure 6.6 (a) Optical microscopic image of a stacked FZP (b) intensity profile of input from a He-Ne laser (c) four focused beams through a spread FZP measured at the focus plane. The scale of the (b) and (c) is different[9]

6.2.2 Integration of heterogeneous structures

A built in coupler consists of a FZP and a waveguide array with 5 × 5 + 2 array size were fabricated in a borosilicate substrate. The size of the substrate is 50 mm × 50 mm with 1.1mm thickness. The two large surfaces have a good optical quality, but the side wall was not polished. Hence, the surface of the side wall was polished before writing process. Firstly, a FZP with a diameter of ~ 1.1 mm was written ~ 200 µm below the surface. The focal length f of the FZP was designed to be f = 10 mm at 543.5 nm. The sample was then rotated to write a waveguide array. One end of the array was placed at the focal point of the FZP to couple the focused input into the waveguides. The length of the waveguides were made to be ~35mm. Figure 6.7 shows the schematic diagram of the fabricated structure.

---

[9] The $1/e^2$ beam size of input beam is about ~1mm

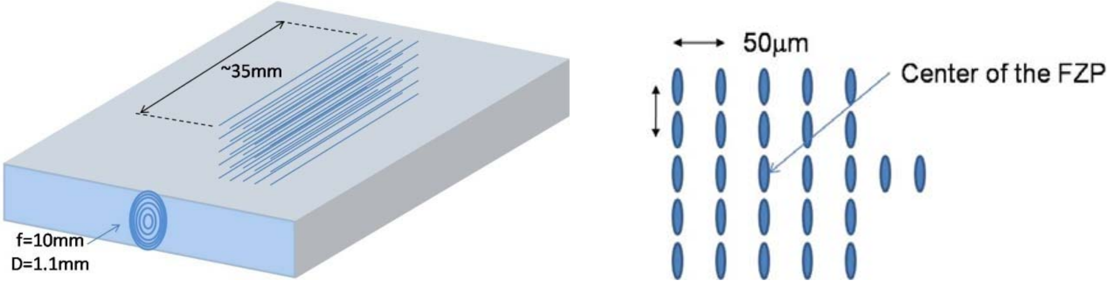

Figure 6.7 A schematic diagram of the integrated optical structure.

The propagated power through the structure was measured using a setup illustrated in Figure 6.8. A HeNe laser at 543.5 nm was used for a probe beam. Although the picture shows that the incidence angle of the input beam was tweaked, in fact, the sample was rotated to change the incidence angle. The sample was mounted on a 5 axis manual stage to tweak not only the translation, but also yaw and tilt. A 10X objective lens was coupled with a CCD beam profiler to acquire near field images of the propagation.

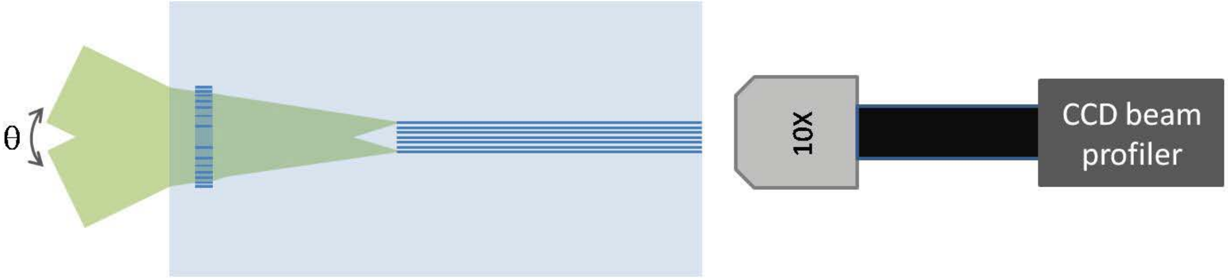

Figure 6.8 Setup for the near field image of the propagation through an integrated structure

Figure 6.9 is the near field images of the propagation through the waveguide array launched by a built-in FZP coupler. Interestingly, the coupling to each waveguide through a FZP was available by rotating the sample with small angle. As is seen, launching from the leftmost waveguide to the rightmost one corresponding to 300 µm distance required a rotation less than

2°. It is also noticed that the coupling from the center waveguide to other waveguides in the vertical direction occurs even though the coupling was made only at the center waveguide. A few possible reasons can be made to understand the observation. The theoretical beam size through the FZP is calculated to be ~13 µm, thus the focused beam should be launched only into one waveguide at the center since the distance between center to center of the waveguides is 50 µm. However the cross-section of the waveguide is revealed as elliptical due to the long beam waist of NA0.4 lens. Thus, the length of the waveguide is estimated to be about 20 µm. This results in a distance between the waveguide of ~10 µm in vertical direction. It infers that there can be cross talks between waveguides leading to an evanescent coupling. However, there is no evidence of coupling in the horizontal direction.

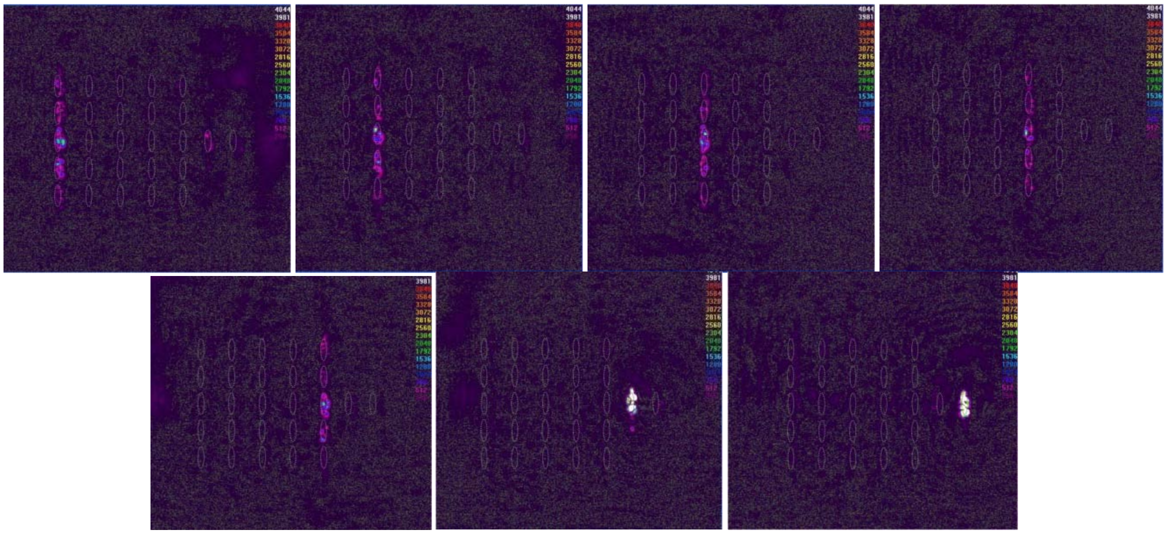

Figure 6.9 Near field image of the propagation through a FZP coupled waveguide array

The total efficiency of the structure was estimated from the ratio of the output power to the input power. It should be noted that the FZP produced in this device is a binary type with a theoretical diffraction efficiency of 40.5%. It implies that the maximum output from the system cannot exceed ~ 101 µW for the input power of 250 µW even if it is a no-loss system. The diffraction efficiency of the FZP was measured separately using a duplicate produced in a different substrate with the same fabrication parameter. According to the measurement, the measured diffraction efficiency of the single FZP was ~ 20% in this case. Hence, the best result can be expected as ~ 50 µW, corresponding to ~ 20% diffraction efficiency with an assumption that no propagation and coupling loss through waveguides are involved. However, the final output from a waveguide was ~20 µW corresponding to ~8 %. After compensation of the intrinsic Fresnel loss for both input and output surfaces of the substrate, the overall system efficiency was obtained as ~9%. It implies that the coupling efficiency including the coupling loss from FZP to waveguide and the propagation loss of 35 mm waveguides were not ignorable. The result can be improved by producing multi-level phase FZP to increase theoretical diffraction efficiency limits. For instance, the theoretical efficiency of a four level phase FZP is 81%, which is double the efficiency of a binary form. However, multi-level phase depth FZP requires a stack of FZPs which means longer fabrication time with increased complexity. One can decide the minimum system efficiency by the trade-off between fabrication time and the application requirement.

Finally, a multiplex FZP consisting of three FZPs with 60 µm shift was combined with a 7 × 1 waveguide array. In Figure 6.10, the optical microscopic image of the multiplex and the waveguide array are shown. The dimensions of the structure are given in the picture. The distance between each layer of FZP was designed to be farther than the depth of a FZP of ~120 µm. The reason for this is to avoid inducing any perturbation due to the overlap that might decrease the overall diffraction efficiency. The diffraction efficiency of each layer was made differently by adjusting fabrication parameters to compensate for the decreased input of the next layer by the previous one. In the picture, the bottom layer is the first FZP toward the laser. To generate a bottom layer with the lowest diffraction efficiency, the lowest laser dose was applied to the bottom layer while the highest dose was applied to the top layer which is the nearest to the waveguide array.

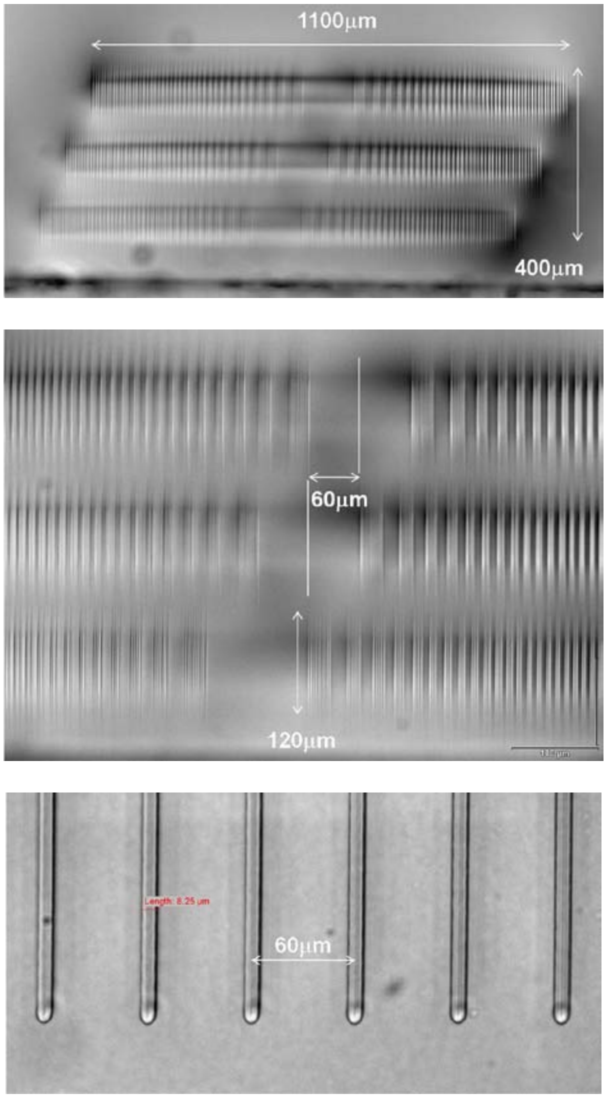

Figure 6.10 Three-piece multiplex FZPs shifted with 60 μm and a 7 × 1 waveguide array

The measured efficiency ratio of each layer is bottom : middle : top = 8:18:23. However, the output which is estimated by the ratio was 7.4:15.3:16 due to the decreased input. Figure 6.11

is the near field images of the integrated structure shown above. As is expected, the propagated beams from three coupled waveguides are seen. However, the coupling and propagation efficiency shows a different ratio compared to the estimation. Figure 6.11(a) has 4.1:4:3.2 while (b) has 5.4:3.8:2.7. This implies that although the structure has definitive diffraction efficiency and propagation loss, small tweak angle variance could change the coupling efficiency to vary the coupling ratio. This also means that variable power transmission through this structure is available even though the optical properties of the structure are fixed.

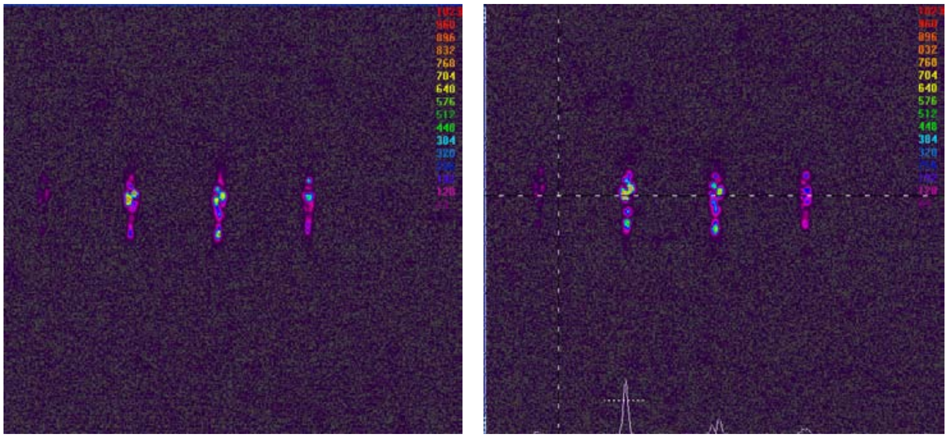

(a) **(b)**

Figure 6.11 Near field images of a waveguide array coupled with a multiplex consists of three FZPs the power ratio is (a) 4.1:4:3.2 (b) 5.4:3.8:2.7

CHAPTER 7 : FEMTOSECOND LAER WRITTEN NONLINEAR OPTICAL STRUCTURES

So far it has been shown that FLDW can fabricate building blocks for integrated optical devices in bulk optical materials based on a modification of their linear optical properties.

In this chapter, another way to enrich photonic applications utilizing FLDW is explored: utilizing nonlinear optical properties of materials. First, nonlinear optical processes and their phenomena are reviewed as a background, and the limitations of amorphous materials as the platform of second-order nonlinear properties are discussed. Then, the recent new finding of “laser-depletion” by this investigation is discussed as a pathway to create second-order nonlinear structures in amorphous glass via high repetition rate femtosecond pulses. The theoretical model of laser-depletion, which enables second-order susceptibility in amorphous glass, is described. Silver ion-containing zinc phosphate glasses are utilized as a substrate of the new scheme of laser-induced second-order nonlinear structure. The most recent experimental result supporting the model is presented. Finally, a series of parametric experimental results as well as analyses of the measurement are presented at the end.

7.1 Nonlinear optical properties of glass

Nonlinear optical processes were discovered immediately after the invention of the laser in 1960 because these phenomena require intense beam intensity to be measured experimentally. Now, numerous applications based on nonlinear optics are providing great opportunities in photonics and optoelectronics. It is well studied that the polarization of dielectric material can be expressed as [36]

$$\tilde{P}(t) = \varepsilon_0[\chi^{(1)}\tilde{E}(t) + \chi^{(2)}\tilde{E}(t)^{(2)} + \chi^{(3)}\tilde{E}(t)^{(3)} + \cdots] \equiv \tilde{P}^{(1)}(t) + \tilde{P}^{(2)}(t) + \tilde{P}^{(3)}(t) + \cdots . \qquad (7.1)$$

In this equation, the polarization of materials has two parts: linear and nonlinear polarization. Linear polarization, which is the first term in the bracket consisting of the linear susceptibility $\chi^{(1)}$ and an applied optical field $\tilde{E}(t)$, is responsible for the material responses in general, such as dispersion, refraction, reflection, and other linear optical phenomena. The rest of the equation which is nonlinearly proportional to the E field is called nonlinear optical parts which are not negligible and often dominant when an intense optical field is applied.

7.1.1 Second-order nonlinearity

The polarization of the second-order of nonlinearity can be described as $\tilde{P}^{(2)}(t) = \varepsilon_o \chi^{(2)}\tilde{E}(t)^{(2)}$. Second harmonic generation (SHG), the Electro-optic effect (or Pockels effect), and sum (difference) frequency generation are all included in the second-order of nonlinear optical phenomena. For example, SHG can be depicted as the schematic energy diagram in Figure 7.1. As is shown, two photons with frequency ω reach the intermediate state which immediately re-emits a photon with frequency 2ω, which is doubled energy.

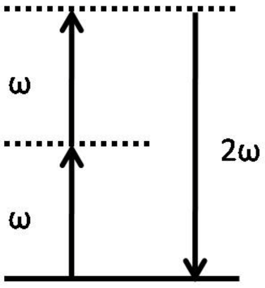

Figure 7.1 Schematic energy diagram of second harmonic generation

Enormous applications such as frequency doubled lasers are relying on this process, which widens the span of laser frequencies from, generally limited laser gain media. The Electro-optic effect is another useful feature of the second-order of nonlinear optic properties. It is widely used for high speed optical switching and the modulation of optical signals in optical communications and laser engineering field [122, 123].

Although these fascinating applications are offered by second-order nonlinearity, amorphous materials possessing inversion symmetry are unable to exhibit second-order nonlinearity. This is because the induced polarization involving $\chi^{(2)}$ is proportional to the vector quantity which is the external electric field in this case. Therefore, the macroscopic vector sum of the polarization is always null in amorphous materials such as glass.

7.1.2 Third-order nonlinearity

The polarization of third-order nonlinearity can be described as [36]

$$\tilde{P}^{(3)}(t) = \varepsilon_o \chi^{(3)} \tilde{E}(t)^3 . \tag{7.2}$$

Some examples of the third-order of nonlinear optical phenomena are third-harmonic generation, the optical Kerr effect, two-photon absorption, and self-focusing. These phenomena are free from the limitations of the material symmetry since these effects depend on the square of the external electric field, which is the laser intensity as a scalar quantity. As a consequence, third-order nonlinearity is, in general, the least order of the nonlinear optical properties allowed in amorphous glasses. For instance, many investigations regarding self-focusing in glasses have been carried out to clarify the laser-induced damage mechanism in optical glasses due to the delivery of the high power laser beam. Another example is two-photon absorption which was intensively discussed in Chapter 2.

7.1.3 Induced second-order nonlinearity of amorphous glass

Glasses have several advantages over nonlinear crystals in terms of practical use. First, there is more freedom in tailoring their optical properties with compositional variance. Also, glasses are easily developed in certain shapes for desired device dimensions from fiber form to bulky, curved shapes. Low cost and ease of handling is another benefit. Although the intrinsic limitations are well understood, utilizing glasses for second-order nonlinear optical applications has been investigated. In 1986, SHG in Si-Ge glass fibers was discovered by Österberg and Margulis [124]. Stolen and Tom [125] proposed a mechanism involving the electric field from a third-order optical rectification. SHG in thermally poled bulk fused silica was first demonstrated by Myers et al. in 1991[126]. Since then, extensive research using poled glasses including silicate, phosphate, and tellurite have been performed to take the advantage of glasses, which are promising for low cost, robust fabrication processes [77, 126-128].

The basic understanding of the second-order susceptibility in poled glass is provided in ref. [125, 126]. The second-order nonlinear susceptibility can be represented as

$$\chi^{(2)} = 3\chi^{(3)} E_{dc}, \tag{7.3}$$

where E_{dc} is the internal electric field induced by a poling process. Thermal poling is commonly used to produce an internal DC field in the material by depletion. Figure 7.2 depicts a schematic of the process. As is shown, the glass substrate is sandwiched by two electrodes in a furnace. Then, the temperature is increased to offer a higher mobility of ions. When the temperature reaches between 200°C to 300°C, a high voltage of 1~3 kV is applied to force the mobile ions to move. The high temperature is kept for ~30 minutes and then is decreased to $T_{Rm.}$ The voltage is then removed from the glass after the glass is cooled down.

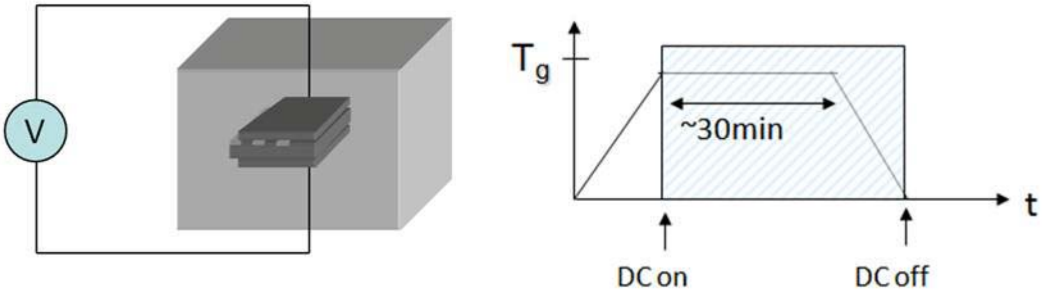

Figure 7.2 Thermal poling of glass

By the thermal poling process, mobile ions migrated from the anode side to the cathode size leaving a depletion zone of few microns at the anode side, depicted in Figure 7.3. The permanent internal electric field from the shift of ions is generated in a depletion zone, which is the basis of the second-order susceptibility of poled glass. Silver, sodium and a few more substances are most commonly used as dopants for depletion.

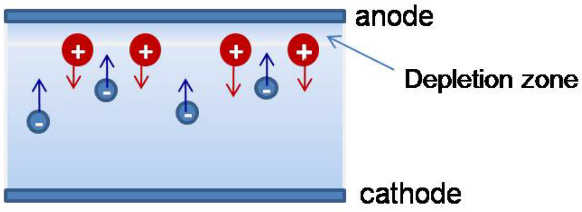

Figure 7.3 Illustration of depletion zone via thermal poling

7.2 Laser-induced depletion

As an analogy of the charge depletion via thermal poling, laser-induced depletion is suggested. Laser-written micro-structures consist of silver clusters with a redistribution of charges resulting in a permanent electric field in the vicinity of the micro-structure. As a consequence, second-order susceptibility involving third-order susceptibility and the internal electric field can be induced. In this section, the mechanism of the creation of micro-structures and laser-induced depletion is described.

7.2.1 Microstructuring of silver containing zinc phosphate glass

It is well known that silver ion containing glass has photosensitivity that helps to create 3-D embedded structures in the glass using laser direct writing [129, 130]. Recently, Bellec et al. [131], who are the collaborators for this investigation, demonstrated sub-diffraction limit laser structuring based on the formation of silver clusters using femtosecond laser irradiation. Figure 7.4 shows a high resolution SEM image of the embedded silver micro-structure and corresponding profiles measured by AFM. The surface of the sample was ground and polished to bring the structure to the glass surface. Next, it was acid-etched for measurement. The width of the rim was measured to be ~ 81 nm (FWHM) which is less than 1/10 of the wavelength of the writing beam.

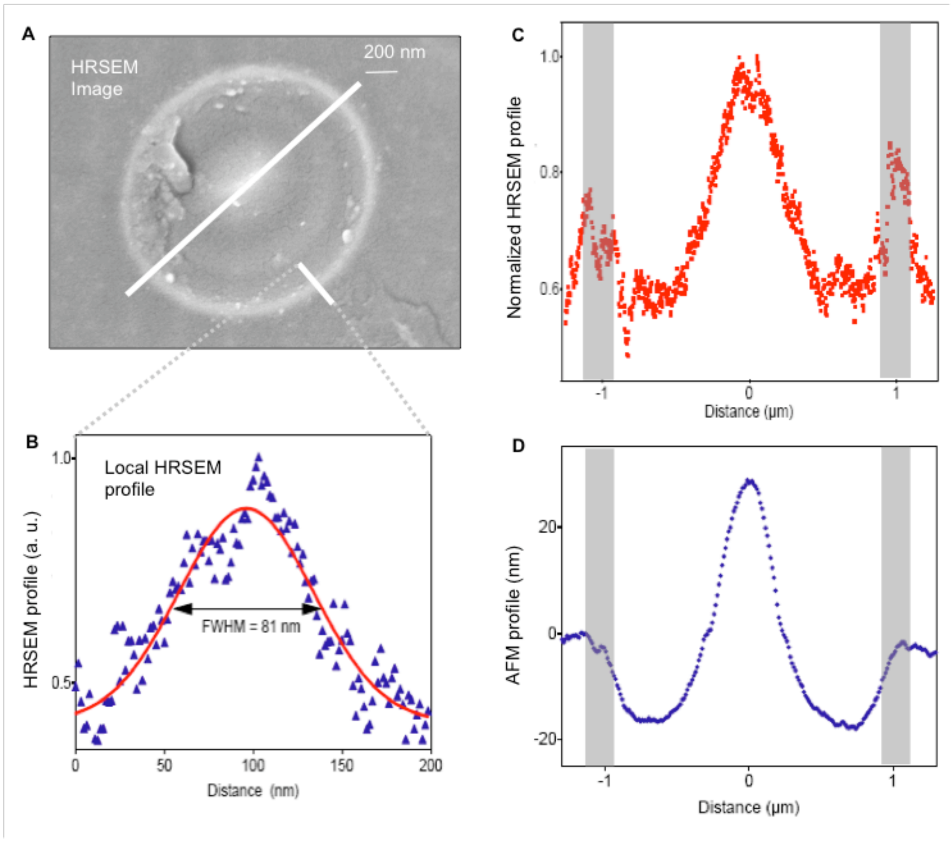

Figure 7.4 HRSEM and AFM characterization of the nanostructures. (a) HRSEM (b) the transversal profile of the rim (c,d) profiles across the ring. From [131]

The formation mechanism is understood as a photo-reduction process via nonlinear absorption generating photo-electrons followed by the aggregation process in the zinc phosphate glass. The unique ring structure results from the photo-dissociation process by the tip of Gaussian beam. Figure 7.5 illustrates this multi-step process to create sub-diffraction limit features via FLDW. The reduction process shown in Figure 7.5 (A) is described as

$$Ag^{+} + e^{-} \rightarrow Ag^{o}, \tag{7.4}$$

Then the process evolves into multiple steps as shown in Eq.(7.5). This leads to the aggregation of silver clusters to form Ag_m^{x+} (m<10) which is a stable chemical form emitting fluorescence around 600 nm for 405 nm excitation.

$$\begin{aligned} &Ag^{0} + Ag^{+} \rightarrow Ag_2^{+}, \\ &Ag_2^{+} + Ag^{+} \rightarrow Ag_3^{2+}, \\ &Ag_3^{2+} + Ag^{0} \rightarrow Ag_m^{x+}. \end{aligned} \tag{7.5}$$

In step (B) in, Thermal diffusion occurs after a few thousands pulses. The last step Figure 7.5 (C) is a photo-dissociation process, which occurs only at the center of the beam due to the high intensity over the dissociation threshold of the silver clusters.

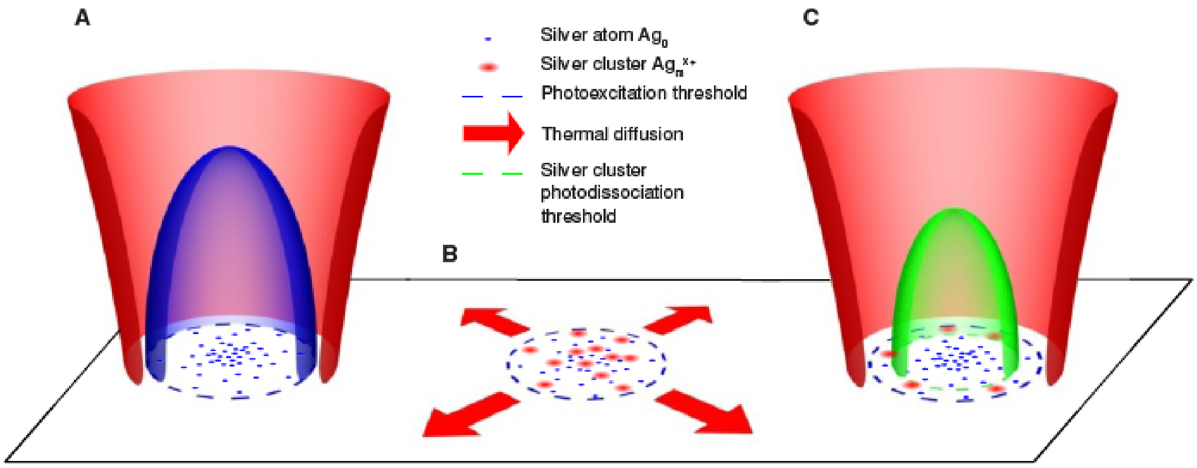

Figure 7.5 Mechanism of the formation of a silver tube. From [131]

7.2.2 Theoretical model of laser-induced depletion

As a consequence, the ring structure has redistributed charges which provide a permanent internal DC field across the wall of the tube. The situation is depicted in Figure 7.6. Because of the intense femtosecond laser irradiation, two most possible identified types of color centers, Ag^{2+} and Ag_m^{x+}, which play as hole trap and electron trap respectively, are generated. They are indicated as blue and red dot lines respectively in the picture. With the process described in previous section, Ag_m^{x+} clusters are rich at the rim of the silver structures. As illustrated, the permanent electric field, which is depicted as black arrows, is formed between Ag^{2+} and Ag_m^{x+}.

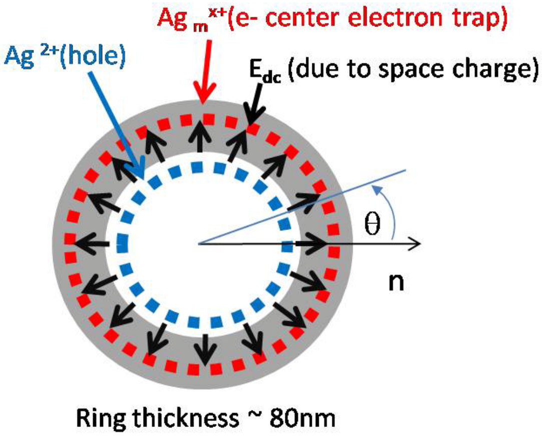

Figure 7.6 Femtosecond laser induced depletion. White arrows indicate the direction of the permanent electric field between Ag^{2+} and Ag_m^{x+}

The induced polarization in the structure is represented as decomposed forms in n and y in Eq. (7.6). [36]

$$\begin{aligned} P_n(2\omega) &= 3\chi^{(3)}_{nnnn}(E_{dc}\cos\theta)E^2_{probe} \\ P_y(2\omega) &= 3\chi^{(3)}_{yynn}(E_{dc}\sin\theta)E^2_{probe} \end{aligned}, \tag{7.6}$$

7.2.3 Second harmonic generation of silver ion containing glass

The second-order of susceptibility can be induced by the interplay of third-order susceptibility and the internal electric field. Thus, second harmonic generation measurement with the laser written structure was tested to explore the existence of second-order susceptibility. Figure 7.7 is the SHG microscopy setup attached to the direct writing station. A femtosecond laser was used as a writing beam to form the silver structure and also used as a probe beam with reduced power.

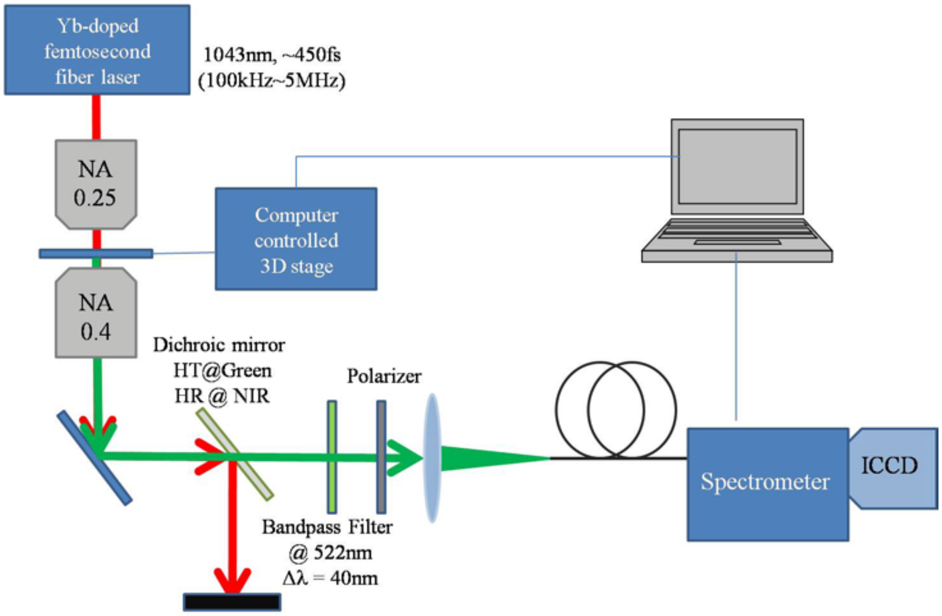

Figure 7.7 SHG measurement setup

The SHG signal was collected by a 0.4 NA objective lens, then delivered into the double monochrometer with an intensified CCD camera (ICCD) as a detector. The fundamental wavelength was rejected by a dichroic mirror. Any possible fluorescence near 600nm by multi-photon excitation was blocked by a bandpass filter at 520nm with 40nm bandwidth. Figure 7.8(a) and (b) show the SHG signal distribution of the silver micro-structures in zinc phosphate and a piece of z-cut quartz respectively imaged by a CCD beam profiler. As is inferred from Figure 7.4 and Figure 4.20, an annular SHG distribution of silver clusters is seen. It is interesting to compare the distribution with the signal from quartz, which is taken at the same probe intensity[10]. The latter shows the same profile with the probe beam which is a Gaussian beam distribution.

---

[10] ND filters were used for quartz to attenuate the SHG intensity (attenuation 99.77%) .

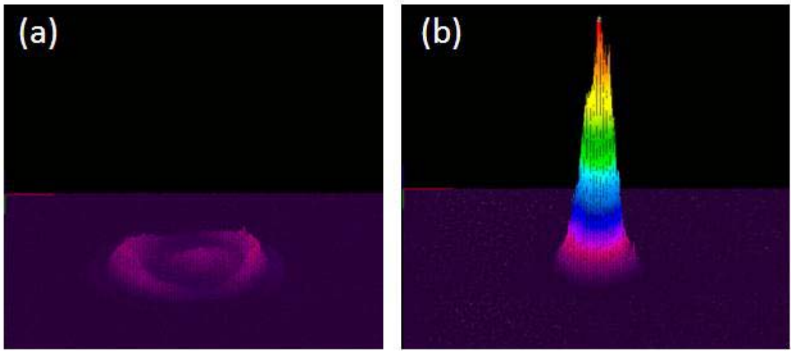

Figure 7.8 3-D SHG profile of (a) silver tube and (b) quartz

Since quartz is an intrinsic second-order nonlinear optical material, the maximum intensity of the SHG is found at the intensity peak of the input beam as illustrated in Figure 7.9. In the silver cluster ring, the nonlinear region is located only at the rim of the structure since the internal electric field only exists in this region. The maximum SHG can also be found at the rim of the structure.

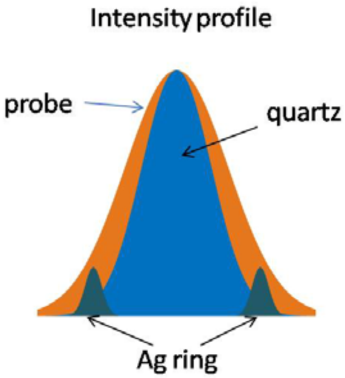

Figure 7.9 Schematic diagram of the convolution of the SHG of the silver ring and quartz with pump beam

Figure 7.10(a,c) shows the SHG from a micro-structure and quartz respectively measured by an intensified CCD detector. The center wavelength is located at ~522 nm, which is half of the fundamental wavelength, so it confirms that the signal is the second harmonic of the probe beam. The FWHM bandwidth of the SHG signal is about ~1.4 nm, which is smaller than the bandwidth of the fundamental laser of ~7.5 nm. Figure 7.10(b,d) is the SHG as a function of probe intensity.

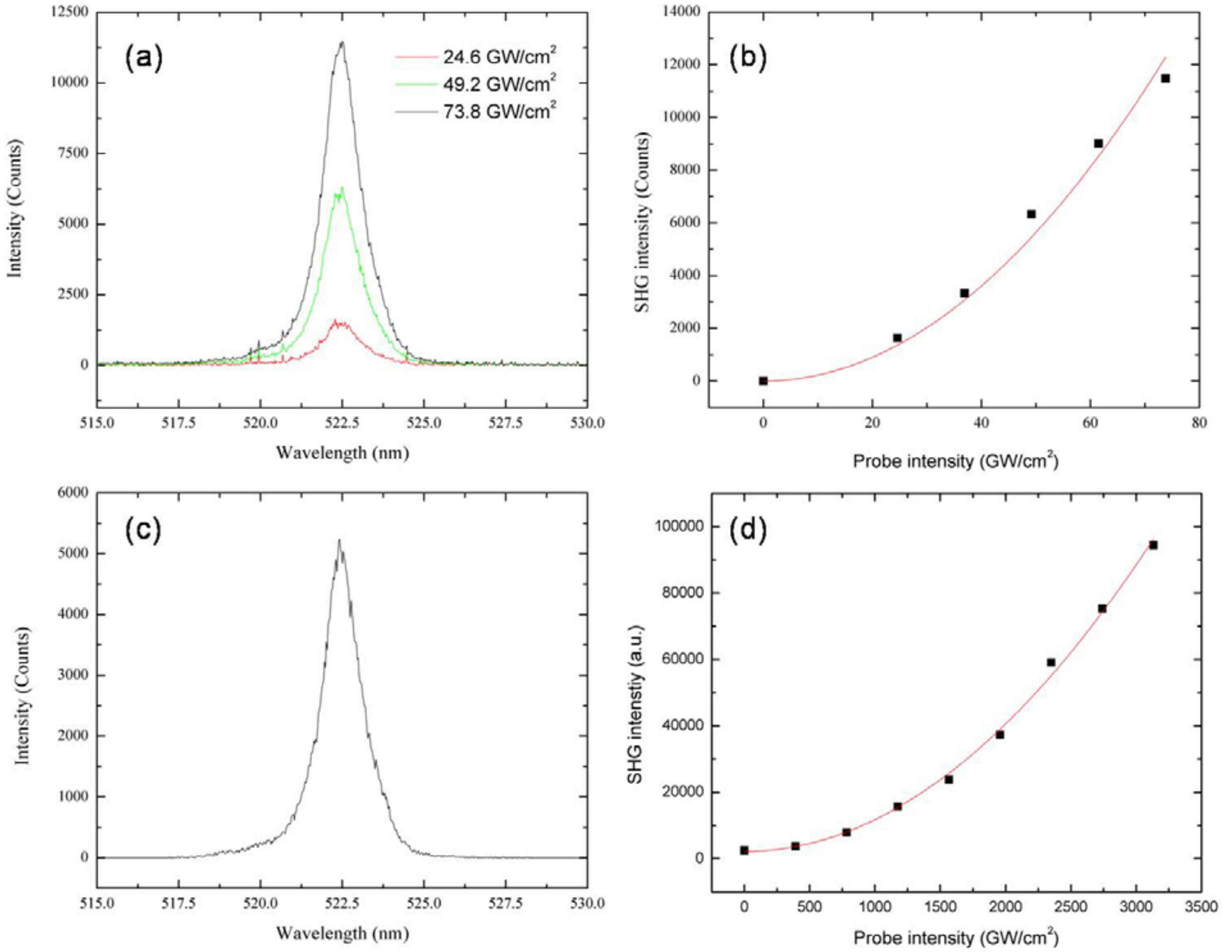

Figure 7.10 (a,b) Measured SHG of a silver tube (b) shows a quadratic relation to the probe beam intensity (c,d) Quartz [11]

The SHG intensity of a micro-structure was compared to the SHG intensity of quartz to estimate the SHG efficiency of the structure. To normalize the gained signal from the structure, the same probe intensity was irradiated both on quartz and on the micro-structure using the same

---

[11] Acquisition times are different in zinc phosphate (10s) and in quartz (10ms)

objective lens. The SHG intensity from the silver structure was divided by the SHG intensity of the quartz crystal. In addition, the effective NLO area was taken into account since only the rim of the structure plays as NLO region. Therefore, the area of the ring was applied. The estimated $\chi^{(2)}$ is 2.44, $\chi^{(2)}_{quartz}$ which corresponds to ~ 1.5 pm/V. The laser-induced $\chi^{(2)}$ is comparable to the thermal poling of the similar composition that is reported as 1.8 pm/V [132].

7.2.4 Polarization dependence

Since the internal DC field has a radial direction, it can be decomposed into the horizontal and vertical direction. In Figure 7.11(a-c), near field images of SHG distribution are shown. White and green arrows indicate the polarization of the laser and the direction of an analyzer respectively. In Figure 7.11(a), the raw SHG intensity without an analyzer is shown as a ring. The highest intensity is in the direction of the polarization of the laser. When the direction of the analyzer is aligned with the laser polarization (HH), the signal looks similar to the signal in Figure 7.11(a). When the analyzer is rotated perpendicularly (HV), there is a very weak signal from the other component of the electric field. It is important to note that the intensity at the center is the same regardless of the direction of the analyzer. It is assumed that the signal could be a result from either the unfiltered fundamental beam or from hyper Rayleigh scattering.

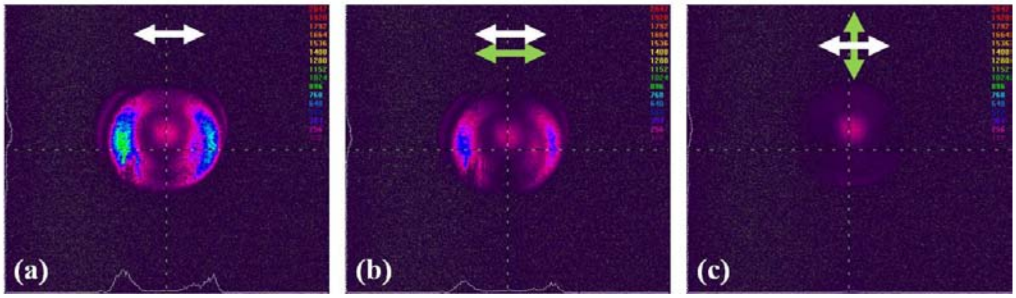

Figure 7.11 Intensity map of the SHG of Ag micro-structure (a) no analyzer, the direction of the analyzer (b) parallel (HH) and (c) perpendicular (HV) to the polarization of the laser

In Figure 7.12, a simulated image of a theoretical model for the horizontal polarization and its experimental result is shown. As is seen in Figure 7.11, both images agree with each other well with the exception of the center signal present in the experimental image. The signal at the center is assumed to be a residue of the peak of the fundamental beam since the signal is not filtered out by the polarizer and does not show the intensity change by the rotation of the polarizer for green wavelength.

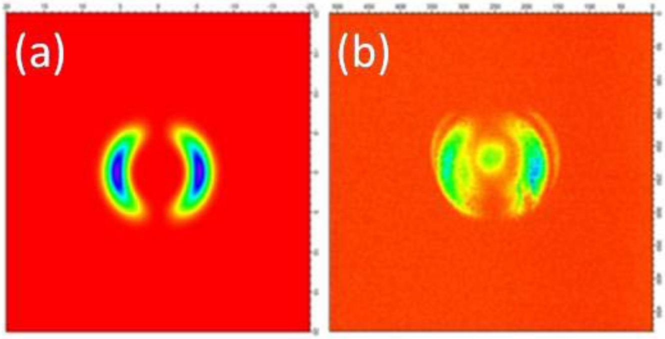

Figure 7.12 SHG distribution at horizontal polarization of probe and analyzer, (a) theoretical (b) experimental

Figure 7.13 is the intensity of the SHG as a function of angle for both polarization orientations. It should be noted that the intensity ratio of HH (horizontal laser polarization and horizontal analyzer) and HV (horizontal for laser polarization and perpendicular analyzer) is about $I_H : I_V = 9:1$. The relationship between the two intensity ratios can be supported because the ratio of corresponding elements in the third-order susceptibility tensors is known as $\chi^{(3)}_{nnnn} : \chi^{(3)}_{yynn} = 3:1$ in glass and thus the intensity ratio is squared.

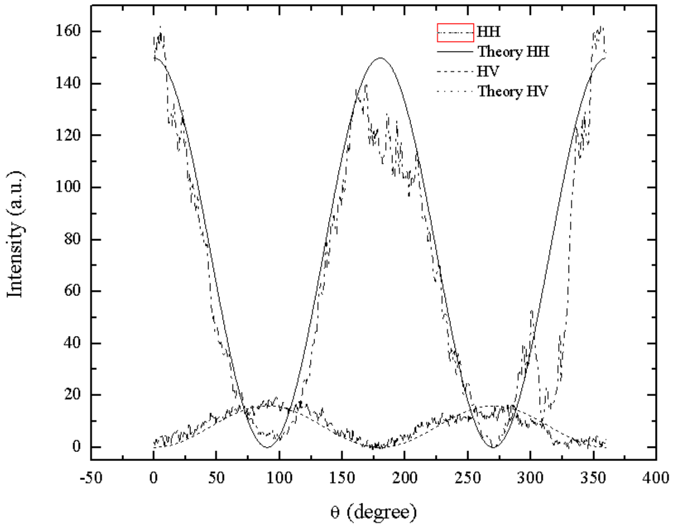

Figure 7.13 Polarization angle dependence of SHG signal

In Figure 7.14, a polar plot of all intensity distributions is shown for both HH and HV configurations as well as the intensity without the analyzer. It is clearly confirmed that the SHG intensity is directional which is determined by the laser polarization.

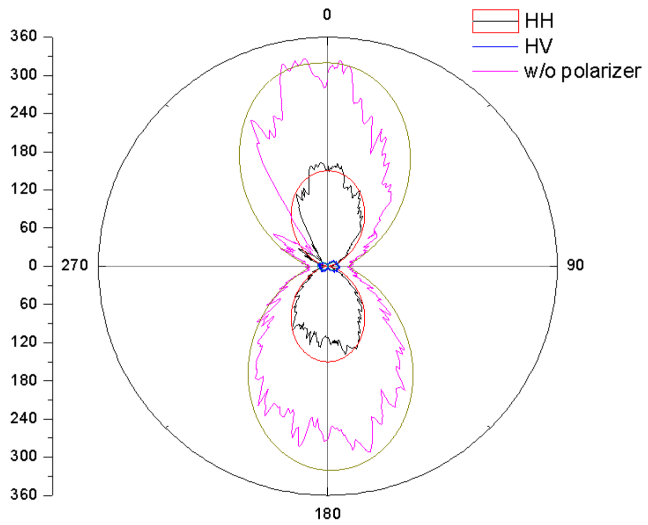

Figure 7.14 SHG intensity plot of HH, HV polarization and without analyzer.

7.2.5 Parametric dependence on fabrication parameters

In order to investigate the parametric dependence of the fabrication factors and material difference, laser repetition rate and numerical aperture were chosen as primary fabrication parameters in zinc phosphate/FOTURAN glasses. FOTURAN glass is a commercially available glass with less than 1% of silver[12][133]. Figure 7.15 shows the SHG intensities of zinc phosphate and FORURAN glass irradiated as a function of probe intensity.

7.2.5.1 focused beam size by different objective lenses

It would be expected that the distribution of the spatial charge can be modified by varying the size of the structure through changing the irradiation beam size. Thus, a laser-induced permanent electric field might be changed due to the variation of ion distribution. This may lead to the enhancement of $\chi^{(2)}$ since $\chi^{(2)}$ is directly proportional to the permanent electric

---

[12] The composition is found in ref [132] as B_2O_3, CeO_2, Sb_2O_3, Ag_2O<1%, K_2O 1–20%, SiO_2 > 80%, Al_2O_3, Na_2O, ZnO, Li_2O 1–10%

field. Two microscope objective lenses (NA=0.25 and 0.4) are used for the investigation. However, there is no significant trend with a small beam size change of a few microns.

7.2.5.2 Material dependence

It should be noted that the difference of the SHG intensity level between zinc phosphate and FOTURAN results not from a single origin but possibly because of several reasons. First, the concentration of the mobile species is different; the silver concentration is 1% for zinc phosphate and <1% for FOTURAN. Secondly, the threshold for color center formation would be different due to the interplay of multi-contents affecting the bandgap of the material. As is shown, the thermal properties, such as the diffusion coefficient, would also differ from phosphate glass and perhaps affect the mobility of nanoparticles. This is supported by Figure 7.15. Higher efficiency is shown for zinc phosphate at high repetition rate (b) whereas similar efficiencies are shown for both glasses at lower repetition rate (a).

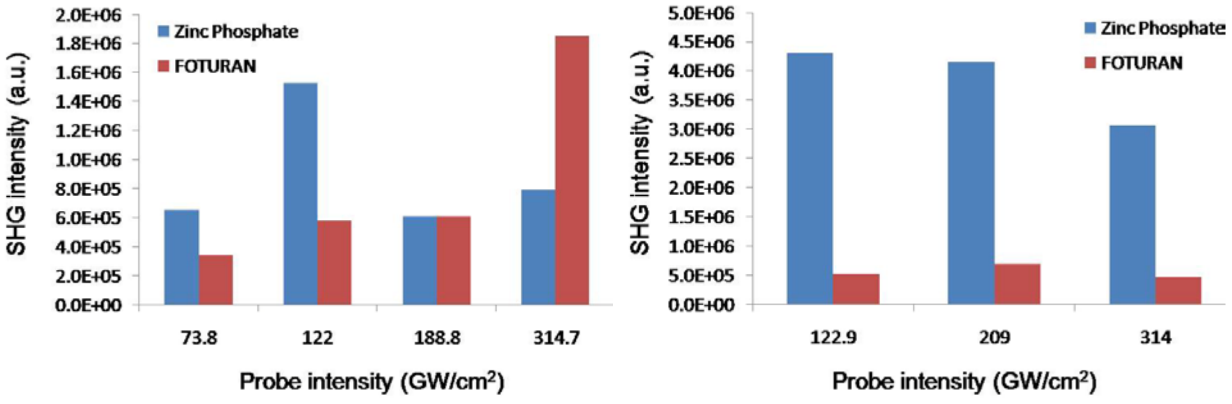

(a) (b)

Figure 7.15 SHG intensity vs. materials at (a) 500 kHz (b) 1500 kHz

7.2.5.3 Laser repetition rate

Figure 7.16 shows the repetition rate dependence of the materials of SHG intensity. As is shown above, zinc phosphate shows higher SHG efficiency than FOTURAN. Furthermore, in Figure 7.16(a), significant enhancement of SHG intensity is shown as the laser repetition rate increases. This would indicate that heat accumulation increases the mobility of clusters leading to the enhanced permanent static electric field.

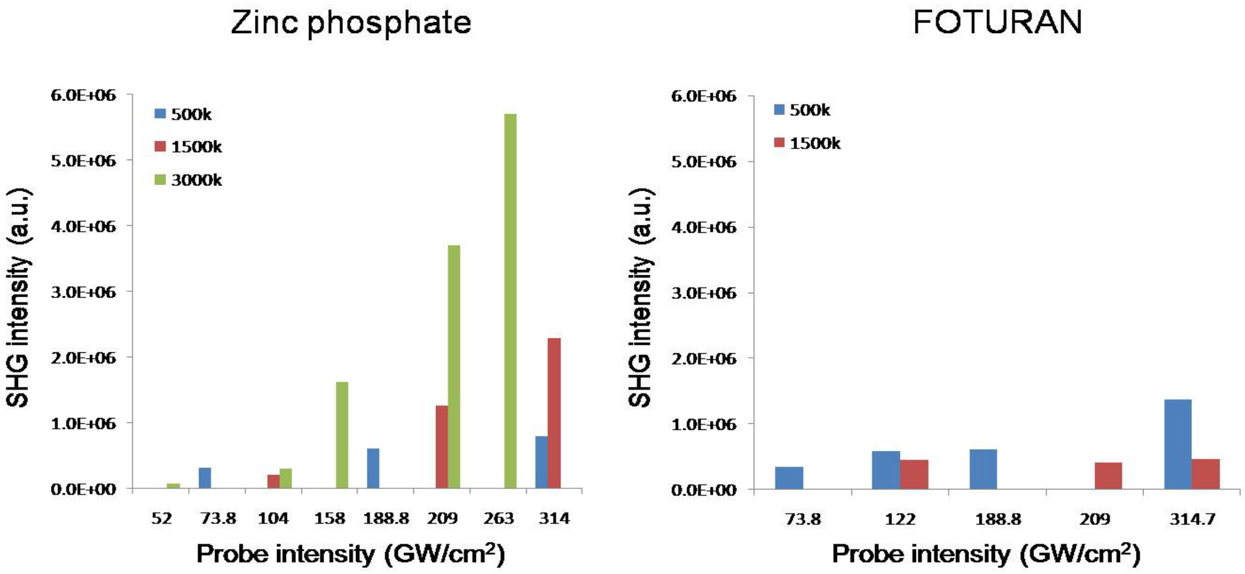

(a) (b)

Figure 7.16 SHG intensity vs. repetition rate and materials as functions of probe intensity (a) zinc phosphate (b) FOTURAN

CHAPTER 8 : RELAXATION OF THE FEMTOSECOND LASER WRITTEN DEVICES

Since its first demonstration with directly-written waveguides in 1996 [7], femtosecond laser direct-writing has been actively adopted in fabricating 3-D photonic devices. However, only a few of thorough investigations have been conducted regarding the reliability and degradation of the performance of the laser-written photonic structures over time and thermal fluctuation. Will et al. demonstrated the characterization of their annealed laser-written waveguide in fused silica [134]. They observed that light guiding properties were not changed by annealing up to 500 °C for a few hours. However, the characteristic fluorescence of laser-induced color centers excited between 560 nm and 630 nm disappeared by annealing at 400 °C. Zhang et al. also reported the annealed Bragg grating waveguide in borosilicate glass and its diffraction efficiency [135]. They observed a serious decrease of grating strength over 250 °C and no guiding over 500 °C. To the best of our knowledge, there is no rigorous investigation on relaxation or degradation properties of the laser-written structure either by heat treatment or time for chalcogenide. Zhang et al. reported the enhancement of n_2 (nonlinear index) in bulk As_2S_3 induced by a femtosecond laser that lasted for 9 months while the reduction of n_2 induced by a cw laser was completely recovered after 4 months [136]. However, they did not carry out a quantitative investigation on this topic. In this chapter, photo-induced structural modification in bulk chalcogenide glasses and corresponding refractive index change is discussed in terms of time and heat treatment conditions. Some ideas for reliability towards the practical use of laser-written structures are discussed as well.

8.1 Relaxation of chalcogenide glass

Chalcogenide glasses (ChGs) have been considered as a candidate for MIR photonic applications due to their wide transparency window in the range from ~0.6 μm to ~16 μm There have been numerous investigations in the fabrication and characterization of femtosecond laser directly-written photonic structures using ChGs [8, 82, 86] Their performances, such as propagation loss and diffraction efficiency, were reported in [137]. However, only limited numbers of investigations have focused on their reliability and thermal issues causing reduction of the performance of the femtosecond laser-written devices. This work used the same composition of bulk ChGs, demonstrated in Chapter 4, to investigate time-involved and annealed glass to show the reliability change of the laser-induced refractive index change in terms of time and thermal treatment.

8.1.1 Fabrication and measurement of test platform

Two different femtosecond laser written structures were made at the surface and in the volume of bulk glasses with the composition $As_{42}S_{58}/As_{36}Sb_6S_{58}/As_{36}Ge_6S_{58}$ in order to investigate the relaxation of the photo-induced structure of the glasses. The first structure is a short line (the length of 200 μm) array written at the surface of the glass as a function of laser dose to monitor the photo-expansion over time and thermal-induced relaxation. The second structure consists of buried linear diffraction gratings formed within the glass samples to estimate the photo-induced refractive index change Δn in bulk. The details of the fabrication are described in Chapter 4. The photo-expansion or diffraction efficiency of each structure was measured using a white light surface profiler and a diffraction efficiency setup consisting of a CW 800 nm Ti:Sapphire laser and a power meter. These results were used as references to normalize the future measurement after 9 months and after annealing. Then, the samples were stored in a desiccator in the dark at room temperature. After 9 months, the same measurements were taken with the structures to compare with the freshly laser-written samples. The samples were then annealed in air for 15 hours at 150°C ($As_{42}S_{58}$ /$As_{36}Ge_6S_{58}$) and at 160°C ($As_{36}Sb_6S_{58}$) depending on the T_g of the glass. Surface photo-expansion and diffraction efficiency were measured after annealing. Micro Raman spectroscopy was performed on the annealed structure to investigate the bond change caused by the heat treatment.

8.1.2 Decrease of photo-expansion

Figure 8.1 shows the photo-expansion of freshly irradiated, 9 months old, and annealed (a) $As_{42}S_{58}$ (b) $As_{36}Sb_6S_{58}$ (c) $As_{36}Ge_6S_{58}$ as a function of inverse writing speed which is proportional to the laser dose. They are normalized with the highest photo-expansion of each composition. It is shown that 10 ~ 25 % of relaxation occurs after 9 months, 27 ~ 56% after annealing with respect to the 9 months (32 ~ 65% from freshly irradiated sample). It is noted that although the 3 investigated glasses show reduction from their initial photo-expansion, there is a difference between compositions. The introduction of Sb in the As-S network shows the largest reduction of the photo-expansion after 9 months while the addition of Ge in a similar network shows the least reduction at the highest laser dose over time. It is assumed due to the 3-D network of Ge containing ChG to be resistant to relaxation at room temperature. The decrease is more pronounced in the glass with the composition $As_{36}Sb_6S_{58}$. This is attributed to the less constrained glass network.

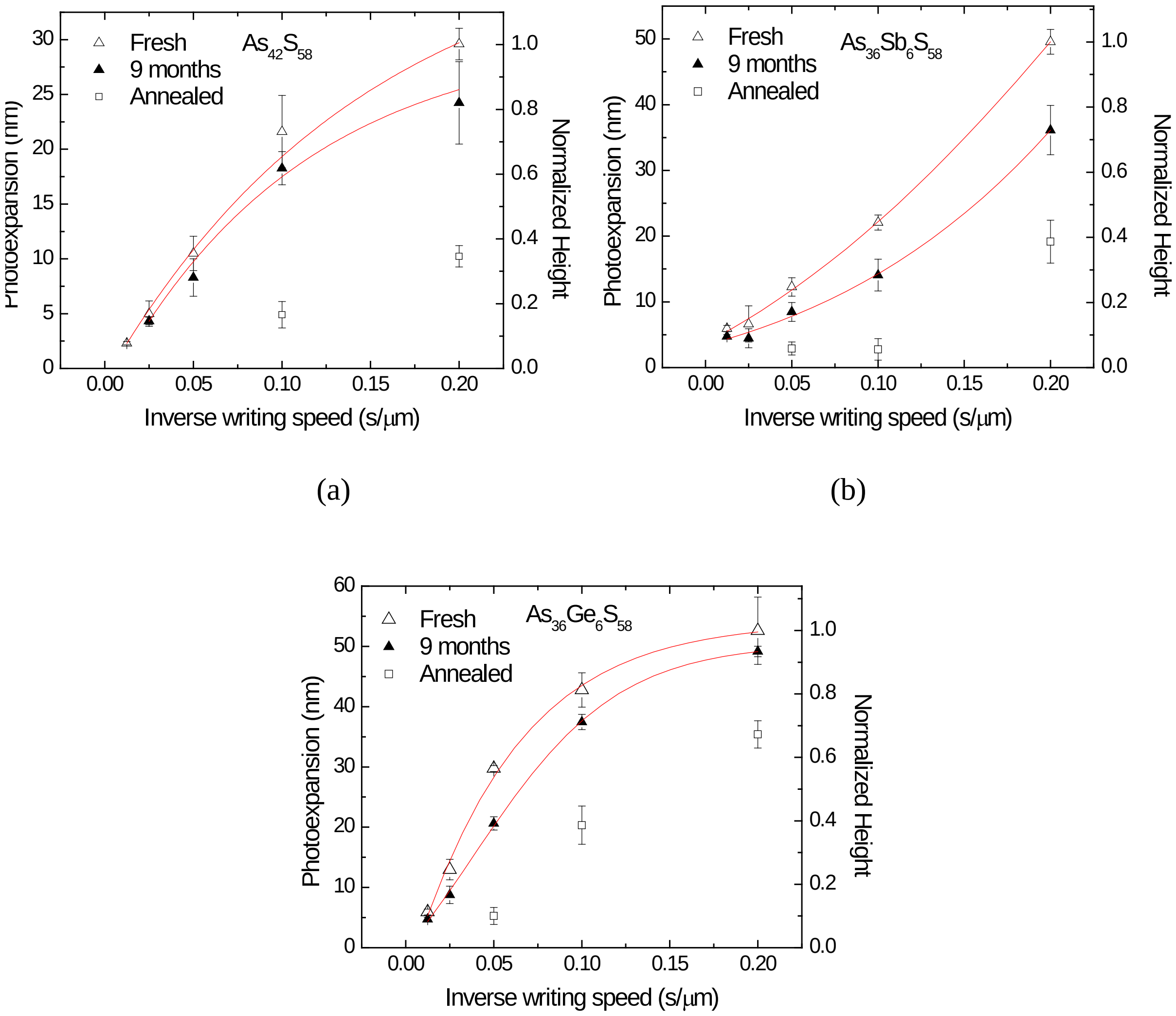

(a)

(b)

(c)

Figure 8.1 Photo-expansion of ChGs after irradiation, after 9 months and after annealing

After the heat treatment, the decrease of photo-expansion for all compositions is even more drastically changed. The two photo-expanded lines completely disappeared and were barely seen using a white light surface profilometer. The glass with the composition $As_{36}Ge_6S_{58}$ exhibits the smallest decrease in photo-expansion amplitude which is consistent with the result above.

Figure 8.2 shows the corresponding Raman spectra of three compositions after annealing. The comparison of the Raman shift between fresh and irradiated samples was discussed in Chapter 4. The micro Raman spectra of the annealed sample were acquired at the blank region and at the photo-expansions written by the first and second highest doses, corresponding to the inverse writing speeds of 0.1 and 0.2 s/μm shown in Figure 8.1. Intensity changes due to the irradiation are found in the regions from 200 to 250 cm^{-1} for all compositions, but not in the region from 450 to 500 cm^{-1}, except $As_{42}S_{58.}$ The band was shown for all compositions after irradiation in Figure 4.18. The black arrows in Figure 8.2 indicate the effect of laser irradiation. In the spectra of $As_{36}Sb_6S_{58}$ and $As_{36}Ge_6S_{58}$, variation of the amplitude of the band located near 360 cm^{-1} is also seen. In addition, a new peak is found after annealing in 200 to 250 cm^{-1} for $As_{42}S_{58}$. The narrow band width of the new peak is suspected to be evidence of partial crystallization. To compare these spectra with Figure 4.18, it is noticed that the laser-induced change in the range of 200 to 250 cm^{-1} and 450 to 500 cm^{-1} seems diminished after annealing, but is not completely reversible as the corresponding photo-expansion still remains as seen in Figure 8.1.

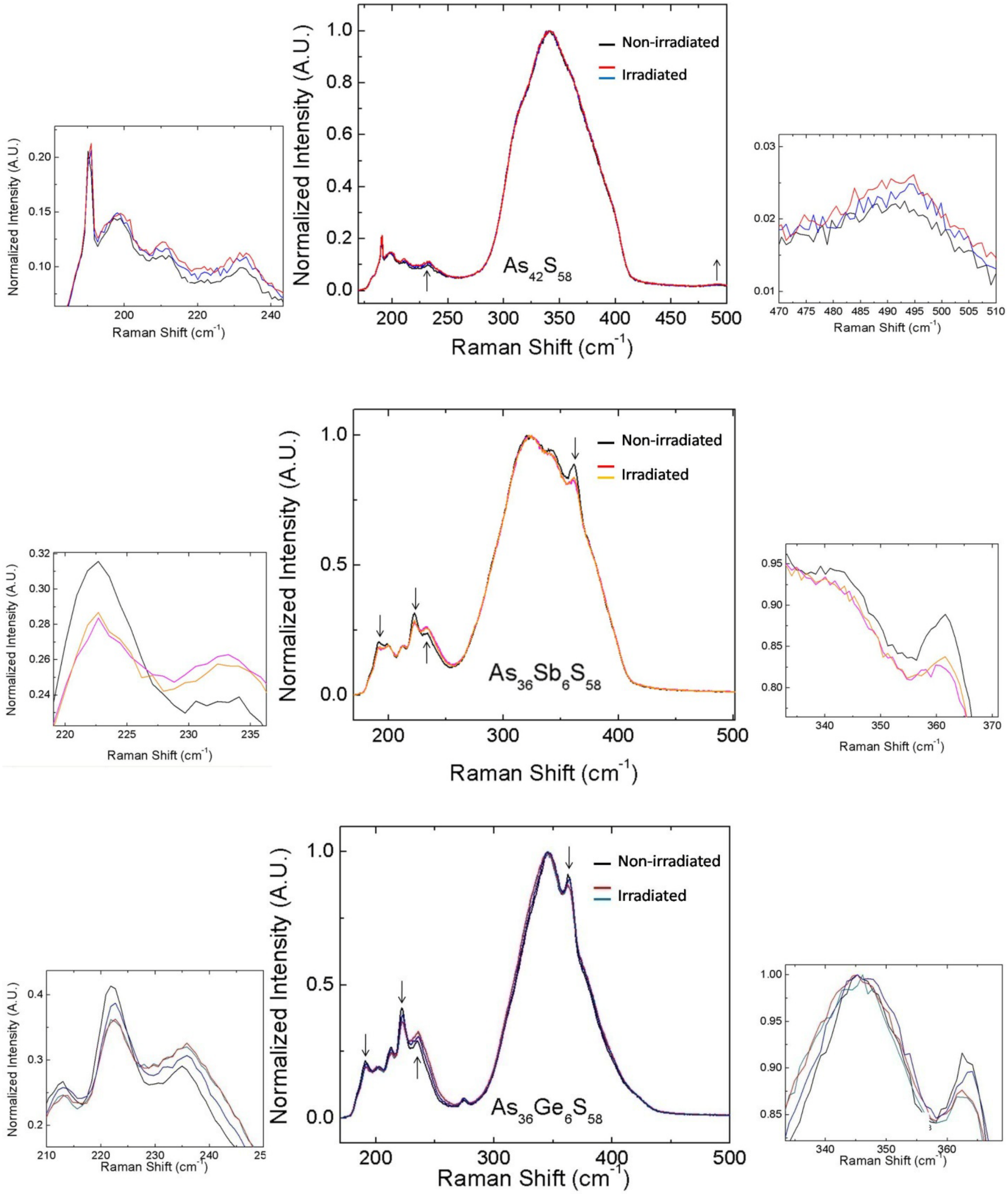

Figure 8.2 Raman shift of irradiated and non-irradiated $As_{42}S_{58}$, $As_{36}Sb_6S_{58}$ and $As_{36}Ge_6S_{58}$ after annealing

8.1.3 Decrease of photo-induced refractive index change

As explained in the previous chapter, the calculated Δn is proportional to the laser dose, which leads to proportional surface photo-expansion[82, 86]. Therefore, the decrease of photo-expansion may imply the decrease of Δn as well. The Δn after 9 months and after annealing was measured to justify the assumption. Figure 8.3 shows the result of Δn measurement of $As_{42}S_{58}$ before and after 9 months. As expected, the decrease of Δn is shown with the reduction of ~10%. After annealing, the diffraction power at the 1^{st} order was smaller than a measurable range. Thus, it was not possible to detect any Δn. For the other compositions, unexpected defects, which distorted the input laser beam, were generated within the samples. Therefore, the diffraction powers were not able to be measured. However, the origin of the generation of defect is unclear.

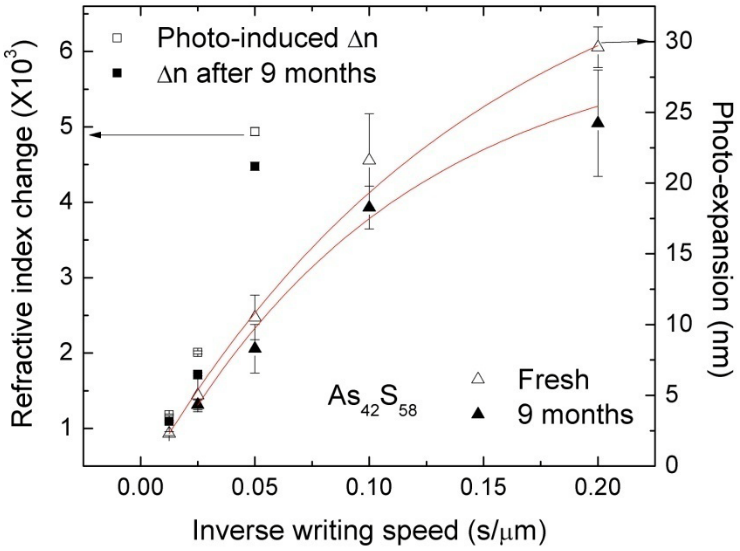

Figure 8.3 Photo-induced expansion and refractive index change of bulk $As_{42}S_{58}$ after irradiation and after 9 months

8.1.4 Reduction of the photo-induced structure by heat treatment

In the previous section, the photo-expansion and corresponding Δn was measured for the overall change due to the combination of aging and annealing. Although Δn of an embedded structure was shown to be proportional to photo-expansion, the linear correlation between two dimensional and three dimensional change is uncertain. Thus, the change of embedded photo-induced structure by heat treatment is measured separately to investigate the sole change via thermal effect in the bulk. Several embedded gratings were inscribed in bulk $As_{36}Sb_6S_{58}$ with various laser doses and intensities. The annealing was carried out immediately after irradiation. The annealing parameters were the same as the previous experiment, for 15 hours at 160°C (T_g - 40°C) in an air environment. Figure 8.4 (top) and (bottom) show the optical microscopic images of the gratings written in the $As_{36}Sb_6S_{58}$ with the dose of 11.1 kJ/cm^2 for Figure 8.4(a) and 5.6 kJ/cm^2 for (b) under the same intensity of ~ 53.7 GW/ cm^2, respectively prior to and after annealing. After annealing, the structures were shrunk about 36% and 34% with respect to the initial lengths for Figure 8.4 (a) and (b) respectively.

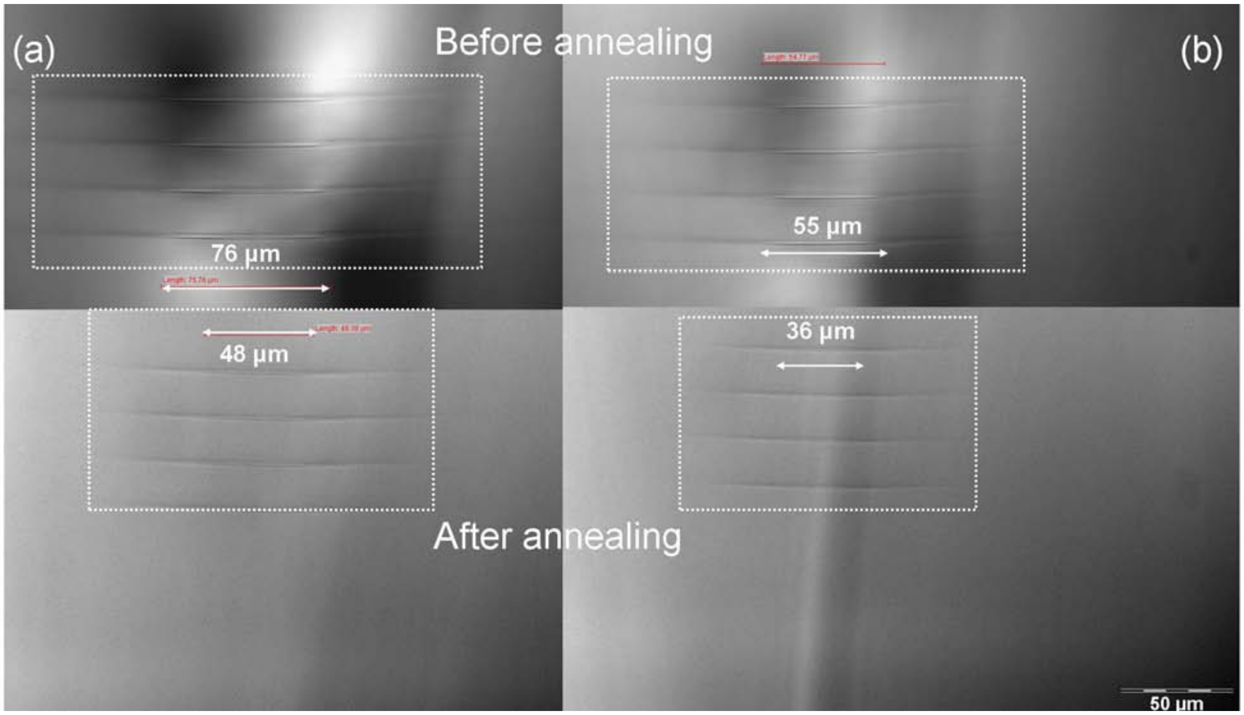

Figure 8.4 Optical microscopic image of the photo- expansion change of bulk $As_{36}Sb_6S_{58}$ before and after annealing for 15 hours at 160 °C in air environment

In order to clarify the relation of dose and intensity dependence on relaxation, various laser doses and intensities were applied. Figure 8.5 shows the DIC optical microscopic image of embedded gratings created using various laser doses prior to and after annealing. The modified region is clearly seen in Figure 8.5 (a, b) while the region is distinguishable but not significant in Figure 8.5 (c, d) compared to (a, b). The former is thought to be at the start of the saturation process. It is interesting to note that the relaxation behavior is also different in both cases. The annealed structures are shown in Figure 8.5 (a-d). It seems that the modification shown in (a, b) is more resistant to annealing than (c, d). Micro Raman spectroscopy and a near-field refractive index measurement may distinguish the difference between both modifications for chemical and optical properties.

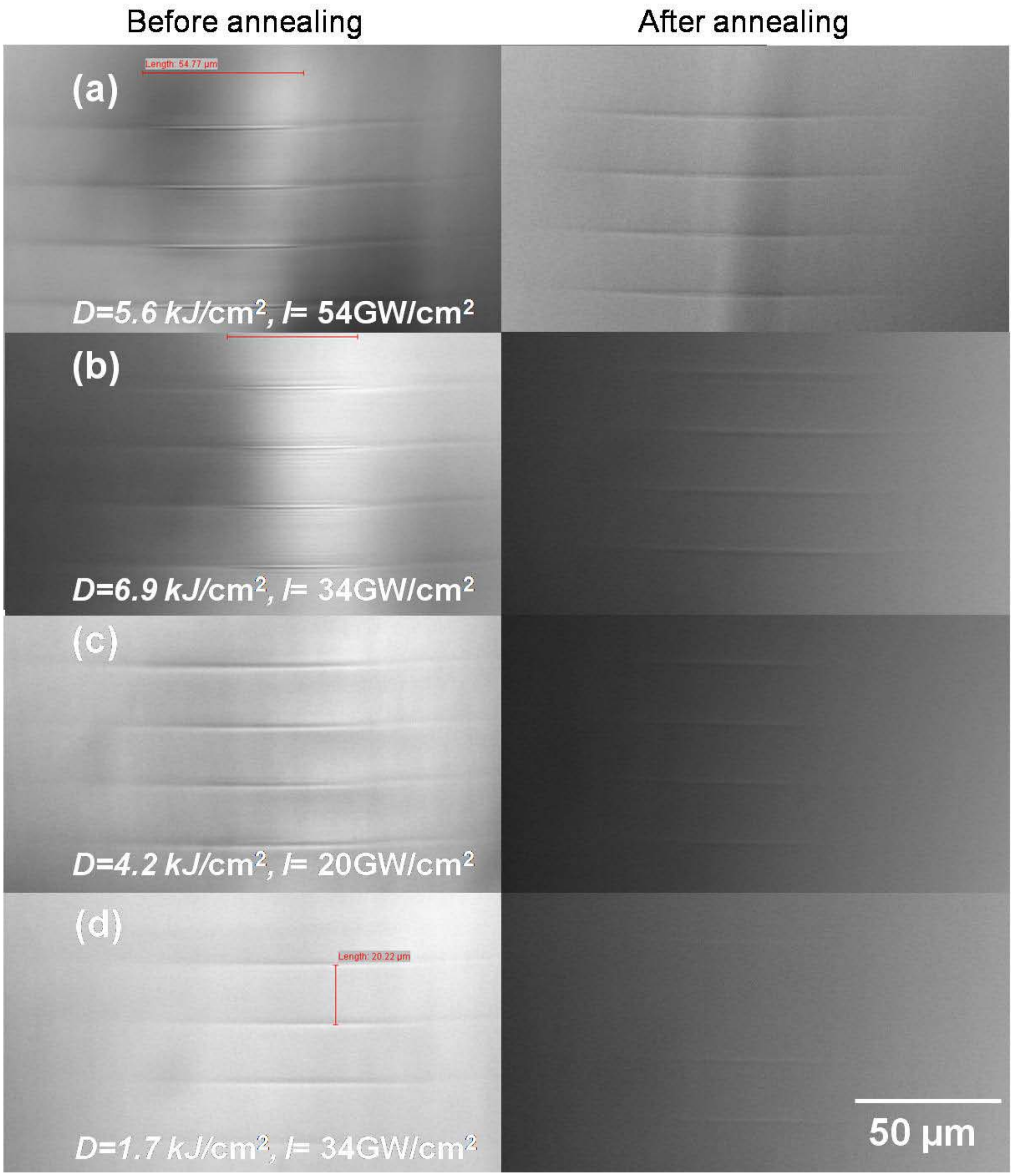

Figure 8.5 Optical microscopic image of the photo-expansion change produced at various dose and intensity in bulk $As_{36}Sb_6S_{58}$ before and after annealing for 15 hours at 160 °C in an air environment

CHAPTER 9 : CONCLUSIONS AND PERSPECTIVES

Increasing demands for a variety of integrated, on-chip photonic devices have stimulated researchers to work on customized photonic devices that can be used in micro-sensors, micro-fluidic on-chip devices, and photonic circuits. Femtosecond laser direct-writing has been a promising technique in meeting these demands, as it enables the production of truly 3D volumetric photonic structures embedded in transparent optical materials such as fused silica, photosensitive glasses, and metal ion-containing glass. Despite the extensive investigations that have been done on FLDW, however, the potential for its applications has not been fully explored. This dissertation was an attempt to make an improvement on the existing FLDW technique to achieve a reliable fabrication protocol for integrated optical devices involving micro diffractive optical elements, such as Fresnel zone plates and volumetric gratings.

As the first step toward the goal is to find appropriate optical materials and to know their photo-responses, various novel materials were investigated—which include chalcogenide, tellurite, silver ion-containing zinc phosphate glasses. The ablation thresholds of the given materials were measured as well as their unique photo-responses such as photo-expansion and photo-reduction/photo-dissociation. These were discussed in Chapter 4.

Next, the fabrication parameters of Fresnel zone plates were systematically investigated to maximize their diffraction efficiency by optimizing fabrication parameters, and it was found that a high repetition rate in the range of a few hundred kHz with low NA objective was useful for maximizing the diffraction efficiency. These were discussed in Chapter 5.

Then, various types of integrating directly-written structures were characterized. A directly written embedded multiplex FZP was produced in borosilicate glass—the first of its kind, to the best of our knowledge. This device was found to provide 11.5% diffraction efficiency at the primary focus and perform as a 1 × 4 focused beam splitter. Then, this multiplex FZP was integrated with a waveguide array so that all-optically written integrated structures consisting of a coupling lens and a waveguide array were realized in borosilicate glass.

In addition, a SHG in laser-structured silver containing zinc phosphate (P_2O_5-Ag_2O-Ga_2O_3-ZnO) by "laser depletion" was demonstrated, as an analogy to the depletion in thermal poled glass—this, too, is the first of its kind to the best of our knowledge. The silver microstructures were formed via a three-step process (photo-reduction, diffusion and photo-dissociation) by femtosecond laser pulses at high repetition rate, which can increase local temperature in a voxel due to the heat accumulation. Ag^{2+} as a hole trap and Ag_m^{x+} (m<10) as an e- trap were two bases formed during the process to generate the permanent electric field due to the charge separation across the ring. The distribution of silver clusters, Ag_m^{x+} (m<10) was investigated via high resolution microscopy and photoluminescence study. Interestingly, the formed clusters were shaped as ring structures depending upon the focused beam size. The nonlinear region was the same as the rim of the ring structure. Therefore, the SHG signal was only found at the rim. It showed polarization-dependent SHG distribution, which implied that the induced polarization, defined by the second-order susceptibility in the material, obeys different tensor elements. It was also revealed that laser depletion is enhanced by a higher repetition rate, which implies it is governed by a thermal effect. In addition, the material differences also exhibited different SHG efficiencies, which means that laser depletion can be described as functions of the concentration of mobile ions, T_g of the glass, color-center generation threshold, and repetition rate of the writing laser and other chemical and optical properties of the glass. Extended investigation such as XPS and EDS could be carried out to measure the distribution of mobile ions and clusters formed by different irradiation parameters so that the origin of the permanent DC field can be clarified.

Finally, the relaxation of directly-written structures in bulk chalcogenide glass ($As_{42}S_{58}$ /$As_{36}Sb_6S_{58}$ /$As_{36}Ge_6S_{58}$) was studied by measuring the surface photo-expansion as well as the diffraction efficiency of embedded gratings after irradiation, after 9 months, and after heat treatment. It was found that relaxation occurred in all compositions but the amounts of relaxation were slightly different among the compositions. The samples showed 10 ~ 25 % of relaxation after 9 months and 27 ~ 56% after annealing with respect to the 9 months (32 ~ 65% from freshly irradiated sample). Ge containing bulk chalcogenide showed the highest resistance against relaxation while As containing glass exhibited the lowest durability. This is attributed to the 3D network of the glass matrix involving Ge atoms. The sole change of embedded 3D photo-induced modification only due to the heat treatment was also investigated, and it was found that there were two types of modifications depending upon laser dose and intensity. However, laser dose was considered to be the primary factor of photo-induced modification. Future work could investigate the relationship between chemical and optical properties of embedded 3D photo-induced structural modifications via micro Raman spectroscopy and rigorous near field refractive index mapping. That way, laser-induced 3D modification can be controlled with quantitative fabrication parameters, a crucial factor in fabricating reliable photonic devices utilizing chalcogenide glasses owing to the embedded 3D structures.

APPENDIX A : THERMO-PHYSICAL PROPERTIES OF OPTICAL MATERIALS

Table A.1 Thermal coefficients of selected optical materials[13] (From [42])

	κ [W/cmK]	ρ [g/cm^3]	c_p [J/gK]	D [cm^2/s]
Ag	4.28	10.5	0.23	1.72
Al	2.37	2.7	0.90	1.03
Cu	4.0 (273)	8.94	0.39	1.14
Stainless steel (304)	0.15	8.03	0.5	0.04
a-Si	0.018	2.32	0.8	0.0097
c-Si	1.5	2.32	0.71	0.85
Water (H2O)	0.06	1	4.18	0.014
Glass (Crown)	0.01	2.4	0.89	0.0058
Glass (BK7)	0.011	2.51	0.86	0.0052
$LiNbO_3$	0.042	4.46	0.64	0.015
PI (Kapton)	0.0012	1.42	1.09	0.0008
PMMA	0.0020	1.18	1.41	0.0011
a-SiO_2	0.014	2.2	0.72	0.009
SiO_2	0.014	2.5	0.74	0.0086
TiO_2 (rutile)	0.089 (273)	4.26	0.93	0.031 (273)

---

[13] If temperature is not specified in parentheses, all values refer to T~300K

APPENDIX B : ABSORPTION PROCESS CONSISTING OF THE NONLINEAR ABSORPTION WITH WEAK LINEAR ABSORPTION

When the laser beam with a frequency of ω is propagating a medium with no gain, the intensity I(z) of the laser beam propagating in z direction in a medium is described as

$$\frac{dI(z)}{dz} = -\alpha_o(\omega)I - \beta(\omega)I^2 - \gamma(\omega)I^3 - \cdots \ , \tag{B.1}$$

where α_o is the linear (or single photon) absorption coefficient, given as $\alpha_o = {2\kappa\omega}/{c}$ (κ is the extinction coefficient of the medium), β and γ are the two- and three-photon absorption coefficients respectively. Therefore, the absorption process involving n photons is proportional to the intensity to the nth power of the incident laser beam. If the medium exhibits absorption in the range of the laser frequency ω, the linear absorption process is the dominant excitation mechanism which promotes a bound electron to the conduction band. Thus Eq. (B.1) is approximated as

$$\frac{dI(z)}{dz} = -\alpha_o(\omega)I \ . \tag{B.2}$$

In transparent materials where the linear absorption is not present in the range of incident laser frequency ($\alpha_o \approx 0$ at ω), nonlinear absorption processes are dominant. Here, single photon excitation does not take place. For two-photon absorption [138], the Eq. (B.1) is then reduced as

$$\frac{dI(z)}{dz} = -\beta(\omega)I^2 . \tag{B.3}$$

Two photon absorption coefficient β is given as $\beta = \frac{3\omega}{2n_0^2 c^2 \varepsilon_0}\chi_{\mathrm{Im}}^{(3)}$, where $\chi_{\mathrm{Im}}^{(3)}$ is the imaginary part of the third-order susceptibility. The solution of the Eq. (B.3) is obtained as

$$I(z) = \frac{I(0)}{1+\beta I(0)z} . \tag{B.4}$$

When linear absorption is small, but not negligible ($\alpha_o << 1$ at ω), the differential equation in Eq. (B.1) for two photon absorption is modified as

$$\frac{dI(z)}{dz} = -\alpha_o(\omega)I - \beta(\omega)I^2. \tag{B.5}$$

The solution of the equation is then described as,

$$I(z) = \frac{I(0)e^{-\alpha_0 z}}{1 + \frac{\beta}{\alpha_0} I(0)(1 - e^{-\alpha_0 z})}. \tag{B.6}$$

The two-photon absorption process is affected by the linear absorption process, thus the contribution of two-photon absorption in terms of the generation of free electron is dependent on the depth of the medium where the laser beam is focused.

APPENDIX C : PHOTO-INDUCED REFRACTIVE INDEX CHANGE IN $\mathbf{As_{0.42-x-y}Ge_xSb_yS_{0.58}}$ AND THE EFFECT OF MEAN POLARIZABILITY CHANGE

The number of bond N involving an atom K in a voxel of the femtosecond laser irradiation is described as [86]

$$N_K = \zeta K_{at\%} \frac{N_A \rho}{M} V \ . \tag{C.1}$$

$K_{At\%}$ is the atomic fraction of atom K (At%), which represents the atom of interest in the bulk glass, ζ indicates the ζ –fold coordination of atom K, N_A is Avogadro's number, ρ and M is the density and the molecular weight of the bulk ChG glasses respectively, V is the volume of a voxel, which is estimated as $V \approx 2\pi w_0^2 z_0$. ρ and M for $As_{42}S_{58}$, $As_{36}Ge_6S_{58}$ and $As_{36}Sb_6S_{58}$ is 3.20, 3.15, 3.40 g/cm^3 and 50.06, 49.92, 52.87 g/mol respectively. The volume of a voxel produced by an objective with NA=0.25 is estimated as 1.54×10^{-10} cm^3. Therefore, the numbers of As-S bond within a voxel in $As_{42}S_{58}$ is estimated to be 6.88×10^{12} cm^{-3} and either As-S or Ge-S (Sb-S) in $As_{36}Ge_6S_{58}$ ($As_{36}Sb_6S_{58}$) are 6.79×10^{12} (6.92×10^{12}) cm^{-3} respectively using the fraction of S (0.58)[14].

The mean polarizability of the material is described by Lorentz-Lorenz equation

$$\frac{n_0^2 - 1}{n_0^2 + 2} = \frac{4\pi}{3} \frac{N_A \rho}{M} \alpha \ . \tag{C.2}$$

where n_o and α is the refractive index and the mean polarizability of the material. α in $As_{42}S_{58}$ (n_o = 2.468 at 800 nm) , $As_{36}Ge_6S_{58}$ (n_o = 2.364 at 800 nm) and $As_{36}Sb_6S_{58}$ (n_o = 2.541 at 800 nm) are estimated using Eq. (C.2) to be 3.90×10^{-24}, 3.80×10^{-24}, 3.98×10^{-24} cm^3 respectively.

Photo-expansion and photo-induced index change (Δn_o) due to the femtosecond laser irradiation result from the decrease of the density ρ and the increase of the refractive index n_o in

---

[14] From a micro-Raman study shown in Figure 4.18, the presence of not only As-S, but also the different type of bonds such as As-As, As-Sb and Sb-Sb are seen before laser irradiation.

the given bulk ChG glasses. Thus, the re-calculation of Eq. (C.2) with $\rho+\Delta\rho$ and $n_o+\Delta n_o$ may provide information on the photo-induced mean polarizability change. $\Delta(\rho\alpha)$, the difference of the product of the density and the mean polarizability, is calculated using Δn_o provided from the measurement shown in Figure 4.21. $\Delta(\rho\alpha)$ in $As_{42}S_{58}$, $As_{36}Ge_6S_{58}$ and $As_{36}Sb_6S_{58}$ after fs pulse exposure using the similar laser dose (~ 10 kJ/cm^2) is obtained as 0.12%, 0.20% and 0.05% respectively. However, the photo-expansion measured from the irradiated surface of the bulk ChGs, which is shown in Figure 4.17, provides only 2-D information of the expansion, whereas the photo-induced Δn was measured using an embedded grating in the bulk, which resulted from 3-D photo-expansion. Therefore, it is not able to determine the mean polarizability change $\Delta\alpha$ separately from $\Delta(\rho\alpha)$ without measuring $\Delta\rho$ three dimensionally.

To conclude, the femtosecond laser-induced structural changes represented as photo-expansion and photo-induced refractive index change may result from the change of either the density or the mean polarizability, which is due to the increase of the number of homo polar bonds. However, it is not clear that the photo-induced refractive change can be directly linked to the photo-expansion and is proportional to the photo-expansion. Further studies such as selective etching followed by HRSEM imaging may be required to measure 3-D photo-expansion in bulk ChG glasses to estimate $\Delta\rho$ separately.

LIST OF REFERENCES

[1] S. Sinzinger and J. Jahns, "Integrated micro-optical imaging system with a high interconnection capacity fabricated in planar optics," Appl. Opt., vol. 36, pp. 4729-4735, 1997.

[2] Y. Wang, W. Yun, and C. Jacobsen, "Achromatic Fresnel optics for wideband extreme-ultraviolet and X-ray imaging," Nature, vol. 424, pp. 50–53, 2003.

[3] Y. S. Chu, J. M. Yi, F. De Carlo, Q. Shen, W. K. Lee, H. J. Wu, C. L. Wang, J. Y. Wang, C. J. Liu, and C. H. Wang, "Hard-x-ray microscopy with Fresnel zone plates reaches 40 nm Rayleigh resolution," Appl. Phys. Lett., vol. 92, p. 103119, 2008.

[4] K. Hedsten, J. Melin, J. Bengtsson, P. Modh, D. Karlén, B. Löfving, R. Nilsson, H. Rödjegård, K. Persson, and P. Enoksson, "MEMS-based VCSEL beam steering using replicated polymer diffractive lens," Sensors & Actuators: A. Physical, vol. 142, pp. 336-345, 2008.

[5] J. Fonollosa, R. Rubio, S. Hartwig, S. Marco, J. Santander, L. Fonseca, J. Wöllenstein, and M. Moreno, "Design and fabrication of silicon-based mid infrared multi-lenses for gas sensing applications," Sensors & Actuators: B. Chemical, vol. 132, pp. 498-507, 2008.

[6] Y. Kuroiwa, N. Takeshima, Y. Narita, S. Tanaka, and K. Hirao, "Arbitrary micropatterning method in femtosecond laser microprocessing using diffractive optical elements," Appl. Phys. Lett., vol. 12, 2004.

[7] K. M. Davis, K. Miura, N. Sugimoto, and K. Hirao, "Writing waveguides in glass with a femtosecond laser," Opt. Lett., vol. 21, pp. 1729-1731, 1996.

[8] K. Miura, J. Qiu, H. Inouye, T. Mitsuyu, and K. Hirao, "Photowritten optical waveguides in various glasses with ultrashort pulse laser," Appl. Phys. Lett., vol. 71, pp. 3329-3331, 1997.

[9] S. Nolte, M. Will, J. Burghoff, and a. Tünnermann, "Femtosecond waveguide writing: a new avenue to three-dimensional integrated optics," Appl. Phys. A, vol. 77, pp. 109-111, 2003.

[10] R. Osellame, S. Taccheo, M. Marangoni, R. Ramponi, P. Laporta, D. Polli, S. De Silvestri, and G. Cerullo, "Femtosecond writing of active optical waveguides with astigmatically shaped beams," J. Opt. Soc. Am. B, vol. 20, pp. 1559-1567, 2003.

[11] S. Taccheo, G. Della Valle, R. Osellame, G. Cerullo, N. Chiodo, P. Laporta, O. Svelto, A. Killi, U. Morgner, and M. Lederer, "Er: Yb-doped waveguide laser fabricated by femtosecond laser pulses," Opt. Lett., vol. 29, pp. 2626-2628, 2004.

[12] A. M. Streltsov and N. F. Borrelli, "Fabrication and analysis of a directional coupler written in glass by nanojoule femtosecond laser pulses," Opt. Lett, vol. 26, pp. 42-43, 2001.

[13] K. Minoshima, A. M. Kowalevicz, I. Hartl, E. P. Ippen, and J. G. Fujimoto, "Photonic device fabrication in glass by use of nonlinear materials processing with a femtosecond laser oscillator," Opt. Lett., vol. 26, pp. 1516-1518, 2001.

[14] S. Katayama, M. Horiike, K. Hirao, and N. Tsutsumi, "Diffraction measurement of grating structure induced by irradiation of femtosecond laser pulse in acrylate block copolymers," Jpn. J. Appl. Phys., vol. 41, pp. 2155-2162, 2002.

[15] Y. Kondo, K. Nouchi, T. Mitsuyu, M. Watanabe, P. G. Kazansky, and K. Hirao, "Fabrication of long-period fiber gratings by focused irradiation of infrared femtosecond laser pulses," Opt. Lett, vol. 24, pp. 646-648, 1999.

[16] P. J. Scully, D. Jones, and D. A. Jaroszynski, "Femtosecond laser irradiation of polymethylmethacrylate for refractive index gratings," Journal of Optics A: Pure and Applied Optics, vol. 5, pp. S92-S96, 2003.

[17] A. Martinez, M. Dubov, I. Khrushchev, and I. Bennion, "Direct writing of bre Bragg gratings by femtosecond laser," Electron. Lett, vol. 40, pp. 31-32, 2004.

[18] H. Zhang, S. M. Eaton, J. Li, and P. R. Herman, "Femtosecond laser direct writing of multiwavelength Bragg grating waveguides in glass," Opt. Lett., vol. 31, pp. 3495-3497, 2006.

[19] H. Zhang, S. M. Eaton, and P. R. Herman, "Single-step writing of Bragg grating waveguides in fused silica with an externally modulated femtosecond fiber laser," Opt. Lett., vol. 32, pp. 2559-2561, 2007.

[20] W. Watanabe, D. Kuroda, K. Itoh, and J. Nishii, "Fabrication of Fresnel zone plate embedded in silica glass by femtosecond laser pulses," Opt. Express, vol. 10, pp. 978-983, 2002.

[21] K. Yamada, W. Watanabe, Y. Li, K. Itoh, and J. Nishii, "Multilevel phase-type diffractive lenses in silica glass induced by filamentation of femtosecond laser pulses," Optics Letters, vol. 29, pp. 1846-1848, 2004.

[22] E. Bricchi, J. D. Mills, P. G. Kazansky, B. G. Klappauf, and J. J. Baumberg, "Birefringent Fresnel zone plates in silica fabricated by femtosecond laser machining," Opt. Lett, vol. 27, pp. 2200-2202, 2002.

[23] P. Srisungsitthisunti, O. K. Ersoy, and X. Xu, "Volume Fresnel zone plates fabricated by femtosecond laser direct writing," Appl. Phys. Lett., vol. 90, p. 011104, 2007.

[24] A. Szameit, F. Dreisow, H. Hartung, S. Nolte, A. Tünnermann, and F. Lederer, "Quasi-incoherent propagation in waveguide arrays," Appl. Phys. Lett., vol. 90, p. 241113, 2007.

[25] A. Szameit, H. Hartung, F. Dreisow, S. Nolte, and A. Tünnermann, "Multi-waveguide excitation in fs laser written waveguide arrays," Appl. Phys.Lett., 2006.

[26] S. Nolte, C. Momma, H. Jacobs, A. Tünnermann, B. N. Chichkov, B. Wellegehausen, and H. Welling, "Ablation of metals by ultrashort laser pulses," J. Opt. Soc. Am. B, vol. 14, pp. 2716 - 2722, 1997.

[27] Q. Sun, H. Jiang, Y. Liu, Z. Wu, H. Yang, and Q. Gong, "Measurement of the collision time of dense electronic plasma induced by a femtosecond laser in fused silica," Opt. Lett., vol. 30, pp. 320-322, 2005.

[28] H. Misawa and S. Juodkazis, 3D Laser Microfabrication: Principles and Applications: Wiley-VCH, 2006.

[29] B. Rethfeld, K. Sokolowski-Tinten, D. Von Der Linde, and S. I. Anisimov, "Timescales in the response of materials to femtosecond laser excitation," Applied Physics A: Materials Science & Processing, vol. 79, pp. 767-769, 2004.

[30] E. G. Gamaly, A. V. Rode, B. Luther-Davies, and V. T. Tikhonchuk, "Ablation of solids by femtosecond lasers: Ablation mechanism and ablation thresholds for metals and dielectrics," Physics of plasmas, vol. 9, p. 949, 2002.

[31] L. Jiang and H. L. Tsai, "Improved two-temperature model and its application in ultrashort laser heating of metal films," Journal of Heat Transfer, vol. 127, p. 1167, 2005.

[32] B. C. Stuart, M. D. Feit, A. M. Rubenchik, B. W. Shore, and M. D. Perry, "Laser-Induced Damage in Dielectrics with Nanosecond to Subpicosecond Pulses," Phys. Rev. Lett., vol. 74, pp. 2248-2251, 1995.

[33] D. Du, X. Liu, G. Korn, J. Squier, and G. Mourou, "Laser-induced breakdown by impact ionization in SiO with pulse widths from 7 ns to 150 fs," Appl. Phys. Lett., vol. 64, p. 3071, 1994.

[34] B. C. Stuart, M. D. Feit, S. Herman, A. M. Rubenchik, B. W. Shore, and M. D. Perry, "Nanosecond-to-femtosecond laser-induced breakdown in dielectrics," Phys. Rev. B, vol. 53, pp. 1749-1761, 1996.

[35] C. B. Schaffer, "Interaction of femtosecond laser pulses with transparent materials," Harvard University, 2001.

[36] R. W. Boyd, Nonlinear Optics: Academic Press, 2008.

[37] X. Liu, D. Du, and G. Mourou, "Laser ablation and micromachining with ultrashort laser pulses," Quantum Electronics, IEEE Journal of, vol. 33, pp. 1706-1716, 1997.

[38] D. Batani, Atoms, solids, and plasmas in super-intense laser fields: Kluwer Academic/Plenum Publishers New York, 2001.

[39] P. Braunlich, G. Brost, A. Schmid, and P. Kelly, "The role of laser-induced primary defect formation in optical breakdown of NaCl," IEEE Journal of Quantum Electronics, vol. 17, pp. 2034–2041, 1981.

[40] P. Kelly, S. Jones, X. Shen, L. Simpson, P. Braunlich, and R. Casper, "Measurement of the three-photon-absorption cross section and intrinsic optical breakdown of KI at 532 nm," Phys. Rev. B, vol. 42, pp. 11370-11372, 1990.

[41] L. V. Keldysh, "Ionization in the field of a strong electromagnetic wave(Multiphonon absorption processes and ionization probability for atoms and solids in strong electromagnetic field)," ZHURNAL EKSPERIMENTAL'NOI I TEORETICHESKOI FIZIKI, vol. 47, pp. 1945-1957, 1964.

[42] D. Bauerle, Laser processing and chemistry: Springer, 2000.

[43] C. B. Schaffer, J. F. Garc, and E. Mazur, "Bulk heating of transparent materials using a high-repetition-rate femtosecond laser," Appl. Phys. A, vol. 76, pp. 351-354, 2003.

[44] C. B. Schaffer, A. Brodeur, J. F. Garcia, and E. Mazur, "Micromachining bulk glass by use of femtosecond laser pulses with nanojoule energy," Opt. Lett, vol. 26, pp. 93-95, 2001.

[45] R. R. Gattass, L. R. Cerami, and E. Mazur, "Micromachining of bulk glass with bursts of femtosecond laser pulses at variable repetition rates," Opt. Express, vol. 14, pp. 351-354, 2006.

[46] S. Eaton, H. Zhang, P. Herman, F. Yoshino, L. Shah, J. Bovatsek, and A. Arai, "Heat accumulation effects in femtosecond laser-written waveguides with variable repetition rate," Opt. Express, vol. 13, pp. 4708-4716, 2005.

[47] A. Zoubir, "Towards direct writing of 3D-Photonic circuits using ultrafast lasers," in School of Optics. vol. Ph.D Orlando: University of Central Florida, 2004.

[48] D. M. Karnakis, J. Fieret, P. T. Rumsby, and M. C. Gower, "Microhole drilling using reshaped pulsed Gaussian laser beams," in Proc. SPIE 2001, pp. 150-158.

[49] C. Abbott, R. Allott, B. Bann, K. Boehlen, M. Gower, P. Rumsby, I. Stassen-Boehlen, and N. Sykes, "New techniques for laser micromachining MEMS devices," in Proc. SPIE, 2002, p. 281.

[50] R. Osellame, S. Taccheo, M. Marangoni, R. Ramponi, P. Laporta, D. Polli, S. De Silvestri, and G. Cerullo, "Femtosecond writing of active optical waveguides with astigmatically shaped beams," J. Opt. Soc. Am. B, vol. 20, pp. 1559-1567, 2003.

[51] M. Ams, G. D. Marshall, D. J. Spence, and M. J. Withford, "Slit beam shaping method for femtosecond laser direct-write fabrication of symmetric waveguides in bulk glasses," Opt. Express, vol. 13, pp. 2626-2628, 2005.

[52] D. Zeng, W. P. Latham, and A. Kar, "Shaping of annular laser intensity profiles and their thermal effects for optical trepanning," Opt. Eng., vol. 45, pp. 014301-014301, 2006.

[53] Z. Jaroszewicz, A. Burvall, and A. T. Friberg, "Axicon - the Most Important Optical Element," Optics & Photonics News, 2005.

[54] S. Juodkazis and H. Misawa, "Forming tiny 3D structures for micro-and nanofluidics," SPIE Newsroom, DOI, vol. 10, p. 0510, 2007.

[55] T. Kondo, S. Matsuo, S. Juodkazis, V. Mizeikis, and H. Misawa, "Multiphoton fabrication of periodic structures by multibeam interference of femtosecond pulses," Appl. Phys. Lett., vol. 82, p. 2758, 2003.

[56] T. Kondo, S. Matsuo, S. Juodkazis, and H. Misawa, "Femtosecond laser interference technique with diffractive beam splitter for fabrication of three-dimensional photonic crystals," Appl. Phys. Lett., vol. 79, p. 725, 2001.

[57] S. Juodkazis, T. Kondo, H. Misawa, A. Rode, M. Samoc, and B. Luther-Davies, "Photo-structuring of As 2 S 3 glass by femtosecond irradiation," Opt. Express, vol. 14, pp. 683 - 685, 2006.

[58] K.-i. Kawamura, N. Sarukura, M. Hirano, and H. Hosono, "Holographic encoding of fine-pitched micrograting structures in amorphous SiO[sub 2] thin films on silicon by a single femtosecond laser pulse," Appl. Phys. Lett., vol. 78, p. 1038, 2001.

[59] K.-i. Kawamura, M. Hirano, T. Kamiya, and H. Hosono, "Holographic writing of volume-type microgratings in silica glass by a single chirped laser pulse," Appl. Phys. Lett., vol. 81, p. 1137, 2002.

[60] P. R. Herman, R. Marjoribanks, and A. Oettl, "Burst-ultrafast laser machining method," USPTO, Ed. USA, 2003.

[61] C. Dille, P. Kaifosh, P. Forrester, A. G. Mordovanakis, L. Lilge, and R. Marjoribanks, "Ablation of Hard Dental Tissue Using Ultrashort Pulsetrain-Burst (> 100MHz) Laser," in Conference on Lasers and Electro-Optics/, 2009, p. JThE67.

[62] C. Dille, P. Kaifosh, P. Forrester, R. Marjoribanks, and L. Lilge, "Ablation of Dental Hard Tissue with an Ultrashort Pulsetrain-Burst (> 100MHz) Laser," in Laser Science XXIV, 2008, p. JSuA12.

[63] C. W. Siders, J. L. W. Siders, A. J. Taylor, S. G. Park, and A. M. Weiner, "Efficient high-energy pulse-train generation using a 2^ n-pulse Michelson interferometer," Appl. Opt., vol. 37, 1998.

[64] C. W. Siders, M. Richardson, N. Vorobiev, T. Ohlmstead, R. Bernath, and T. Shih, "Burst-mode femtosecond ablation in copper and lexan," 2003, p. 2.

[65] J. Choi, R. Bernath, M. Ramme, and M. Richardson, "Increase of ablation rate using burst mode femtosecond pulses," in Proc CLEO/QELS, Baltimore, MD, USA, 2007, p. JThD101.

[66] L. Canioni, M. Bellec, A. Royon, B. Bousquet, and T. Cardinal, "Three-dimensional optical data storage using third-harmonic generation in silver zinc phosphate glass," Opt. Lett., vol. 33, pp. 360-362, 2008.

[67] R. R. Gattass, "Femtosecond-laser interactions with transparent materials: applications in micromachining and supercontinuum generation," Harvard university, 2006.

[68] R. Osellame, N. Chiodo, G. Della Valle, S. Taccheo, R. Ramponi, G. Cerullo, A. Killi, U. Morgner, M. Lederer, and D. Kopf, "Optical waveguide writing with a diode-pumped femtosecond oscillator," Optics Letters, vol. 29, pp. 1900-1902, 2004.

[69] R. Osellame, S. Taccheo, M. Marangoni, R. Ramponi, P. Laporta, D. Polli, S. De Silvestri, and G. Cerullo, "Femtosecond writing of active optical waveguides with astigmatically shaped beams," Journal of the Optical Society of America B, vol. 20, pp. 1559-1567, 2003.

[70] K. C. Vishnubhatla, N. Bellini, R. Ramponi, G. Cerullo, and R. Osellame, "Shape control of microchannels fabricated in fused silica by femtosecond laser irradiation and chemical etching," Optics Express, vol. 17, pp. 8685-8695, May 11 2009.

[71] R. M. Vazquez, R. Osellame, D. Nolli, C. Dongre, H. van den Vlekkert, R. Ramponi, M. Pollnau, and G. Cerullo, "Integration of femtosecond laser written optical waveguides in a lab-on-chip," Lab on a Chip, vol. 9, pp. 91-96, 2009.

[72] M. Wakaki, K. Kudo, and T. Shibuya, Physical properties and data of optical materials: CRC, 2007.

[73] M. D. O'Donnell, K. Richardson, R. Stolen, A. B. Seddon, D. Furniss, V. K. Tikhomirov, C. Rivero, M. Ramme, R. Stegeman, G. Stegeman, M. Couzi, and T. Cardinal, "Tellurite and fluorotellurite glasses for fiberoptic raman amplifiers: glass characterization, optical properties, raman gain, preliminary fiberization, and fiber characterization," J. Am. Ceram. Soc., vol. 90, pp. 1448-1457, 2007.

[74] C. Rivero, K. Richardson, R. Stegeman, G. Stegeman, T. Cardinal, E. Fargin, M. Couzi, and V. Rodriguez, "Quantifying raman gain coefficients in tellurite glasses," J. Non-Cryst. Solids, vol. 345-346, pp. 396-401, 2004.

[75] E. Fargin, A. Berthereau, T. Cardinal, G. Leflem, L. Ducasse, L. Canioni, P. Segonds, L. Sarger, and A. Ducasse, "Optical non-linearity in oxide glasses," J. Non-Cryst. Solids, vol. 203, pp. 96-101, 1996.

[76] G. Vrillet, P. Thomas, V. Couderc, a. Barthelemy, and J. Champarnaudmesjard, "Second harmonic generation in optically poled tellurite glasses doped with heavy metal oxides," J. Non-Cryst. Solids, vol. 345-346, pp. 417-421, 2004.

[77] K. Tanaka, K. Kashima, K. Hirao, N. Soga, A. Mito, and H. Nasu, "Second Harmonic Generation in Poled Tellurite Glasses," Jpn. J. Appl. Phys., vol. 32, pp. L843-L845, 1993.

[78] Y. Yonesaki, K. Tanaka, J. Si, and K. Hirao, "Second-harmonic generation in optically poled tellurite glasses doped with V2O5," J. Phys.: Condens. Matter, vol. 14, pp. 13493-13503, 2002.

[79] B. Ferreira, "Second harmonic generation in poled tellurite glass," J. Non-Cryst. Solids, vol. 332, pp. 207-218, 2003.

[80] Y. Shimotsuma, K. Hirao, J. Qiu, and K. Miura, "Nanofabrication in transparent materials with a femtosecond pulse laser," J. Non-Cryst. Solids, vol. 352, pp. 646-656, 2006.

[81] H. Hisakuni and K. Tanaka, "Giant photoexpansion in As 2 S 3 glass," Applied Physics, vol. 65, pp. 2925-2927, 1994.

[82] A. Zoubir, M. Richardson, C. Rivero, A. Schulte, C. Lopez, K. Richardson, N. Ho, and R. Vallee, "Direct femtosecond laser writing of waveguides in As2S3 thin films," Opt. Lett., vol. 29, pp. 748-750, 2004.

[83] L. Petit, J. Choi, T. Anderson, R. Villeneuve, J. Massera, N. Carlie, M. Couzi, M. Richardson, and K. C. Richardson, "Effect of Ga and Se addition on the "near-surface" photo-response of new Ge-based chalcogenide glasses under IR femtosecond laser exposure," Opt. Mater., vol. 31, pp. 965-969, 2009.

[84] L. Petit, N. Carlie, T. Anderson, M. Couzi, J. Choi, M. Richardson, and K. C. Richardson, "Effect of IR femtosecond laser irradiation on the structure of new sulfo-selenide glasses," Opt. Mater., vol. 29, pp. 1075-1083, 2007.

[85] L. L. Petit, N. N. Carlie, T. T. Anderson, J. J. Choi, M. M. Richardson, and K. K. C. Richardson, "Progress on the Photoresponse of Chalcogenide Glasses and Films to Near-Infrared Femtosecond Laser Irradiation: A Review," Selected Topics in Quantum Electronics, IEEE Journal of, vol. 14, pp. 1323-1334, 2008.

[86] T. Anderson, L. Petit, N. Carlie, J. Choi, J. Hu, A. M. Agarwal, L. C. Kimerling, K. Richardson, and M. Richardson, "Femtosecond laser photo-response of Ge23Sb7S70 films," Opt. Express, vol. 16, pp. 20081–20098, 2008.

[87] J. Hu, X. Sun, A. M. Agarwal, J. F. Viens, L. C. Kimerling, L. Petit, N. Carlie, K. C. Richardson, T. Anderson, and J. Choi, "Studies on structural, electrical, and optical properties of Cu doped As-Se-Te chalcogenide glasses," Journal of Applied Physics, vol. 101, p. 063520, 2007.

[88] L. Petit, N. Carlie, T. Anderson, J. Choi, C. Maurel, M. Couzi, T. Cardinal, M. Richardson, and K. Richardson, "Engineering of glasses for advanced optical applications," The 58th Southeast Regional Meeting, pp. 34604-34604, 2007.

[89] Y. Hamanaka, K. Fukuta, a. Nakamura, L. M. Liz-Marzán, and P. Mulvaney, "Enhancement of third-order nonlinear optical susceptibilities in silica-capped Au nanoparticle films with very high concentrations," Appl. Phys. Lett., vol. 84, p. 4938, 2004.

[90] F. Hache, D. Ricard, and C. Flytzanis, "Optical nonlinearities of small metal particles: surface-mediated resonance and quantum size effects," J. Opt. Soc. Am. B, vol. 3, p. 1647, 1986.

[91] D. Ricard, "Surface-mediated enhancement of optical phase conjugation in metal colloids," Opt. Lett., vol. 10, pp. 511-513, 1985.

[92] M. Dubiel and G. Mosel, "Extended X-Ray Absorption Fine Structure Investigations at the Silver K-Edge of Ion Exchanged Sodium Silicate Glasses," Jpn. J. Appl. Phys, vol. 33, pp. 5892-5893, 1994.

[93] F. Gonella, G. Mattei, P. Mazzoldi, C. Sada, G. Battaglin, and E. Cattaruzza, "Au-Cu alloy nanoclusters in silica formed by ion implantation and annealing in reducing or oxidizing atmosphere," Applied Physics Letters, vol. 75, p. 55, 1999.

[94] H. Hofmeister, S. Thiel, M. Dubiel, and E. Schurig, "Synthesis of nanosized silver particles in ion-exchanged glass by electron beam irradiation," Applied Physics Letters, vol. 70, p. 1694, 1997.

[95] I. Belharouak, C. Parent, B. Tanguy, G. L. Flem, and M. Couzi, "Silver aggregates in photoluminescent phosphate glasses of the 'Ag2O?ZnO?P2O5' system," J. Non-Cryst. Solids, vol. 244, pp. 238-249, 1999.

[96] C. Maurel, T. Cardinal, M. Bellec, L. Canioni, B. Bousquet, M. Treguer, J. J. Videau, J. Choi, and M. Richardson, "Luminescence properties of silver zinc phosphate glasses following different irradiations," J. Lumin., 2009.

[97] D. Huang, E. A. Swanson, C. P. Lin, J. S. Schuman, W. G. Stinson, W. Chang, M. R. Hee, T. Flotte, K. Gregory, and C. A. Puliafito, "Optical coherence tomography," Science, vol. 254, pp. 1178-1181, 1991.

[98] J. A. Izatt, M. R. Hee, G. M. Owen, E. A. Swanson, and J. G. Fujimoto, "Optical coherence microscopy in scattering media," Opt. Lett, vol. 19, pp. 590-592, 1994.

[99] J. Choi, K.-S. Lee, J. P. Rolland, T. Anderson, and M. C. Richardson, "Nondestructive 3-D Imaging of Femtosecond Laser Written Volumetric Structures Using Optical Coherence Microscopy," submitted.

[100] M. Will, S. Nolte, B. N. Chichkov, and A. T?nermann, "Optical properties of waveguides fabricated in fused silica by femtosecond laser pulses," Appl. Opt, vol. 41, p. 4360?364, 2002.

[101] R. Swanepoel, "Determination of the thickness and optical constants of amorphous silicon," Journal of Physics E: Scientific Instruments, vol. 16, pp. 1214-1222, 1983.

[102] H. J. Eichler, P. Gunter, and D. W. Pohl, "Laser induced dynamic gratings (ed.)," Berlin: Springer-Verlag, 1986.

[103] U. Kreibig and M. Vollmer, Optical properties of metal clusters: Springer, 1995.

[104] B. E. A. Salech and M. C. Teich, "Fundamentals of photonics," Willey, NY, 1991.

[105] R. Yokota and H. Imagawa, "ESR Studies of Radiophotoluminescent Centers in Silver-Activated Phosphate Glass," J. Phys. Soc. Jpn., vol. 20, pp. 1537-1538, 1965.

[106] R. Yokota and H. Imagawa, "Radiophotoluminescent Centers in Silver-Activated Phosphate Glass," J. Phys. Soc. Jpn., vol. 23, pp. 1038-1048, 1967.

[107] A. V. Dmitryuk, S. E. Paramzina, A. S. Perminov, N. D. Solov'eva, and N. T. Timofeev, "The influence of glass composition on the properties of silver-doped radiophotoluminescent phosphate glasses," J. Non-Cryst. Solids, vol. 202, pp. 173-177, 1996.

[108] K. Tanaka, "Photoexpansion in As2 S3 glass," Phys. Rev. B, vol. 57, pp. 5163-5167, 1998.

[109] J. Choi, N. Carlie, L. Petit, T. Anderson, K. Richardson, and M. Richardson, "Measurement of Photo-Induced Refractive Index Change in As 0.42-xy Ge x Sb y S 0.58 Bulks Induced by Fs Near IR Laser Exposure," 2007, pp. 100-101.

[110] T. Feldmann and A. Treinin, "Inorganic Radicals Trapped in Glasses at Room Temperature: IV. Silver Radicals in Metaphosphate Glass," J. Chem. Phys., vol. 47, pp. 2754-2754, 1967.

[111] J. Qiu, M. Shirai, T. Nakaya, J. Si, X. Jiang, C. Zhu, and K. Hirao, "Space-selective precipitation of metal nanoparticles inside glasses," Appl. Phys. Lett., vol. 81, pp. 3040-3042, 2002.

[112] S. Qu, J. Qiu, C. Zhao, X. Jiang, H. Zeng, C. Zhu, and K. Hirao, "Metal nanoparticle precipitation in periodic arrays in au[sub 2]o-Doped glass by two interfered femtosecond laser pulses," Appl. Phys. Lett., vol. 84, p. 2046, 2004.

[113] J. W. Chan, T. Huser, S. Risbud, and D. M. Krol, "Structural changes in fused silica after exposure to focused femtosecond laser pulses," Opt. Lett, vol. 26, pp. 1726-1728, 2001.

[114] Q.-D. Chen, D. Wu, L.-G. Niu, J. Wang, X.-F. Lin, H. Xia, and H.-B. Sun, "Phase lenses and mirrors created by laser micronanofabrication via two-Photon photopolymerization," Appl. Phys. Lett., vol. 91, pp. 171105-171105, 2007.

[115] J. K. Kim, J. Kim, K. Oh, I.-B. Sohn, W. Shin, H. Y. Choi, and B. Lee, "Fabrication of Micro Fresnel Zone Plate Lens on a Mode-Expanded Hybrid Optical Fiber Using a Femtosecond Laser Ablation System," in IEEE Photonics Technology Letters, pp. 2008-2010.

[116] O. K. Ersoy, Diffraction, fourier optics, and imaging. Hoboken, N.J.: Wiley-Interscience, 2007.

[117] B. Kress and P. Meyrueis, Digital diffractive optics : an introduction to planar diffractive optics and related technology. Chichester ; New York: John Wiley, 2000.

[118] A. Zoubir, M. Richardson, L. Canioni, A. Brocas, and L. Sarger, "Optical properties of infrared femtosecond laser-modified fused silica and application to waveguide fabrication," J. Opt. Soc. Am. B, vol. 22, pp. 2138-2143, 2005.

[119] S. M. Eaton, H. Zhang, P. R. Herman, F. Yoshino, L. Shah, and A. Y. Arai, "Writing optical waveguides with a 0.1-5MHz repetition rate femtosecond fiber laser," in Conference on Lasers & Electro-Optics (CLEO), pp. 2174-2176.

[120] S. M. Eaton, H. Zhang, M. L. Ng, J. Li, W. J. Chen, S. Ho, and P. R. Herman, "Transition from thermal diffusion to heat accumulation in high repetition rate femtosecond laser writing of buried optical waveguides," Opt. Express, vol. 16, pp. 9443-9458, 2008.

[121] D. Wu, W. Mohammed, P. Srinivasan, E. G. Johnson, L. Qian, and P. W. E. Smith, "Multi-Fiber-Channel, Ultrafast, All-Optical Switch Utilizing a 2D Fresnel Lens Array," in CLEO/QELS, pp. 5-6.

[122] Y. Shi, W. Wang, J. H. Bechtel, a. Chen, S. Garner, S. Kalluri, W. H. Steier, D. Chen, H. R. Fetterman, L. R. Dalton, and L. Yu, "Fabrication and characterization of high-speed polyurethane-disperse red 19 integrated electrooptic modulators for analog system applications," IEEE Journal of Selected Topics in Quantum Electronics, vol. 2, pp. 289-299, 1996.

[123] D. Chen, H. R. Fetterman, A. Chen, W. H. Steier, L. R. Dalton, W. Wang, and Y. Shi, "Demonstration of 110 GHz electro-optic polymer modulators," Appl. Phys. Lett., vol. 70, p. 3335, 1997.

[124] U. Osterberg and W. Margulis, "Dye laser pumped by Nd:YAG laser pulses frequency doubled in a glass optical fiber," Opt. Lett., vol. 11, pp. 516-516, 1986.

[125] R. H. Stolen and H. W. K. Tom, "Self-organized phase-matched harmonic generation in optical fibers," Opt. Lett., vol. 12, pp. 585-585, 1987.

[126] R. A. Myers, N. Mukherjee, and S. R. J. Brueck, "Large second-order nonlinearity in poled fused silica," Opt. Lett, vol. 16, pp. 16-22, 1991.

[127] M. Dussauze, E. Fargin, V. Rodriguez, A. Malakho, and E. Kamitsos, "Enhanced Raman scattering in thermally poled sodium-niobium borophosphate glasses," J. Appl. Phys., vol. 101, pp. 083532-083532, 2007.

[128] P. G. Kazansky, A. R. Smith, P. S. J. Russell, G. M. Yang, and G. M. Sessler, "Thermally poled silica glass: Laser induced pressure pulse probe of charge distribution," Appl. Phys. Lett., vol. 68, pp. 269-269, 1996.

[129] K. Sugioka, Z. Wang, and K. Midorikawa, "3D integration of microfluidics and microoptics inside photosensitive glass by femtosecond laser direct writing for photonic biosensing," Proceedings of SPIE, vol. 6879, pp. 68790M-68790M-7, 2008.

[130] L. A. Siiman, J. Lumeau, and L. B. Glebov, "Phase Fresnel lens recorded in photo-thermo-refractive glass by selective exposure to infrared ultrashort laser pulses," Opt. Lett., vol. 34, pp. 40-42, 2009.

[131] M. Bellec, A. Royon, B. Bousquet, K. Bourhis, M. Treguer, T. Cardinal, M. Richardson, and L. Canioni, "Beat the diffraction limit in 3D direct laser writing in photosensitive glass," Opt. Express, vol. 17, pp. 10304-10318, 2009.

[132] M. Dussauze, E. I. Kamitsos, E. Fargin, and V. Rodriguez, "Structural Rearrangements and Second-Order Optical Response in the Space Charge Layer of Thermally Poled Sodium-Niobium Borophosphate Glasses," Journal of Physical Chemistry C, vol. 111, pp. 14560-14566, 2007.

[133] I. Rajta, I. Gomez-Morilla, M. H. Abraham, and A. Z. Kiss, "Proton beam micromachining on PMMA, Foturan and CR-39 materials," Nuclear Inst. and Methods in Physics Research, B, vol. 210, pp. 260-265, 2003.

[134] M. Will, S. Nolte, B. N. Chichkov, and A. Tünnermann, "Optical Properties of Waveguides Fabricated in Fused Silica by Femtosecond Laser Pulses," Appl. Opt., vol. 41, pp. 4360-4364, 2002.

[135] H. Zhang, S. M. Eaton, J. Li, A. H. Nejadmalayeri, and P. R. Herman, "Type II high-strength Bragg grating waveguides photowritten with ultrashort laser pulses," Electron. Lett, vol. 15, pp. 3495-3497, 2007.

[136] Q. Zhang, W. Liu, L. Liu, L. Xu, Y. Xu, and G. Chen, "Large and opposite changes of the third-order optical nonlinearities of chalcogenide glasses by femtosecond and continuous-wave laser irradiation," Appl. Phys. Lett., vol. 91, p. 181917, 2007.

[137] A. Zoubir, L. Shah, K. Richardson, and M. Richardson, "Practical uses of femtosecond laser micro-materials processing," Appl. Phys. A, vol. 77, pp. 311-315, 2003.

[138] F. Yoshino, "Multiphoton effects in the polydiacetylene poly bis(p-toluene sulfonate) of 2,4-hexadiyne-1,6-diol (PTS)," in School of Optics. vol. Doctor of Philosophy Orlando: University of Central Florida, 2003.

Résumé:

A la suite de la première démonstration de l'écriture de guide d'onde au sein de verres en 1996 par laser femtoseconde, l'écriture direct par Laser Femtoseconde (Femtoseconde Direct Laser Writing - FLDW) est apparu comme une technique souple pour la fabrication de structure photonique en trois dimensions au sein de matériaux pour l'optique.

La thèse a porté sur l'inscription par laser femtoseconde de fonctionnalités optiques au sein de verres. Des éléments diffractifs par modification de l'indice de réfraction et des structures présentant des propriétés de luminescence ou d'optique non linéaire d'ordre deux ont pu être obtenus au sein de matériaux vitreux et étudiés.

Mots Clés :

Verre
Inscription laser
Optique non linéaire
Eléments diffractifs
Laser femtoseconde

Summary

Since the first demonstration of femtosecond laser written waveguides in 1996, femtosecond laser direct writing (FLDW) has been providing a versatile means to fabricate embedded 3-D microstructures in transparent materials. The key mechanisms are nonlinear absorption processes that occur when a laser beam is tightly focused into a material and the intensity of the focused beam reaches the range creating enough free electrons to induce structural modification. This dissertation was an attempt to make an improvement on the existing FLDW technique to achieve a reliable fabrication protocol for integrated optical devices involving micro diffractive optical elements and laser-structures exhibiting second order nonlinear optical properties. Relaxation processes of directly-written structures in chalcogenide glasses have been also investigated.

.

Key Words :

Glass
Direct Laser writing
Nonlinear properties
Diffractive optical elements
Femtosecond laser